Title

Modeling Interstellar Dust Evolution in Cosmological Galaxy Simulations

Author

Choban, Caleb Ryan

Publication Date

2023

Peer reviewed|Thesis/dissertation

UNIVERSITY OF CALIFORNIA SAN DIEGO

Modeling Interstellar Dust Evolution in Cosmological Galaxy Simulations

A dissertation submitted in partial satisfaction of the
requirements for the degree Doctor of Philosophy

in

Physics

by

Caleb Ryan Choban

Committee in charge:

Professor Dušan Kereš, Chair
Professor Patrick Diamond
Professor Michael Norman
Professor Karin Sandstrom
Professor Mark Thiemens

2023

The Dissertation of Caleb Ryan Choban is approved, and it is acceptable in quality and form for publication on microfilm and electronically.

University of California San Diego

2023

DEDICATION

For my wonderful wife, Camille, and my parents, Patricia and Sandor.

EPIGRAPH

The true harvest of my daily life is somewhat as intangible and indescribable as the tints of morning or evening. It is a little star-dust caught, a segment of the rainbow which I have clutched.

- Henry David Thoreau
Walden

TABLE OF CONTENTS

Dissertation Approval Page iii

Dedication iv

Epigraph v

Table of Contents vi

List of Figures viii

List of Tables xi

Acknowledgements xii

Vita xiv

Abstract of the Dissertation xv

Chapter 1 Introduction 1
- 1.1 Interstellar Dust Grains 1
- 1.2 Dust Physics 3
- 1.3 How Dust is Observed 4
- 1.4 Dust Evolution and Life Cycle 7
- 1.5 Galaxy Formation Simulations 10

Chapter 2 The Galactic Dust-Up: Modeling Dust Evolution in FIRE 13
- 2.1 Abstract 13
- 2.2 Introduction 14
- 2.3 Methods 18
  - 2.3.1 Galaxy Feedback Mechanisms 18
  - 2.3.2 Initial Conditions 20
  - 2.3.3 Dust Evolution 21
  - 2.3.4 Dust Creation 28
  - 2.3.5 Dust Growth in the ISM 34
  - 2.3.6 Dust Destruction 37
- 2.4 Results 41
  - 2.4.1 Testing Free Parameters 41
  - 2.4.2 Element Depletions and D/Z 47
  - 2.4.3 Spatially Resolved D/Z Beyond the MW 59
- 2.5 Conclusions 62
- 2.6 Acknowledgements 65
- 2.A Effects of variations in initial conditions 65
- 2.B Sub-Resolution treatment of dense molecular gas chemistry 66

2.C Effects of variations in stellar dust formation prescriptions 70
2.D Importance of the Coulomb Enhancement and Molec-ular CO Terms 71
2.E Effects of Different Metal Yields - A Comparison between FIRE-2 and FIRE-3 . 74

Chapter 3 A Dusty Locale: Evolution of Galactic Dust Populations from Milky Way to Dwarf-Mass Galaxies 81
3.1 Abstract 81
3.2 Introduction 82
3.3 Methodology 87
3.4 Results 90
3.4.1 Cosmic Evolution 93
3.4.2 Element Depletions & Aggregate D/Z 98
3.4.3 Extragalactic Dust Emission 105
3.5 Discussion 113
3.5.1 Efficient Gas-Dust Accretion 113
3.5.2 Dust Buildup and Equilibrium 115
3.6 Conclusions 118
3.A Sight Line Methodology 120
3.B Defining Oxygen Abundance and Metallicity 121

Chapter 4 Conclusions and Future Endeavours 127

Bibliography 131

LIST OF FIGURES

Figure 1.1. Pictorial diagram of the three main methods used to observe interstellar dust and the dust properties derived from each method. 5

Figure 1.2. Pictorial diagram of the dust life cycle within galaxies. 8

Figure 2.1. Pictorial representation of mechanisms composing the dust life cycle included in our dust evolution models. 27

Figure 2.2. Comparison of the cumulative dust production (from all stellar sources) per stellar mass of carbonaceous dust (*left*) and all other dust (dominated by silicates) (*right*) over the lifetime of a stellar population 30

Figure 2.3. "Elemental" time evolution of galaxy-integrated D/Z ratio (*top*), fraction of total dust mass from each source (*middle*), and fraction of total dust mass composed of each dust species (*bottom*) for an idealized Milky Way-like galaxy. 44

Figure 2.4. "Species" time evolution of galaxy-integrated D/Z ratio (*top*), fraction of total dust mass from each source (*middle*), and fraction of total dust mass composed of each dust species (*bottom*) for an idealized Milky Way-like galaxy. 45

Figure 2.5. Predicted sight line C, O, Mg, Si, and Fe depletion versus $N_{\mathrm{H,neutral}}$ from 10,000 sight lines at the solar galactic radius in an idealized Milky Way-like galaxy 50

Figure 2.6. Predicted C, O, Mg, Si, and Fe depletion versus $n_{\mathrm{H,neutral}}$ in an idealized Milky Way-like galaxy 51

Figure 2.7. Relation between D/Z ratio and $n_{\mathrm{H,neutral}}$ in an idealized Milky Way-like galaxy for "Species" and "Elemental" implementations, with 16-/84-percentiles represented by shaded regions. 54

Figure 2.8. Relation between median D/Z ratio and neutral gas surface density (*left*) and galactocentric radius (*right*) in 2 kpc bins at simulation end for the "Elemental" and "Species" implementations with 16-/84-percentiles represented by the shaded regions. 61

Figure 2.9. Same as Fig. 2.6 comparing our "Species" implementation (including Nano-iron and O-reservoir dust species) 67

Figure 2.10. Same as Fig. 2.7 comparing our "Species" implementation (including Nano-iron and O-reservoir dust species) 68

Figure 2.11. Resulting median molecular mass fraction (f_{H_2}) (*solid*) predicted in our simulated galaxy's ISM gas and median mass fraction of gas in dense molecular phase (f_{dense}) (*dashed*) produced by our model 71

Figure 2.12. Same as Fig. 2.3 but varying our assumed creation/formation efficiencies for the "Elemental" implementation of dust. 72

Figure 2.13. Same as Fig. 2.4 but varying our assumed dust creation/formation efficiencies for the "Species" implementation of dust. 73

Figure 2.14. Same as Fig. 2.6 comparing our default "Species" implementation (including Nano-iron and O-reservoir dust species) with (*solid*) and without (*dashed*) the default terms which attempt to account for Coulomb enhancement 75

Figure 2.15. Same as Fig. 2.7 comparing our default "Species" implementation (including Nano-iron and O-reservoir dust species) with (*solid*) and without (*dashed*) the default terms which attempt to account for Coulomb enhancement 76

Figure 2.16. Cumulative SNe metal yields per stellar mass for main refractory elements in dust over a stellar population's life for the assumed yield models in FIRE-2 and FIRE-3 78

Figure 2.17. Same as Fig. 2.6 comparing the "Species" implementation with O-reservoir and Nano-iron dust species integrated with FIRE-2 or FIRE-3 stellar feedback and ISM physics. 79

Figure 2.18. Same as Fig. 2.7 comparing the "Species" implementation including Nano-iron and O-reservoir dust species integrated with FIRE-2 and FIRE-3 stellar feedback and ISM physics. 80

Figure 3.1. Face-on and edge-on images of our spiral and dwarf spiral galaxies at $z = 0$. 91

Figure 3.2. Mock images, same as Fig. 3.1, of our irregular dwarf galaxies. 92

Figure 3.3. Evolution of total galactic gas, stellar, and dust properties for our simulated galaxies for all gas/stars within 10 kpc of the galactic center. 94

Figure 3.4. Time evolution of metallicity (*top*), D/Z (*second from top*), dust creation source mass fraction (*second from bottom*), and dust species mass fraction (*bottom*) for **m12i** (*left*), **m11v_halo0** (*middle*), and **m11d** (*right*). 96

Figure 3.5. Same as Fig. 3.4 for **m11e** (*left*), **m11v_halo2** (*middle left*), and **m11i** (*middle right*) and **m10q** (*right*). 97

Figure 3.6. Predicted median sight line C, O, Mg, Si, and Fe depletion versus $N_{\mathrm{H,neutral}}$ from in-disk sight lines for **m12i** and face-on sight lines for **m11v_halo0**, **m11d**, **m11e**, **m11v_halo2**, and **m11i** following the sight line methodology outlined in Appendix 3.A. . . . 103

Figure 3.7. Resulting C, O, Mg, Si, and Fe depletion versus $n_{\mathrm{H,neutral}}$ for gas within the 10 kpc of each galaxy at z=0. . . . 104

Figure 3.8. Resulting D/Z versus $n_{\mathrm{H,neutral}}$ (*left*) and temperature (*right*) for gas within 10 kpc for each galaxies at z=0. . . . 105

Figure 3.9. Resulting relation between galaxy integrated D/Z and metallicity for our galaxies over time. . . . 107

Figure 3.10. Relation between median D/Z ratio and galactocentric radius (*top left*), neutral gas surface density (*top middle*), molecular gas surface density (*top right*), stellar surface density (*bottom left*), star formation rate surface density (*bottom middle*), gas-phase oxygen abundance (*bottom right*) 109

Figure 3.11. Resulting D/$\mathrm{H_{neutral}}$ versus $\Sigma_{\mathrm{gas,neutral}}$ with (*left*) 144 pc resolution pixels and (*right*) 14 pc resolution pixels from face-on projections of each galaxy at $z = 0$. . . . 111

Figure 3.12. Predicted evolution of the degree of condensation for Si bound in silicate dust through successive cycles of gas into dense clouds, where the dust grows via accretion, and out into diffuse clouds, where it is destroyed by SNe, using Eq. 20 and Eq. 21 in C22. . . . 117

Figure 3.13. Face-on (*top*) and edge-on (*bottom*) gas density projection of **m12i** with a subset of our sight lines (*white lines*) to young stars overplotted. . . . 122

Figure 3.14. Face-on gas density projection of **m11v_halo0** (*top left*), **m11d** (*top right*), **m11e** (*bottom left*), and **m11v_halo2** (*bottom right*) with all young stars (*gold stars*) overplotted. . . . 123

Figure 3.15. Resulting oxygen abundances from different definitions for our suite of simulations. . . . 125

Figure 3.16. Resulting relation between median O abundance and median metallicity for all gas within $0.1R_{\mathrm{vir}}$ for our suite of simulations. . . . 126

LIST OF TABLES

Table 2.1. Condensation efficiencies for “Elemental” and “Species” implementations taken from Dwek (1998) and Zhukovska et al. (2008). 33

Table 2.2. Summary of input constants assumed in our “Species” gas-dust accretion model. 38

Table 2.3. Table summarizing whether or not a given piece of our assumed dust physics strongly influences either the D/Z ratio or element-by-element depletion trends. 59

Table 3.1. Parameters describing initial conditions of simulations in this paper. 88

ACKNOWLEDGEMENTS

It would be remiss of me not to express my deepest gratitude to my PhD advisor, Professor Dušan Kereš, whose guidance and support helped me become the scientist I am today. Our numerous discussions about research and life, always punctuated by Dušan's signature deadpan humor, helped me forge my path in academia while reminding me to take time for life outside of work. I look forward to many future discussions, hopefully over a "good" glass of wine that does not taste of sour cabbage. I would also like to express my gratitude to Professor Karin M. Sandstrom. Although unofficial, I think of her as a second advisor. Her infectious enthusiasm for interstellar dust, and science in general, helped me find joy in research even in the most stressful of times and inspired me to help mentor and encourage the next generation of scientists.

My research would not have been as robust nor detailed without the aid and support of my collaborators, Philip Hopkins, Claude-André Faucher-Giguère, and Christopher Hayward. I also appreciate the guidance and feedback provided by the members of my dissertation committee - Patrick Diamond, Mark Thiemens, and Michael Norman. Their insights and questions improved my dissertation and made for an enjoyable dissertation defense.

I give my heartfelt appreciation to my wife, Camille. Her love, support, and patience helped me develop into a person I never thought I could become. I am lucky to have such a wonderful person to share the unexpected twists and turns of life with, and I look forward to the many misadventures the future holds for us.

I would like to thank my senior research members Tsang Keung Chan, Nathan Butcher, and Bili Dong. They provided much need guidance in my earlier years, helping develop my code wrangling and supercomputer whispering skills that I have strived to pass on to our newest junior members. I would also like to thank my office mate I-Da Chiang, our numerous impromptu discussions on the minutia of dust observations truly enlightened a theorist such as I am.

I sincerely thank my close friends and 'adoptive' family, Sanchit Sabhlok, Cameron Trapp, Stella Zhang, Anna Miller, Murphy Hernandez, Mayia Vranas, and Max Silva-Feaver. They put up with, and somewhat encouraged, my ramblings on various topics, helped preserve my sanity during the COVID pandemic, and, most important of all, showed me that true friends support each other in all facets of life. They also helped me step away from work and enjoy the intangible things, such as hiking, biking, and drinking with good company, that make life fulfilling and lead to lifelong friendships.

My heart also goes out to all the cafes in Hillcrest, which provided me with a late-night refugee for writing and studying. I also want to thank the San Diego Zoo and all the animals within it, who provided much needed respite from thesis writing. Especially Kaja, the baby orangutan.

Chapter 2, in full, is a reprint of the material as it appears in *Monthly Notices of the Royal Astronomical Society*, Choban, Caleb R.; Kereš, Dušan; Hopkins, Philip F.; Sandstrom, Karin M.; Hayward, Christopher C.; Faucher-Giguère, Claude-André, Volume 514, Issue 3, August 2022, Pages 4506–4534. The dissertation author was the primary investigator and author of this paper.

Chapter 3, in full, is currently being prepared for submission for publication of the material. Choban, Caleb R.; Kereš, Dušan. The dissertation author was the primary investigator and author of this material.

VITA

2015	B. S. in Physics *cum laude*, University of California San Diego
2016-2023	Graduate Student Researcher, University of California San Diego
2023	Ph. D. in Physics, University of California San Diego

ABSTRACT OF THE DISSERTATION

Modeling Interstellar Dust Evolution in Cosmological Galaxy Simulations

by

Caleb Ryan Choban

Doctor of Philosophy in Physics

University of California San Diego, 2023

Professor Dušan Kereš, Chair

Interstellar dust grains play prominent roles in physical processes across astronomical scales and affect all astronomical observations to varying degrees. However, our understanding of how dust evolves within galaxies and across cosmic time is incomplete. We investigate the dust life cycle and make predictions for the evolution of galactic dust populations across cosmic time by developing dust evolution models and integrating them into cosmological galaxy simulations.

In Chapter 2, we present two separate dust evolution models coupled with the “Feedback In Realistic Environment” (FIRE) model for stellar feedback and ISM physics. These models incorporate the main mechanisms comprising the dust life cycle but differ in their treatment of dust chemical composition and gas-dust accretion based on recent, contrasting approaches

in the galaxy formation community. We test and compare these models in an idealized Milky Way-mass galaxy and find that both produce reasonable galaxy-integrated dust populations and predict gas-dust accretion as the main dust growth mechanism. However, only a model that simultaneously incorporates a physically motivated gas-dust accretion routine and tracks the evolution of specific dust species can reproduce observed spatial dust variability within the Milky Way, in both amount and composition.

In Chapter 3, we present a suite of cosmological galaxy simulations of Milky Way to dwarf halo-mass galaxies. These simulations utilize the dust evolution model presented in Chapter 2, which tracks the evolution of specific dust species and incorporates a physically motivated dust growth routine. We find that gas-dust accretion is the dominant producer of dust mass for all but the most metal-poor galaxies and, in the case of the Milky Way, dominates for the majority of the galaxy's life. We also discover that the onset of rapid growth via gas-dust accretion differs between dust species, arising from differences in element abundances, dust physical properties, and life cycles. These differences can explain the variable dust population, in both amount and composition, in the MW, LMC, and SMC and highlight the importance of accurate gas-dust accretion modeling for individual dust species.

Chapter 1

Introduction

1.1 Interstellar Dust Grains

When you look up to the sky on a particularly dark night, with either your eyes or an optical telescope, you will observe a bright streak, or band, of stars stretching across the sky which we call the Milky Way. The keen observer will notice that this band is patchy but uniformly luminous in appearance, with no region being exceptionally brighter than any other region on average. Indeed, classical astronomers (i.e. wealthy gentry/nobility who took an interest in all manner of arts and sciences) who were limited to visible light observations noticed this and postulated that Earth must be at the center of the Milky Way (e.g. Herschel, 1785). It was not until the early 1900s that modern astronomers discovered an absorbing medium exists between the stars (Barnard, 1907, 1910). This dims the light of stars in proportion to the amount and density of medium along our line of sight and obscures the true center of the Milky Way, which is 8.5 kiloparsecs from Earth[1]. It was later determined that this absorbing medium is comprised of numerous small particles residing within the interstellar medium (ISM), collectively called interstellar dust grains (Trumpler, 1930).

In the succeeding decades, observations across all wavelengths, from X-ray to radio, have yielded a plethora of information about dust and contributed to the current paradigm. Interstellar

[1] The position of the Galactic Center was initially inferred from globular cluster positions (Shapley, 1918) and later via radio emissions from a supermassive black hole likely located there (Jansky, 1933; Oort & Rougoor, 1960).

dust grains are amorphous solid particles comprised of astrophysical metals[2] (mainly C, O, Mg, Si, and Fe). They range from ~1 nm to ~1 μm in size and are primarily composed of two chemically distinct species, silicates and carbonaceous, with carbonaceous dust being further subdivided into amorphous graphite and polycyclic aromatic hydrocarbons (PAHs)[3]. Within the Milky Way, dust grains make up only 1% of the ISM by mass but account for ~40% of all metals (dust-to-metals ratio; D/Z). They are abundant within most galaxies and are observed even in young galaxies in the early universe (e.g. Strandet et al., 2017). Dust preferentially absorbs ultraviolet (UV) and optical light and re-emits light in the infrared (IR), affecting all astronomical observations to varying degrees. Therefore a detailed understanding of dust's effects on observations of astronomical objects, from individual stars to galaxies, is needed to determine these objects' true nature. Dust is also an integral component of numerous physical processes across astronomical scales. It is critical for the formation of stars, stellar feedback via radiation pressure, and heating and cooling channels responsible for ISM phase structure. Therefore an accurate accounting of dust physics is needed to model and predict the impact of these processes.

Despite the extensive insights revealed by observations, many uncertainties remain. What is the dust life cycle and how does it evolve within galaxies? How does dust and its evolution affect galactic evolution? How can we disentangle the observational effects of dust to interpret observations? With the recent launch of the James Webb Space Telescope (JWST), future observations will provide a wealth of information by probing dust populations in various environments, from the heart of local supernovae (SNe) to distant, young galaxies with unprecedented resolution. However, observations of dust alone cannot answer these questions since they provide only brief snapshots of a complex system involving numerous physical processes which has evolved over billions of years. Computational simulations in concert with observations are needed to disentangle this system and provide a self-consistent 'laboratory' to interpret observations. In this

[2]In astrophysics, metals are any element heavier than hydrogen and helium.

[3]PAHs are a unique species of extremely small grains (<1nm), comprising <5% of the dust mass within galaxies (Li, 2020). Very little is known about their evolution, but JWST provides an excellent tool for future study.

dissertation, I attempt to broaden our understanding of interstellar dust evolution and life cycle by developing novel dust evolution models incorporated into state-of-the-art galaxy formation simulations.

For the remainder of this chapter, I review dust physical processes and their importance in a galactic context. I then describe the different ways interstellar dust is observed and what they tell us about dust populations. I summarize what observations reveal to us about dust evolution within galaxies and across cosmic time, culminating in our current understanding of the dust life cycle. Finally, I give a brief overview of galaxy formation simulations which are ideal tools for testing dust evolution theory along with the current state of the field.

1.2 Dust Physics

Interstellar dust grains play a prominent role in physical processes on almost all astronomical scales, affecting everything from star/planet formation to galaxy evolution. The surface of dust grains provides a catalyst site for important astrochemistry. Most importantly, the formation of H_2 molecules on dust grain surfaces is by far the most efficient formation channel, occurring >3 orders of magnitude faster than gas-phase formation channels (Gould & Salpeter, 1963; Hollenbach & Salpeter, 1971). Therefore, dust grains are critical for the formation of molecular clouds and, indirectly, the stars that form within them. Dust grains are also a critical mediator for feedback around star-forming regions. These regions house young stars that produce massive amounts of radiation, which dust grains absorb and scatter. This produces radiation pressure that pushes the dust grains, which is then translated to the gas the dust resides in through collisional (drag) and electrodynamic forces. This pressure is a crucial component of feedback from young stars on local and galactic scales. Stellar feedback halts the infall of nearby gas, regulating local star formation, and drives galactic winds, shaping galaxy evolution (Thompson et al., 2005; Murray et al., 2010). Dust is also a critical heating and cooling source in various phases of the ISM. When dust grains absorb energetic photons, an electron can be ejected from the grains.

These photoelectrons can then heat the surrounding gas via collisions. This photoelectric heating is the primary heat source in the neutral ISM (Tielens & Hollenbach, 1985). In hot plasmas, ion-dust collisions excite dust grains which then radiate that energy in the IR, cooling the plasma (Dwek & Werner, 1981; Dwek, 1987). All of these physical processes strongly depend on the amount and size of dust grains, which can evolve over time. Therefore, to accurately model these processes requires an understanding of the evolution of dust populations.

1.3 How Dust is Observed

Before we study how dust evolves within galaxies, we must first understand the distinct ways in which astronomers observe dust, what they have contributed to the current interstellar dust paradigm, and the uncertainties that remain. There are three main methods for observing dust: (1) dust extinction of UV, optical, and IR light, (2) IR dust emission, and (3) gas-phase element depletions. An illustration of each observational method can be seen in Fig. 1.1, along with a brief description of each provided below.

The oldest method used to quantify interstellar dust is via its dimming of UV/optical light from stars, appropriately named extinction. In particular, dust selectively absorbs and scatters light depending on its wavelength. This wavelength-dependent extinction[4] curve (A_λ) depends on the size of dust grains and their chemical composition. Of particular note is the prominent 2175 Å feature/bump, which is produced by small carbonaceous grains originally postulated to be amorphous graphite in structure (Stecher & Donn, 1965), although PAHs are now the favored candidate (Shivaei et al., 2022). There are also smaller Si-O and O-Si-O features at 9.7μm and 18μm corresponding to silicate grains of olivine ($[\mathrm{Mg_xFe_{(1-x)}}]_2\mathrm{SiO_4}$) and pyroxene ($\mathrm{Mg_xFe_{(1-x)}SiO_3}$) composition (e.g. Henning, 2010). Given these features and the general shape of the extinction curve, the size distribution of each dust grain species can also be determined (see Fig. 1.1 for a simple schematic of dust extinction curves and these

[4]'Reddening' is also a commonly used terminology due to the preferential absorption and scattering of 'blue' light, making stars redder in appearance.

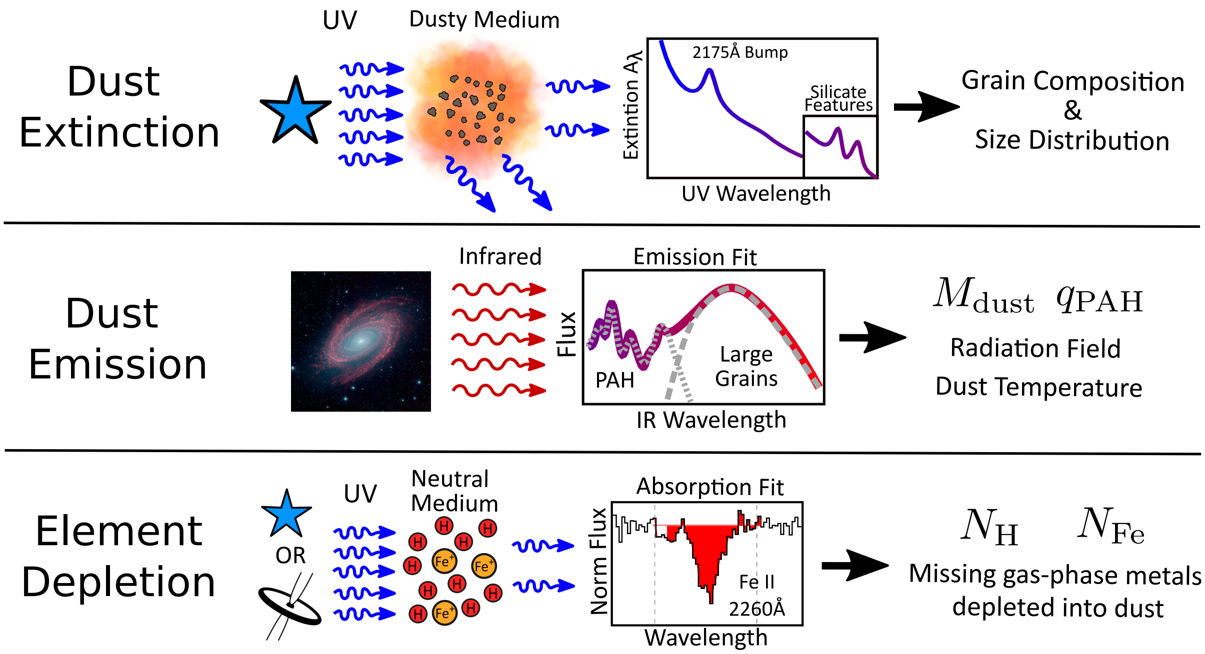

Figure 1.1. Pictorial diagram of the three main methods used to observe interstellar dust and the dust properties derived from each method.

features). The observed features and shape of extinction curves indicate that the dust population within the Milky Way consists primarily of silicates and carbonaceous material with a roughly power-law size distribution $dn/da \propto a^{-3.5}$ (Mathis et al., 1977) dominated by small grains in number. Since this dust extinction technique requires observations of individual stars, its use is limited to within the Milky Way and its satellites, the Large and Small Magellanic Clouds (LMC & SMC). An extension of this technique aggregates multiple sight lines to quantify the effects of light extinguished, light scattered back into the line of sight, and light from unobscured stars. This is called dust attenuation and can be used to investigate dust populations outside the Milky Way and its satellites, but star-dust geometry and radiative transfer effects make determination of the underlying dust population properties nontrivial (e.g. Salim & Narayanan, 2020).

Another method to study dust properties is through their IR emission. Small grains are stochastically heated by photons causing them to emit photons at specific wavelengths in the near-to-mid-IR. Large grains constantly receive and emit photons due to their size, reaching thermal equilibrium and producing a modified black body thermal emission spectrum in the far-IR (e.g. Bianchi, 2013). Theoretical dust emission models fitted to observed IR emission spectra yield information on the total dust mass, the fraction of the dust mass composed of PAHs ($q_{\rm PAH}$), as well as other information (e.g. dust temperature, local radiation field) depending on the complexity of the dust model used (Chastenet et al., 2021). However, given the complexities in the interpretation of dust emission spectra[5], the complete dust chemical makeup is difficult to obtain. Due to its less stringent resolution requirements, this technique is widely used to study dust outside the MW. In particular, it can probe the dust populations of entire galaxies and spatially-resolved areas within them (Draine et al., 2007; Rémy-Ruyer et al., 2014; Chiang et al., 2018; Galliano et al., 2018).

The primary indirect method of examining dust is via observations of elements missing from the gas-phase, called gas-phase element depletions. By observing the spectra from bright UV sources (O/B-type stars or quasars), the gas-phase abundance of individual elements along the line of sight to the source can be determined from the distinct UV absorption features they produce. These abundances are then compared to the expected abundance of each element in the gas along the line of sight, determined from observations of stellar photospheres, with any missing elements assumed to be locked in dust (e.g. Jenkins, 2009). This technique gives a detailed accounting of the elements locked in dust, providing solid constraints for the chemical composition and amount of dust. However, due to its reliance on high spectral resolution, observations are primarily limited to within the MW, LMC, and SMC and individual quasar sight lines through damped Lyα systems. A significant discovery of this technique is that the current silicate-carbonaceous dust composition paradigm cannot explain the observed depletions of oxygen and iron, suggesting currently unobserved dust species (Jenkins, 2009; Whittet, 2010).

[5] Dust masses derived from IR emissions can vary by up to a factor of 3 depending on the dust model used (Chastenet et al., 2021), and over predict dust masses compared to those derived using other observational techniques (Chiang et al., 2021).

1.4 Dust Evolution and Life Cycle

Our understanding of dust populations was originally derived from observations of dust within the Milky Way utilizing the methods previously described. The Milky Way has a relatively uniform dust population with a fraction of metals in dust of D/Z~40%, a silicate-to-carbonaceous dust mass ratio of 3:1, and a fraction of dust mass comprised of PAHs of q_{PAH}~4.6% (Li & Draine, 2001; Weingartner & Draine, 2001a). However, observations outside the Milky Way reveal that this does not hold for all galaxies nor all time.

Local galaxies (e.g. LMC, SMC, Andromeda, Triangulum) provide the most robust evidence of this. Due to their 'close' proximity to the Milky Way, extinction, emission, and element depletion observations can be used in concert, providing the clearest picture of dust population variability within and between galaxies. Dust emission and element depletions show that these galaxies all exhibit increasing D/Z in denser environments (Jenkins, 2009; Roman-Duval et al., 2021; Clark et al., 2023). Element depletions also indicate a decrease in galaxy averaged D/Z between the Milky Way, LMC, and SMC, respectively, and a changing chemical composition (Roman-Duval et al., 2022a). Dust extinction curves reveal a sharp decrease in the abundance of small carbonaceous grains between the Milky Way and LMC, and a complete lack of them in the SMC (Pei, 1992; Weingartner & Draine, 2001a). This is further reinforced by observed PAH emissions which show decreasing q_{PAH} of ~3.3% and ~1.0% for the LMC and SMC respectively (Chastenet et al., 2019).

Beyond the local neighborhood, dust populations within galaxies cannot be spatially resolved. However, galaxy-integrated dust populations can be observed via dust emission and, in conjunction with a large observational sample, can reveal relations between dust populations and various galactic properties, providing insights into dust evolution over time. These observations reveal a clear correlation between galactic D/Z and metallicity, with D/Z sharply increasing with metallicity before plateauing at high-metallicity (Rémy-Ruyer et al., 2014; De Vis et al., 2019). Observations of PAHs also show a strong relation with galactic metallicity, with q_{PAH} rapidly

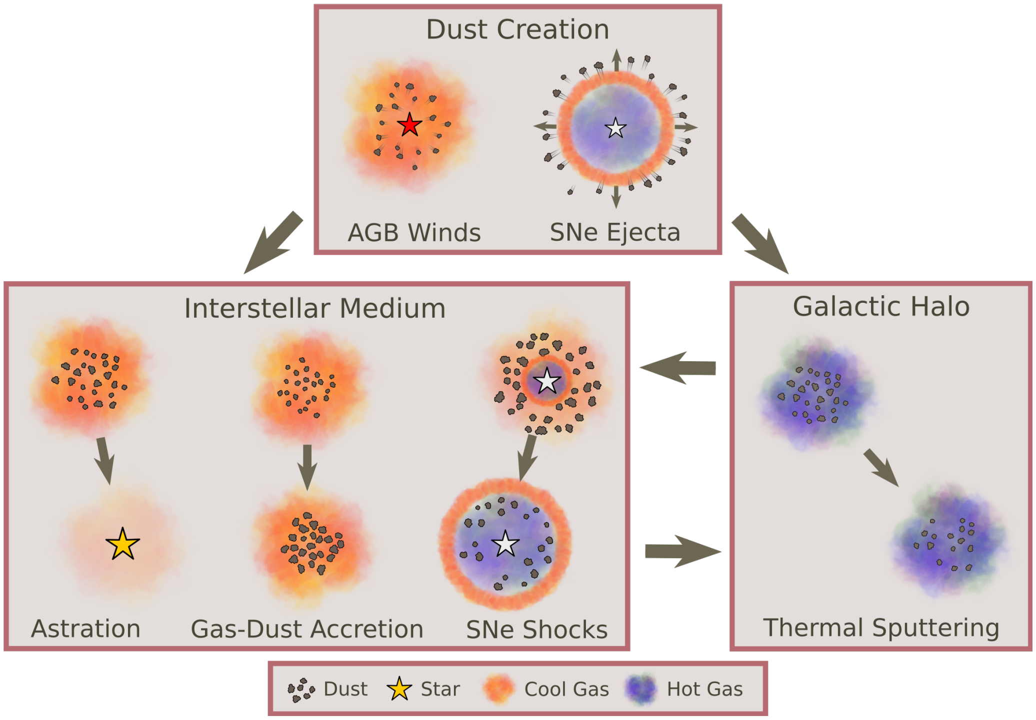

Figure 1.2. Pictorial diagram of the dust life cycle within galaxies.

increasing above a critical metallicity (Draine et al., 2007; Rémy-Ruyer et al., 2015; Aniano et al., 2020; Galliano et al., 2021).

All these observations suggest a complex dust life cycle that depends on the local gas properties the dust resides in and possibly on the history of the galaxy as a whole. Combined with theoretical models, these observations have guided our understanding of the dust life cycle. This life cycle involves numerous processes which can create, grow, and destroy dust grains. An illustration of the dust life cycle can be seen in Fig 1.2, with a description of each process provided below.

Creation: The typical temperatures, pressures, and heavy element abundances required for gas-phase metals to condense directly into solid dust grains are only achieved in the dense, metal-rich environments of stellar ejecta. Primarily that of core-collapse supernovae (SNe II), the explosive ends of massive ($>8M_{\odot}$) stars, and the stellar winds of asymptotic giant branch (AGB) stars, the end stage of intermediate to low mass ($0.5-8M_{\odot}$) stars during which they successively shed their stellar envelope. Observations of local supernovae and AGB stars suggest that a fraction of the metals they produce condensed into dust. However, the efficiency of this process is poorly constrained.

Destruction: Violent events and hostile environments can shatter, erode, and outright destroy dust grains through various processes. Supernova remnants (SNR), produced by strong shock waves from supernovae, are believed to be the primary destroyers of dust. These remnants shock heat gas as they travel through the ISM, efficiently destroying dust within the gas due to gas-dust and dust-dust collisions. Dust grains residing in hot, ionized gas experience collisions from highly energetic protons and helium ions, which can shatter and erode large dust grains and completely destroy small dust grains through the process of thermal sputtering (Draine & Salpeter, 1979). As dense molecular clouds cool and collapse, forming stars, dust within the cloud is destroyed through the process of astration, contributing to the stars' composition.

Growth: Dust grains residing in cool, dense gas can grow via the accretion of gas-phase metals. Gas-phase metals collide with dust grains and, due to their low energy in these environments, stick to their surface, growing them over time. Gas-dust accretion is collisional in nature, depending on the density and metallicity of local gas, but the exact physical processes that determine the effective accretion rate are unclear. However, efficient gas-dust accretion is necessary to explain the amount of dust we see within the Milky Way, and could be the primary dust production mechanism in most galaxies (e.g McKee, 1989; Draine, 2009).

Large uncertainties exist for all of these processes, and the exact importance of each in the overall evolution of dust within galaxies is debated. Galaxy formation simulations coupled with dust evolution models can elucidate this issue and further refine our understanding of the dust life cycle.

1.5 Galaxy Formation Simulations

Accurate modeling of the formation and evolution of galaxies in which dust resides is necessary to study dust evolution. In the last few decades, a revolution in our understanding of galaxy evolution has occurred owing to the adoption of computational simulations for theoretical modeling and the continued surge in computing power. During this time, two approaches have arisen, semi-analytical models and cosmological galaxy simulations. Semi-analytical models utilize set prescriptions and approximations to model complicated and interwoven astronomical processes such as star formation and galaxy merger history. These prescriptions include numerous free parameters that are 'tuned' to match observational constraints or are derived from more detailed simulations. Due to their assumptions and approximations, semi-analytical models have low computational cost and can typically run on personal computing hardware. On the other hand, cosmological galaxy simulations directly model many physical processes utilizing numerical methods, including direct modeling of gravitational, gas-phase, and other interactions using millions or billions of computational elements. They follow the evolution of galaxies across cosmic time and attempt to infer galactic properties from first principles. These simulations can also produce self-consistent galactic histories, modeling the gravitational dynamics of galactic mergers and the complex physical processes within their ISM, such as gas cooling, star formation, and stellar feedback. Due to this complexity, these simulations require drastically more computing power than semi-analytical models, necessitating the use of supercomputers.

Low computational cost provides a major advantage for semi-analytical models and allows for the generation of large sample sizes, which can be statistically compared with observations. They can also be used to understand the broader implications of various model ingredients (e.g. the necessity of stellar feedback to stop the runaway collapse of galactic halos). For these reasons, semi-analytical models helped paint the broad strokes of our current understanding of the dust life cycle (e.g. Dwek, 1998), reviewed in Chapter 1.4. However, due to their oversimplifications and 'tuned' parameters, these models are ill-suited for investigating the intricate details and physics of dust processes and their effects on dust evolution over the age of the universe. In contrast, cosmological galaxy simulations focus on the direct interactions and properties of small-scale computational elements, making them excellent tools for the task.

These simulations model the evolution of galaxies in a fully cosmological context, with galactic structures growing hierarchically as predicted by the Lambda-CDM model (e.g. Katz et al., 1996). The initial small density perturbations in the early universe collapse due to gravitational instability, forming the first dark matter (DM) halos. Gas subsequently collapses into the center of these halos, forming the first galaxies devoid of metals and dust. Over time, these DM halos merge and grow, building larger structures. Galaxies within these halos grow via accretion of intergalactic gas and mergers with other galaxies (e.g. Kereš et al., 2005). This results in a complex system where stars form within galaxies and pollute them with metals while incoming low metallicity gas dilutes their metal content. This ability to follow the evolution of galaxies from their inception to the present day makes cosmological galaxy simulations ideal for investigating the evolution of dust from its initial creation in the first SNe and AGB stars and across cosmic time.

The "Feedback in Realistic Environments" (FIRE; Hopkins et al. 2014, 2018a, 2023) cosmological galaxy simulations are particularly noteworthy in this respect. The FIRE simulations incorporate a comprehensive suite of modeled gas physics, including detailed implementation of stellar feedback, star formation, and heating and cooling channels. These capabilities have enabled FIRE to reproduce a wide range of observed galaxy relations and their evolution across time. In particular, the Kennicutt–Schmidt star formation law (Orr et al., 2018) and the mass-metallicity relation and its evolution over redshift (Ma et al., 2016), where galaxy evolution is governed by the cycles and strengths of infalling and outflowing gas in galaxies (Muratov et al., 2015). Given these successes, I employ FIRE simulations to test our understanding of the dust life cycle and investigate dust evolution within galaxies.

Cosmological galaxy simulations typically model the numerous physical processes dust is responsible for, as described in Chapter 1.2, but assume a fixed fraction of metals locked in dust. Only in the last few years has the galaxy formation community put serious effort into developing dust evolution models. However, contrasting approaches have arisen, diverging in two primary aspects. **(1) Resolving Power**: Some models directly resolve when and where the processes comprising the dust life cycle occur within galaxies (Zhukovska et al., 2016; Granato et al., 2021), while others rely on 'tunable' sub-resolution routines to approximate these processes (Bekki, 2015a; McKinnon et al., 2016). **(2) Dust Composition**: Tracking the evolution of separate, chemically-distinct dust species is difficult and requires confronting uncertainties in dust chemical composition (Zhukovska et al., 2008, 2018; Granato et al., 2021), therefore many models assume a single, chemically ambiguous dust population (McKinnon et al., 2016; Li et al., 2019; Aoyama et al., 2020).

In this dissertation, I introduce one of the first dust evolution models to resolve dust life cycle processes and include details of dust composition integrated into cosmological galaxy simulations. In Chapter 2, I introduce two separate dust evolution models I developed to test these contrasting approaches and investigate their effects on the expected evolution of interstellar dust. I show that only a model that simultaneously resolves dust life cycle processes and tracks the evolution of specific dust species can reproduce observed spatial dust variability within the Milky Way, in both amount and composition. In Chapter 3. I analyze the evolution of galactic dust populations over cosmic time utilizing cosmological galaxy simulations. I demonstrate that gas-dust accretion is the dominant producer of dust mass for all but the most metal-poor galaxies. I also show that the differences in accretion efficiencies and life cycles between dust species could explain the variable dust populations in galaxies.

My dissertation research is documented in one publication (Choban et al., 2022) and one publication in preparation (Choban et al. in preparation) as listed in the reference sections.

Chapter 2

The Galactic Dust-Up: Modeling Dust Evolution in FIRE

2.1 Abstract

Recent strides have been made developing dust evolution models for galaxy formation simulations but these approaches vary in their assumptions and degree of complexity. Here we introduce and compare two separate dust evolution models (labelled ‘Elemental’ and ‘Species’), based on recent approaches, incorporated into the GIZMO code and coupled with FIRE-2 stellar feedback and ISM physics. Both models account for turbulent dust diffusion, stellar production of dust, dust growth via gas-dust accretion, and dust destruction from time-resolved supernovae, thermal sputtering in hot gas, and astration. The “Elemental” model tracks the evolution of generalized dust species and utilizes a simple, ‘tunable’ dust growth routine, while the “Species” model tracks the evolution of specific dust species with set chemical compositions and incorporates a physically motivated, two-phase dust growth routine. We test and compare these models in an idealized Milky Way-mass galaxy and find that while both produce reasonable galaxy-integrated dust-to-metals (D/Z) ratios and predict gas-dust accretion as the main dust growth mechanism, a chemically motivated model is needed to reproduce the observed scaling relation between individual element depletions and D/Z with column density and local gas density. We also find the inclusion of theoretical metallic iron and O-bearing dust species are needed in the case of specific dust species in order to match observations of O and Fe depletions,

and the integration of a sub-resolution dense molecular gas/CO scheme is needed to both match observed C depletions and ensure carbonaceous dust is not overproduced in dense environments.

2.2 Introduction

Although it only makes up 1% of the interstellar medium (ISM) by mass in the Milky Way (Whittet, 2003), dust is integral to the physics within. It provides a surface for complex astrochemistry such as H_2 formation (Hollenbach & Salpeter, 1971), facilitating the formation of molecular clouds and indirectly stars. It is a key coolant in extremely dense environments (Goldsmith & Langer, 1978; Burke & Hollenbach, 1983; Goldsmith, 2001), important for star and planet formation, is the primary heat source via the photoelectric effect in neutral phases of the ISM (Tielens & Hollenbach, 1985; Hollenbach et al., 1991; Weingartner & Draine, 2001b), and can reduce the abundance of important gas coolants, which allow gas to cool and collapse, by locking away elements from the gas phase. Dust also affects how the ISM reacts to radiation pressure and might help drive galactic winds (Murray et al., 2005; Thompson et al., 2015), which can be crucial for shaping galaxy evolution. Observationally, dust redistributes the stellar spectral energy distribution (SED) shifting optical-UV light to infrared affecting all observations to varying degree (e.g Salim & Narayanan, 2020). This fact along with the spatial distribution of dust within galaxies is especially critical for constraining the star formation rate density (SFRD) (Madau & Dickinson, 2014). For example, the exact dust geometry (clumpiness and covering fraction) and relative distribution between dust and stars has dramatic effects on the effective attenuation law and thus the IRX-β_{UV} relation (Narayanan et al., 2018; Liang et al., 2021), which is a useful tool to constrain the attenuation properties at UV wavelengths of high-z galaxies.

In order for these physical processes and observations to be accurately modelled and predicted in simulations a detailed understanding of dust evolution on galactic/cosmological scales is needed. Currently many galaxy formation models treat dust in post-processing or assume a constant dust-to-metals ratio (D/Z) (e.g. Hayward et al., 2011; Narayanan et al., 2015;

Camps et al., 2016; Trayford et al., 2017, 2020; Liang et al., 2018, 2019; Ma et al., 2019), and therefore may not accurately predict observed diverse dust scaling relations and their evolution. For example, in the Milky Way, observations of gas-phase element depletions (fraction of elements missing from the gas-phase assumed to be locked in dust) indicate a strong correlation between the total amount of metals in dust and gas density along with a varying dust population composition (Jenkins, 2009). Similar relations have also been found for the Magellanic Clouds but with systematically smaller fractions of metals in dust (Jenkins & Wallerstein, 2017; Roman-Duval et al., 2019b). Outside the MW and its satellites, galaxy surveys of 126 local galaxies by Rémy-Ruyer et al. (2014) and ~500 local galaxies by De Vis et al. (2019) found an overall increase of D/Z with metallicity with a large (>1 dex) scatter in the galaxy-integrated D/Z at a given metallicity. Interestingly, these studies disagree on whether this relation extends to high metallicity ($12+\log_{10}(\mathrm{O/H}) > 8.1$) or becomes approximately constant. Recent spatially-resolved studies of individual, local galaxies also show D/Z variation with local gas properties (Roman-Duval et al., 2017; Chiang et al., 2018, 2021; Vílchez et al., 2019). Furthermore, the current paradigm of carbonaceous-silicate dust chemical composition based on observed dust extinction curves (e.g. Draine & Li, 2007) does not fully agree with the above observations. In particular, observations of O and Fe gas-phase depletions (Whittet, 2010; Dwek, 2016) cannot be explained by silicate dust alone, suggesting currently unknown dust species. This can be especially important for the expected D/Z since O makes up a large fraction of the metal mass. These all suggest a complex dust system which depends heavily on the local gas properties the dust resides in and possibly on the history of the galaxy as a whole. This necessitates a more detailed modelling of dust in galaxy simulations to accurately account for stellar feedback and the effects of dust on galaxy evolution. Furthermore, detailed dust modelling will help interpret and guide observations such as the predicted amount and composition of dust populations in various gas and galactic environments which determine the expected dust extinction curves and emission spectra.

An accurate model of dust evolution on galactic scales needs to account for the main mechanisms of the dust life cycle. It is generally believed that under typical ISM conditions in Milky Way-like galaxies three processes dominate: i) production from stellar sources that create the initial 'seeds' of the dust grain populations, ii) dust growth by gas-phase metal accretion onto preexisting dust grains, and iii) dust destruction by sputtering in supernovae (SNe) shocks and in hot, diffuse gas. An accurate model for these processes must also be coupled with a chemical evolution model since the evolution of dust is directly dependent on the evolution of refractory elemental abundances during a galaxy's life. One of the first detailed analytic models to accomplish this was developed by Dwek (1998). They integrated a dust evolution model into a one-zone and one-phase (averaging over properties of the ISM and vertical direction of the disk) chemical evolution model of the Milky Way. Although they were unable to accurately model spatial variations in dust properties or dust formation in molecular clouds, their model reproduced observed galaxy-integrated dust properties (specifically a steady-state D/Z ≈ 0.4 similar to that in the MW; Dwek 1998; Draine & Li 2007).

Owing to the success and simplicity of Dwek (1998) model, it has served as the core framework for most recent numerical dust evolution models on galactic scales. One of the first of these was presented in Bekki (2013) who modeled dust evolution coupled to gas in smoothed particle hydrodynamics (SPH) models of disk galaxies and added modeling of H_2 formation on the surface of dust grains. This model's main limitation was an assumed constant accretion and destruction timescale that was independent of local ISM conditions. In later work (Bekki, 2015a), the accretion timescale is scaled with the density and temperature of the gas. In Bekki (2015b), a live dust particle model was introduced which decoupled the gas and dust particles. A dust evolution model has also been implemented in the moving-mesh code AREPO and used in a suite of cosmological zoom-in simulations of Milky Way-like galaxies (McKinnon et al., 2016). Their model closely follows that of Bekki (2015a), with a coupling of the dust destruction timescale to the local supernova rate being the main modification. Supplemental work added thermal gas-dust sputtering (McKinnon et al., 2017) and decoupling of gas and dust particles with dust grain size evolution (McKinnon et al., 2018), with this framework becoming a recent staple for numerous galaxy simulations (e.g. Li et al., 2019; Aoyama et al., 2020). In another vein, a more comprehensive analytical dust evolution model was presented by Zhukovska et al. (2008) which included detailed AGB dust yields, incorporated a molecular cloud evolution model to restrict dust accretion to only molecular clouds, and restricted dust accretion based on the chemical make up of dust species. In later works (Zhukovska et al., 2016, 2018), the model was incorporated into short-term hydrodynamic simulations of a Milky-Way like disc with molecular clouds and the gas-dust accretion was modified to account for temperature dependent sticking efficiencies and ion-grain interactions for both silicate and metallic iron dust species. A middle ground between these divergent methods has also been presented by Granato et al. (2021) which incorporated chemically distinct dust species, similar to Zhukovska et al. (2008), with two-size approximate dust grain size evolution (Hirashita, 2015; Aoyama et al., 2017; Gjergo et al., 2018) and was used in cosmological zoom-in simulations of an isolated disc galaxy with a sub-resolution star formation and feedback model. While all of these models agree with observations to varying degrees a detailed comparison between them under similar conditions has not been carried out.

In this work, we develop two separate implementations of dust evolution based on the approaches discussed above with a more detailed and varied set of dust physics. One tracks generalized dust species and utilizes a simple, 'tunable' dust growth routine and the other tracks specific dust species with set chemical compositions and incorporates a physically motivated, two-phase dust growth routine. We integrate both of these dust evolution routines into the magneto-hydrodynamics meshless-finite mass code GIZMO coupled with the FIRE-2 (Feedback in Realistic Environments)[1] model for stellar feedback and ISM physics, which is the first application for both models in simulations which resolve whole galaxies and routinely resolve gas phase structure down to $\lesssim$10 K and molecular cloud core densities of $\sim 10^4$ cm^{-3}. We also incorporate a sub-resolution treatment of dense molecular gas chemistry into both routines, and in the case where we track specific dust species, we investigate the inclusion of theoretical dust species to account for the gas-phase depletions of O and Fe.

[1] See the FIRE project web site: http://fire.northwestern.edu

This paper is organized as follows. We layout the framework for our dust evolution model and describe the separate "Elemental" and "Species" implementations in Section 2.3. In Section 2.4, we describe the simulations we use for both implementations, testing the sensitivity of our models to free parameters in Section 2.4.1 and comparing the results of our models to local Milky Way and extragalactic observations in Section 2.4.2 and 2.4.3. Finally, we present our conclusions in Section 2.5.

2.3 Methods

To study the evolution of dust in and its effects on galaxies we utilize simulations of an idealized, non-cosmological Milky Way-like galaxy running two separate dust evolution models incorporated into the GIZMO code base (Hopkins, 2015) and coupled with FIRE-2 stellar feedback and ISM physics. FIRE-2 is an update of the FIRE star-formation and stellar feedback model (Hopkins et al., 2014). Detailed description is available in Hopkins et al. (2018a), but a general overview along with the modifications we made are explained below in Sec. 2.3.1. The initial conditions used in our simulations are presented in Sec. 2.3.2. Our two dust evolution models are based on earlier work by Bekki (2013); McKinnon et al. (2016, 2017) or Zhukovska et al. (2008, 2016, 2018) that we extend, modify, and adjust to the FIRE-2 model as explained in detail in Sec. 2.3.3.

2.3.1 Galaxy Feedback Mechanisms

All simulations in this work are run with the GIZMO code base in the meshless finite-mass (MFM) mode with FIRE-2 model of star formation, and stellar feedback. FIRE-2 incorporates multiple sources of stellar feedback, specifically stellar winds (O/B and AGB), ionizing photons, radiation pressure, and supernovae (both Types Ia and II). Gas cooling is followed self-consistently for T = 10 - 10^{10} K including free-free, Compton, metal-line, molecular, fine-structure, and dust collisional processes while gas is also heated by cosmic rays, photo-electric, and photoionization heating by both local sources and a uniform but redshift dependent meta-galactic background (Faucher-Giguère et al., 2009), including the effect of self-shielding[2]. Star formation is only allowed in cold, molecular, and locally self-gravitating regions with number densities above $n_{\rm H} = 1000\,{\rm cm}^{-3}$.

Each star particle represents a stellar population with a known mass, age, and metallicity assuming a Kroupa (2002) initial mass function (IMF) from $0.1 - 100\,{\rm M}_{\odot}$. The luminosity, mass loss rates, and SNe II rates of each star particle are calculated based on the STARBURST99 (Leitherer et al., 1999) libraries, and SNe Ia rates following Mannucci et al. (2006). Metal yields from SNe II, Ia, and AGB winds are taken from Nomoto et al. (2006), Iwamoto et al. (1999), and Izzard et al. (2004) respectively. Evolution of eleven species (H, He, C, N, O, Ne, Mg, Si, S, Ca, and Fe) is tracked for each gas cell. Sub-resolution turbulent metal diffusion is modeled as described in Su et al. (2017) and Escala et al. (2018). For future reference, FIRE-2 adopts the older Anders & Grevesse (1989) solar metal abundances with $Z \sim 0.02$ so whenever we mention solar abundances we are referring to the Andres & Gravesse abundances.[3]

FIRE has been successful in matching a wide range of observations related to galaxies, including the mass-metallicity relation and its evolution over redshift (Ma et al., 2016) and the Kennicutt–Schmidt star formation law (Orr et al., 2018). This success is owed to the high resolution, star formation criteria, cooling to low temperatures, and multi-channel stellar feedback of FIRE, all of which result in a reasonable ISM phase structure and giant molecular cloud (GMC) mass function (Benincasa et al., 2020). These also lead to the self-consistent development of galactic winds that eject large amounts of gas (Muratov et al., 2015; Anglés-Alcázar et al., 2017) and metals (Muratov et al., 2017; Hafen et al., 2019; Pandya et al., 2021) out of galaxies, preventing excessive star formation and leading to a plausible stellar-halo mass relation.

[2]Note that all cooling and heating processes and radiative transfer modeled in FIRE-2 are not coupled with our dust evolution models. Specifically, dust heating and cooling and radiative transfer assume a constant D/Z ratio and metal-line cooling assumes no metals are locked in dust. In future works, we will fully integrate our dust evolution models with FIRE and investigate the effects on galaxy evolution.

[3]In Appendix 2.E we provide a preliminary comparison of our dust evolution model results incorporated into both FIRE-2 and FIRE-3. While FIRE-3 incorporates numerous improvements, including adoption of the newer Asplund et al. (2009) proto-solar abundances with $Z \sim 0.014$, we find our results are primarily sensitive to the adopted nucleosynthesis yields.

Furthermore, the FIRE model is ideally suited for examining dust evolution due to its in-depth treatment of the multi-phase ISM and tracking of principle heavy elements that make up carbonaceous and silicate dust in gaseous form as a product of stellar evolution. Also, in contrast to most other cosmological simulations, FIRE time-resolves individual SNe events (Hopkins et al., 2018b) and models their interaction with the ISM. This is particularly relevant for dust evolution, since SNe are one of the main creators and destroyers of dust. Being able to time-resolve individual SNe events allows us to track the local variability of dust in the ISM.

For this work, we made a few, specific, changes to the underlying stellar population model in FIRE to enable more accurate treatment of dust production from AGB stars. Specifically, the age at which a stellar population switches from producing a majority O/B winds to AGB winds is changed from 100 Myr to 37.5 Myr to match the end of SNe II, and the stellar winds mass return is modified to more accurately follow results from Leitherer et al. (1999) past stellar ages of 3.5 Myr, specifically the IMF-average mass-loss rate of a stellar population of mass M_* and age $t_{\rm Myr}$ in Myr is $\dot{M}_{\rm w} = 29.4(t_{\rm Myr}/3.5)^{-1.3} M_*\ {\rm Gyr}^{-1}$ for $t_{\rm Myr} > 3.5$. Together, these changes increase the cumulative AGB stellar yields by a factor of ~2.5. We will later show in Sec. 2.4.1 that these changes only affect the early-time dust production, and have no effect on the steady-state dust population.

2.3.2 Initial Conditions

In this paper, we utilize an idealized, non-cosmological Milky Way-like galaxy. Specifically we initialize a disc galaxy with $M_{\rm disc,gas} = 0.9 \times 10^{10}\,M_\odot$ and $M_{\rm disc,*} = 4.7 \times 10^{10}\,M_\odot$ and an exponential gas and stellar density profile $\rho(R,z) \propto e^{-R/R_{\rm d}} e^{-|z|/z_{\rm d}}$ with radial scale lengths of $R_{\rm d,gas} = 6.4$ kpc and $R_{\rm d,*} = 3.2$ kpc respectively and vertical scale length of $z_{\rm d} = 0.25$ kpc for both. We also include a stellar bulge with $M_{\rm bulge} = 1.5 \times 10^{10}\,M_\odot$ and a Hernquist profile (Hernquist, 1990). The galaxy is embedded in a NFW profile (Navarro et al., 1996) dark matter halo with $M_{\rm vir} = 1.5 \times 10^{12}\,M_\odot$ and halo concentration of $c = 12$. We use a gas cell mass resolution of $\sim 2 \times 10^4\,M_\odot$ with adaptive softening lengths, achieving a minimum softening length of $\epsilon_{\rm gas}^{\rm MIN} \approx 10$ pc at simulation end. The dark matter particles have a mass resolution of $\sim 3 \times 10^6 \, M_\odot$ with a universal softening length of $\epsilon_{\rm DM} \approx 40$ pc. All gas cells and star particles start with an initial $Z = Z_\odot$, star particles initially have a uniform age distribution over 13.8 Gyr, and gas cells are initially free of dust. The galaxy was simulated for ~1.5 Gyr, long enough for all dust evolution models to reach a steady-state D/Z ratio and dust population composition as we show in Sec. 2.4.1. The galaxy undergoes a roughly constant star formation rate of $\sim 1 \, M_\odot/\rm yr$ throughout the simulation, producing a median gas metallicity within the galactic disc of $Z \approx 1.3 Z_\odot$ at simulation end. To test the sensitivity of our results to our initial metallicity and dust population we ran two simulations, using our preferred dust evolution model, with either reduced initial metallicity or an initial dust population. We present the specific initial conditions and their results in Appendix 2.A, finding little difference in our results beyond small systematic offsets.

2.3.3 Dust Evolution

In this work we examine two separate implementations of dust evolution whose general methodology can be traced to the semi-analytic model of Dwek (1998):

Dust by Element: "Elemental"

This implementation is motivated by and largely follows numerical hydrodynamic galaxy simulations by Bekki (2013) and McKinnon et al. (2016, 2017). It follows the evolution of individual elements (C, O, Si, Mg, and Fe) within dust, assuming they comprise carbonaceous and generalized (no set chemical composition) silicate dust species. A major consequence of such an approach, which we discuss in detail later on, is the possibility of locking the entirety of all elements into dust. This implementation also relies on explicit tuning of a few free parameters which encompass a vast range of 'sub-grid' dust physics and is effectively single-phase since it does not restrict dust processes to certain gas environments, most notably gas-dust accretion. In this dust evolution model we track the fraction of mass for each element locked up in dust for each gas cell.

Dust by Species: "Species"

We have also implemented a more physically and chemically motivated dust evolution model based on Zhukovska et al. (2008, 2016, 2018). This implementation tracks the evolution of specific dust species (silicates, carbonaceous, and silicon carbide), concentrating on the most abundant species that originate from stars that are also found as presolar dust grains in meteorites. We also consider metallic iron dust since it should theoretically be produced in stellar outflows and SNe and may be needed to explain observed Fe depletions which cannot be explained by Fe in silicate dust alone (Dwek, 2016). In this implementation we track both the fraction of mass for each element locked up in dust for each gas cell and the mass fraction of each gas cell comprised of each dust species (e.g. $M_{\rm dust,silicate}/M_{\rm gas}$). This implementation is also effectively two-phase due to the inclusion of a more physically motivated dust growth model which is discussed below. Owing to its more realistic accounting of elements locked in dust and complex dust growth model this is our preferred implementation. Several aspects require special attention in this method as discussed below (common approaches between our two methods are discussed as they appear).

Carbonaceous: For both implementations the fraction of total carbon locked up in CO molecules ($f_{\rm CO}$) must be taken into account since it is unavailable for carbonaceous dust growth, limiting the maximum formable amount. Observations indicate a $f_{\rm CO}$ ratio of 20% to 40% (e.g. Irvine et al., 1987; van Dishoeck et al., 1993; van Dishoeck & Blake, 1998; Lacy et al., 1994) in Milky Way molecular clouds. It has also been found that atomic C to CO formation progresses rapidly as gas transitions from the diffuse to dense molecular regime (Liszt, 2007; Burgh et al., 2010), making CO the dominant host of gas-phase C in dense molecular clouds. Therefore, to accurately determine $f_{\rm CO}$ beyond assuming a set fraction we must know what gas is in the dense molecular regime and track its evolution. Since typical FIRE-2 simulations only resolve the high-mass end ($> 10^5\ M_\odot$) of the GMC spectrum (Benincasa et al., 2020), we devised a sub-resolution prescription to track the mass fraction of each gas cell in the dense molecular phase $f_{\rm dense}$ (where we assume nearly all gas-phase metals are neutral and specifically gas-phase carbon is almost completely molecular in the form of CO), and with it $f_{\rm CO}$, which is described in Appendix 2.B. Note that this prescription takes into account the depletion of gas-phase C into dust (which limits the maximum formable amount of CO) when calculating $f_{\rm CO}$.

Silicates: Our prescription for silicate dust composition follows that in Zhukovska et al. (2008) consisting of an olivine ($[Mg_xFe_{(1-x)}]_2SiO_4$) and pyroxene ($Mg_xFe_{(1-x)}SiO_3$) mixture which is assumed to be constant. The fraction of olivine in the mixture is represented as $f_{\rm ol}$. The fraction of the silicate structure (assumed to be the same for olivine and pyroxene for simplicity) incorporating Mg is represented as x.[4] Traditionally x and $f_{\rm ol}$ are chosen to reproduce observed depletions of Si and Mg, assuming depleted gas-phase Si and Mg is predominantly locked up in silicate dust. With the observed number abundance ratio of elements Si and Mg bound in dust ($A_{\rm Mg}/A_{\rm Si}$), $f_{\rm ol}$ is related to x through the simple relation $f_{\rm ol} = \frac{A_{\rm Mg}}{xA_{\rm Si}} - 1$. One issue with this method is its sensitivity to the assumed solar abundances (particularly either Lodders (2003) or Asplund et al. (2009) solar abundances) which give observed values of $A_{\rm Mg}/A_{\rm Si} = 1.02 - 1.3$[5] in the cold neutral medium (CNM) (Dwek, 2005; Jenkins, 2009; Draine, 2011). A more recent approach involves direct observation of dust absorption features in the spectra of bright X-ray binaries in combination with direct synchrotron measurements of X-ray absorption fine structure features for numerous silicate compositions. These observations are focused near the Galactic center and probe dust composition and structure in dense environments ($N_{\rm H} \geq 0.5 \times 10^{22}$ cm^{-3}), giving $f_{\rm ol}$ close to unity and $x \approx 0.5$ (Zeegers et al., 2019; Rogantini et al., 2020). These results are complicated by the small sample size and the fact that they probe a much denser phase of the ISM than the CNM. There are also X-ray observations in the CNM which point to entirely iron-free ($x = 1$) silicate crystal structure with separate metallic iron inclusions (Costantini

[4]For clarity, olivine is comprised of both Mg_2SiO_4 and Fe_2SiO_4 and similarly pyroxene is a mixture of $MgSiO_3$ and $FeSiO_3$. So x represents the fraction of the olivine and pyroxene structure incorporating Mg, while the fraction incorporating Fe is $(1-x)$.

[5]Assuming Anders & Grevesse (1989) solar abundances gives $A_{\rm Mg}/A_{\rm Si} \sim 1.08$.

et al., 2012).[6] Due to these uncertainties we chose to follow the traditional approach, assuming $A_{\rm Mg}/A_{\rm Si} = 1.06$ and set $x = 0.65$, and thus $f_{\rm ol} = 0.63$. We determine this value for x by matching the observed silicate-to-carbon dust mass ratio of 2 in the local diffuse ISM (Dwek, 2005) given our maximum theoretical carbon and silicate dust masses for our assumed solar metal abundances and silicate dust composition. Our choice of $A_{\rm Mg}/A_{\rm Si}$ does not greatly affect the maximum amount of formable silicate dust, with only a change of < 10% between $A_{\rm Mg}/A_{\rm Si} = 1.02 - 1.3$, but it does affect the exact depletion patterns of Mg and Si which we comment on in more detail later.

Oxygen: Additional discretion must be given with regards to oxygen in silicate dust since observed oxygen depletions in the Milky Way (Jenkins, 2009) cannot be accounted for by silicate dust alone (Whittet, 2010). If we allow oxygen to only deplete into silicate grains, in the "Species" implementation, the maximum possible oxygen depletion and resulting D/Z ratio end up markedly lower than what is observed. The question of where this oxygen goes is still open with a plethora of proposed candidates such as thick ice mantles on large dust grains (Poteet et al., 2015), μm-sized ice grains (Wang et al., 2015), and organic carbonates on the surface of dust grains (Jones & Ysard, 2019). We thus opt for a simple and optional inclusion of an Oxygen Reservoir (O-reservoir) dust species set to match observed oxygen depletion which we describe below.

First, we determine the dependence of gas-phase oxygen depletion on the hydrogen number density. To this end, we use observations of oxygen depletion and the derived relation between oxygen depletion and mean sight line neutral hydrogen number density, $\langle n_{\rm H,neutral} \rangle$ [cm^{-3}], from Jenkins (2009) to define the fractional amount of O in dust, $D(\rm O)$, as

$$D(\mathrm{O}) = 1 - 0.654 \left(\frac{1 \ \mathrm{cm}^{-3}}{\langle \mathrm{n_{H,neutral}} \rangle} \right)^{0.1} . \tag{2.1}$$

[6]The true role of iron in silicate chemical composition will be better understood with future instruments allowing for the direct X-ray observation of Mg, Si, and Fe absorption K-edges simultaneously (Rogantini et al., 2018)

This relation is observed up to $\langle n_{\rm H,neutral} \rangle \approx 10$ cm^{-3}, but we extrapolate it to higher densities. This also does not consider O in CO or in O-bearing "ices" as neither of these depletion sources exist over the observed range. With this in mind, we set the maximum of this relation to $1 - f_{\rm O\,in\,CO}$ where $f_{\rm O\,in\,CO}$ is the fractional amount of O in CO derived from our prescription for tracking C in CO discussed earlier. Since converting mean sight line density $\langle n_{\rm H,neutral} \rangle$ to physical 3D density $n_{\rm H,neutral}$ is a complicated, multi-faceted problem we assume $\langle n_{\rm H,neutral} \rangle \approx n_{\rm H,neutral}$ for simplicity, which can be taken as an upper bound on the expected depletion at a given number density in our simulations since $\langle n_{\rm H,neutral} \rangle$ will always be significantly lower than the true physical density.

In addition, assuming this O-reservoir dust species is tied to the local amount of dust, and to enable variation in $D(\rm O)$, we scale $D(\rm O)$ by the fraction of the maximum formable amount of silicate dust currently present in the gas cell, $f_{\rm sil}$, given local element abundances. Thus the fraction of oxygen in the gas we put into the O-reservoir is

$$f_{\rm O\text{-}res} = f_{\rm sil}\, D(\rm O) - f_{\rm O\;in\;sil} \tag{2.2}$$

where $f_{\rm O\;in\;sil}$ is the maximum fraction of oxygen that can be trapped in silicate dust. Note we only manually set $f_{\rm O\text{-}res}$ to match Eq. 2.2 when silicate dust grows through gas-dust accretion. Otherwise the O-reservoir is treated as its own distinct dust population experiencing the same destruction processes as the other dust species. The "Elemental" routine avoids this unidentified oxygen depletor issue by allowing oxygen to accrete freely onto dust grains assuming it is in the form of water ice as stated in Dwek (1998).

Iron: The exact form of solid-phase iron dust is unknown and no easily identifiable spectroscopic features exist making direct observation of such species difficult. Two prominent theories for solid-phase iron are free-flying iron nanoparticles (Gioannini et al., 2017; Hensley & Draine, 2017) and iron and FeS inclusions in silicate grains (Min et al., 2007; Jones et al., 2013), with in situ studies on interstellar grains demonstrating silicate particles containing iron and the existence of individual iron particles (Westphal et al., 2014; Altobelli et al., 2016). Also, as previously mentioned, the exact role of atomic iron in silicate dust chemical composition, either directly integrated in the silicate crystal structure, incorporated purely as metallic iron inclusions, or some mixture of the two, is unclear. With this in mind we examine two separate prescriptions for iron dust. 1) **Normal-iron** assumes entirely free-flying metallic iron dust with the same grain size distribution as silicates such as that implemented in Zhukovska et al. (2008), and 2) **Nano-iron** assumes free-flying metallic iron nanoparticles which can be locked into silicate dust as inclusions. Specifically, if any silicate dust is present we lock a set fraction $f_{\rm incl} = 0.7$ of this nanoparticle dust into silicates as inclusions which are protected from SNe destruction, unless all dust is destroyed, and unavailable for gas-dust accretion as implemented in Zhukovska et al. (2018). For simplicity, we assume that the metallic iron dust inclusions contribute to the atomic iron needed in the aforementioned silicate dust composition. This means silicate dust growth via gas-dust accretion will not be hampered by the depletion of gas-phase iron into metallic iron dust since said dust is effectively accreting onto silicate dust and then locked into the dust structure as inclusions. One caveat of this prescription is the total amount of iron in the silicate dust structure can exceed the amount given by our choice of $f_{\rm ol}$ and x discussed earlier.[7] Any differences between these prescriptions will be noted in the proceeding sections.

Both implementations include the dominant sources of dust production and the dominant dust destruction mechanisms. Specifically, we track and differentiate between dust created from SNe Ia and II, AGB stars, and gas-phase accretion in the ISM and account for dust destroyed by SNe shocks, thermal sputtering, and astration. We also incorporate sub-resolution turbulent dust diffusion in the same manner as the turbulent metal diffusion already in FIRE-2. Other mechanisms, such as dust shattering and coagulation, will be left to future work. An illustration of these mechanisms can be seen in Figure 2.1. We now describe these processes in more detail.

[7] Note that the difference in optical properties of silicate dust with iron inclusions versus iron being directly included in the silicate structure are small (Jones et al., 2013, see Appendix A)

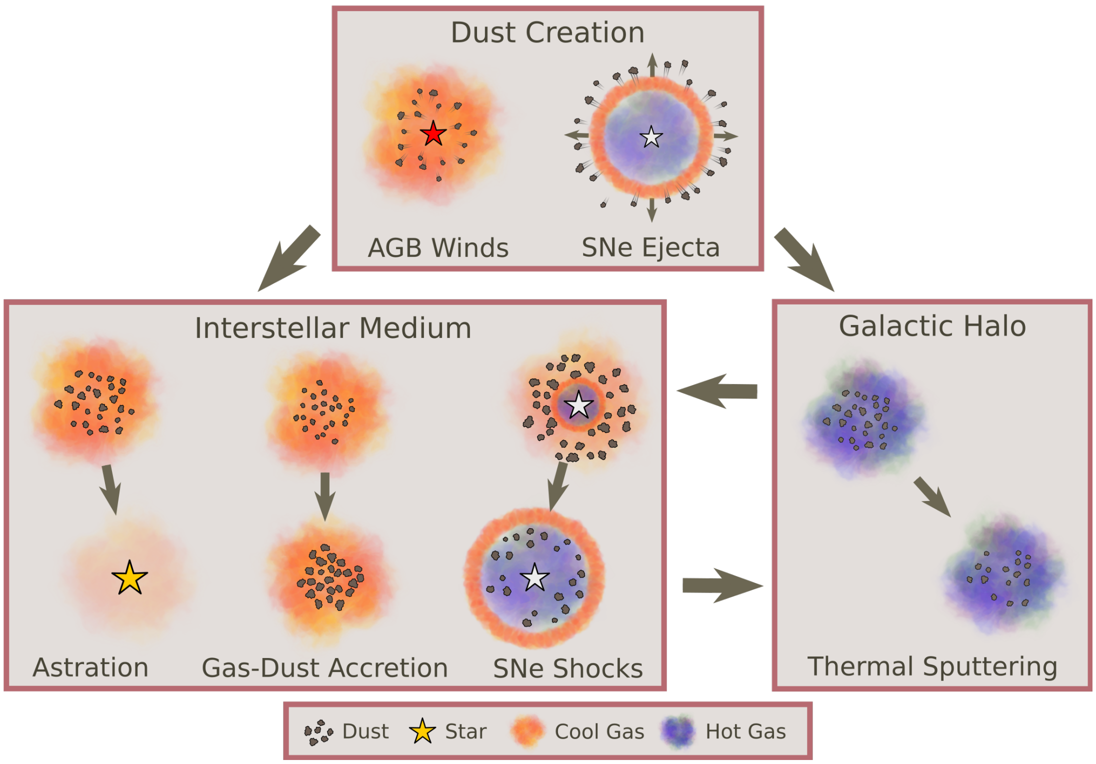

Figure 2.1. Pictorial representation of mechanisms composing the dust life cycle included in our dust evolution models. **Dust Creation:** The initial 'seeds' of the dust population are created in the stellar ejecta of SNe and AGB winds where a portion of ejected metals condense into dust. Once these 'seeds' have been created they spend their life in the ISM and/or the galactic halo where they are exposed to various processes. **Gas-Dust Accretion:** In cool, dense phases of the ISM, gas-phase metals accrete onto the surface of preexisting dust grains growing the grains over time. This is believed to be the main source of dust mass in the MW. **SNe Shocks:** As supernovae remnants propagate through the ISM they destroy and shatter dust grains residing in the ISM via grain-grain collisions, thermal sputtering, and non-thermal sputtering. This is believed to be the main destroyer of dust in the MW. **Astration:** As gas cools and collapses forming stars, dust residing in said gas is also destroyed and contributes to the stellar metallicity. **Thermal Sputtering:** Dust grains residing in hot gas, such as in the galactic halo, are eroded and destroyed by energetic atoms.

2.3.4 Dust Creation

Dust Creation by SNe

The exact dust yields from SNe are not well known and so both of our implementations follow the same simplified prescriptions from Dwek (1998) which assumes a set fraction of the metal yields from SNe condense into dust.

Elemental: For this implementation we follow the typical approach used in existing galaxy formation models. Specifically, for both SNe Ia and SNe II the dust mass for a given element i is given by

$$\Delta M_{i,\mathrm{elem}} = \begin{cases} \delta_{\mathrm{C}}^{\mathrm{SN}} \Delta M_{\mathrm{C}} & \text{if } i = \mathrm{C} \\ \mu_{\mathrm{O}} \sum\limits_{k=\mathrm{Mg,Si,Fe}} \delta_k^{\mathrm{SN}} \Delta M_k / \mu_k & \text{if } i = \mathrm{O} \\ \delta_i^{\mathrm{SN}} \Delta M_i & \text{if } i = \mathrm{Mg, Si, Fe} \end{cases} \tag{2.3}$$

where δ_i^{SN} is the dust condensation efficiency for element i whose value can be found in Table 2.1. These choices for SNe efficiencies are originally stated by Dwek (1998) as arbitrary, but they do reproduce similar results to more detailed theoretical dust yields modeled in Todini & Ferrara (2001) and produce similar dust masses as some observations (Chawner et al., 2019; De Looze et al., 2019), but are in contention with others (Sugerman et al., 2006; Rho et al., 2008; Lau et al., 2015). For silicates, a majority of the refractory elements, Mg, Si, and Fe, and an equal amount of O by number are assumed to condense into dust. In the rare case this prescription requires more O for silicate dust than the total available O, we scale down silicate dust production to not exceed this O limit.

Species: This implementation is similar, but makes a distinction between SNe Ia and SNe II, assuming SNe II produce all dust species while SNe Ia may only theoretically produce some iron dust. This is due to recent observations and modelling that suggests SNe Ia produce little, if any, dust (Nozawa et al., 2011; Gomez et al., 2012). In either case, the amount of dust species returned in one SNe event is tied to the total mass return of the key element[8] required to form the given dust species. The dust condensation efficiencies for silicates, carbon, and SiC are determined by comparing to observed abundance ratios of presolar dust grains from supernova and AGB found in meteorites. This process is explained in detail in Zhukovska et al. (2008), but it should be noted that the observations for some of the dust species are somewhat limited and produce relatively low condensation efficiencies, which contradict some observations (e.g. SNe 1987a is observed to have near all ejecta condensed into dust Matsuura et al. 2011, 2015). The condensation efficiencies for iron dust are arbitrarily set to a low nonzero values, but they very well could be zero. All species condensation efficiencies can be found in Table 2.1.

Thus, for a single SNe event the dust mass returned for a given species j is given by

$$\Delta M_{j,\mathrm{spec}} = \delta_j^{\mathrm{SN}} \Delta M_{\mathrm{key},j} \frac{A_j}{A_{\mathrm{key},j}}, \tag{2.4}$$

where $\Delta M_{\mathrm{key},j}$ and $A_{\mathrm{key},j}$ are the returned mass and atomic mass of the key element for species j and A_j is the atomic mass of one formula unit of species j. The dust masses contributed by each element are then updated based on their mass fraction in species j.

The overall SNe dust species production for both routines is shown in Figure 2.2. The "Elemental" SNe routine produces more carbonaceous and silicate dust overall and is dominated by silicate dust in contrast to the "Species" SNe routine which is dominated by carbonaceous dust.

Dust Creation by AGB Stars

Near the end of an AGB star's life a certain amount (ΔM_{dust}) of the stellar wind injected into the surrounding gas condenses into dust. The type of dust that forms at this end stage depends on the evolution of the stellar surface carbon-to-oxygen number ratio (C/O) during the

[8]Here key element refers to the element for which N/i has the lowest value, where N is the number of atoms of the element in the initial SNe ejecta and i is the number of atoms of the element in one formula unit of the dust species under consideration.

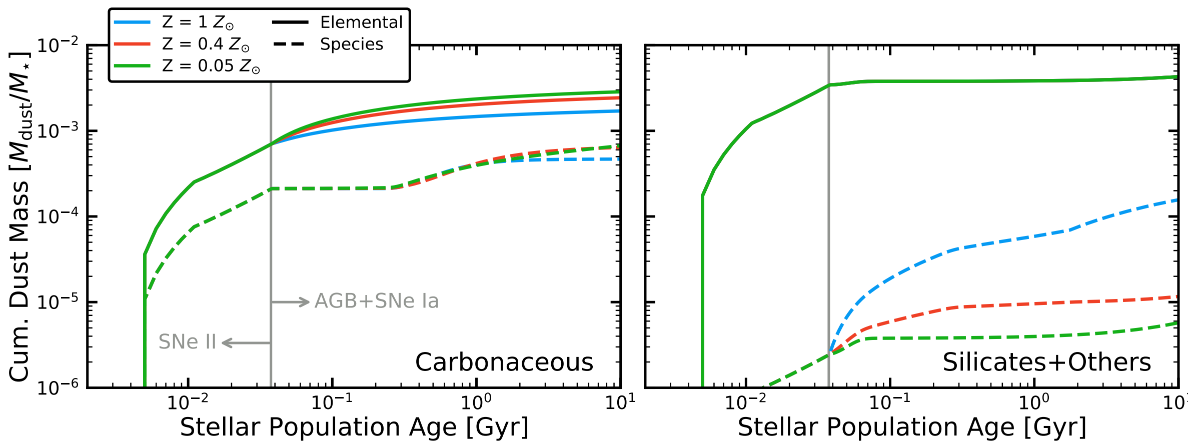

Figure 2.2. Comparison of the cumulative dust production (from all stellar sources) per stellar mass of carbonaceous dust (*left*) and all other dust (dominated by silicates) (*right*) over the lifetime of a stellar population for the "Elemental" (*solid*) and "Species" (*dashed*) implementations with various initial stellar metallicities. The grey line shows when the transition between SNe II and SNe Ia/AGB dust production occurs at $t \approx 0.0375$ Gyr. Note the drop in AGB carbonaceous dust with higher metallicity is due to the stellar surface C/O ratio that determines the type of dust that formed. All stars have initial C/O < 1 and increase their stellar surface C abundance via mixing. This means higher metallicity stars have higher initial surface C and O content, requiring more mixing to achieve C/O > 1, which may not be possible before the end of the AGB phase. Ultimately, this leads to less carbonaceous dust being formed when compared to low metallicity stars. A more detailed breakdown of these results can be found in Ferrarotti & Gail (2006) and Sec. 2.3 of Zhukovska et al. (2008). We also note that the "Elemental" AGB dust routine only produces carbonaceous dust since it is coupled with FIRE-2 time- and IMF-averaged AGB metal yields which never produce surface C/O < 1, effectively making the "Elemental" silicate dust production metallicity independent since it is only produced by SNe.

AGB phase, which is governed by the initial mass and metallicity of the star. In carbon rich outflows most oxygen is tied up in CO molecules, so mainly carbonaceous dust is produced. Conversely, in oxygen rich outflows most carbon is tied up in CO molecules, so mainly silicate dust is produced (Draine, 1990; Ferrarotti & Gail, 2006).

Elemental: For this implementation we take a simple "leftover" approach for carbonaceous and silicate dust production, which depends on the carbon-to-oxygen number abundance ratios $C/O > 1$ or $C/O < 1$ in the stellar outflow. It is assumed that either all the O or C in AGB outflows is locked up into newly formed CO molecules depending on which is less abundant by number, while the remainder of the more abundant element forms into dust. Specifically, if $C/O > 1$ the excess C condenses into carbon dust while for $C/O < 1$, a majority of the refractory elements, Mg, Si, and Fe, and an equal amount of O by number condense into silicate dust, similar to the SNe prescription. Thus for a given stellar population and ΔM_i, the ith element stellar outflow metal mass which is tabulated from standard stellar population models (STARBURST99; Leitherer et al. (1999)) assuming a Kroupa (2001) IMF, we calculate the dust mass produced by AGB stars accordingly. For AGB stars with C/O > 1 in their stellar outflows, the amount of dust of element i produced is given by

$$\Delta M_{i,\mathrm{elem}} = \begin{cases} \delta_{\mathrm{C}}^{\mathrm{AGB,C/O>1}}(\Delta M_{\mathrm{C}} - 0.75\Delta M_{\mathrm{O}}) & \text{if } i = \mathrm{C} \\ 0 & \text{otherwise.} \end{cases} \tag{2.5}$$

For AGB stellar outflows with C/O < 1 it is given by

$$\Delta M_{i,\mathrm{elem}} = \begin{cases} \delta_i^{\mathrm{AGB,C/O<1}} \Delta M_i & \text{if } i = \mathrm{Mg,Si,Fe} \\ \mu_{\mathrm{O}} \sum\limits_{k=\mathrm{Mg,Si,Fe}} \delta_k^{\mathrm{AGB,C/O<1}} \Delta M_k/\mu_k & \text{if } i = \mathrm{O} \\ 0 & \text{otherwise,} \end{cases} \tag{2.6}$$

where μ_k is the atomic mass in AMU of element k and $\delta_{\rm C}^{\rm AGB,C/O>1}$ and $\delta_i^{\rm AGB,C/O<1}$ are the dust condensation efficiencies, whose values can be found in Table 2.1. In the rare case this prescription requires more O for silicate dust than the total available O not locked in CO, we scale down silicate dust production to not exceed this O limit. We emphasize that for C/O and ΔM_i in Eq. 2.5 & 2.6 we use the time- and IMF-averaged stellar metal yields in FIRE-2 and not the metal yields for individual stars which can under- or over-predict the total amount of dust formed. Specifically only one dust species is allowed to form for each stellar wind event and the IMF-averaged C/O ratio can be markedly different from the individual stellar C/O. Furthermore, the FIRE-2 metal yields never satisfy C/O < 1, so we should expect AGB stars to only produce carbonaceous dust for this implementation.

Species: This implementation uses the Zhukovska et al. (2008) AGB dust production results which they extended from Ferrarotti & Gail (2006) to include a finer grid of metallicities and initial stellar masses. We interpolate this grid to calculate the total dust mass by species produced by AGB stars over their lifetime for a range of metallicities and stellar masses. Using this and averaging over a Kroupa (2001) IMF, we calculate the total AGB production of dust species j for a star particle of a given age, $t_{\rm age}$, and metallicity, Z, over a time step δt as

$$M_{j,\rm spec}(t_{\rm age}+\delta t, Z) = \frac{M_*}{M_\odot}\int_{m(t_{\rm age})}^{m(t_{\rm age}+\delta t)} \Phi(m)\, M_{j,\rm spec}^{\rm AGB}(m,Z)\, dm. \tag{2.7}$$

Here $\Phi(m)$ is the Kroupa (2001) IMF normalized such that $\int m\,\Phi(m)\,dm = 1\,M_\odot$, $m(t)$ is the inverse of the stellar lifetime function which we take to be the main sequence lifetime, giving $m(t)\,[M_\odot] \approx 2.51\,t_{\rm Gyr}^{-0.4}$ which approximately defines the mean mass of stars going through the peak of the AGB dust-production phase, for a well sampled stellar population of age $t_{\rm Gyr}$ in Gyr, $M_{j,\rm spec}^{\rm AGB}(m,Z)$ is the given species dust mass returned by a single star of a given mass and metallicity interpolated from the data table given in Zhukovska et al. (2008)[9], and M_* is the total

[9]As noted by Zhukovska et al. (2008), most of the dust mass created over the lifetime of an AGB star is formed and expelled at the very end of its life when mass loss rates are the highest but the timescales are vanishingly small compared to galaxy dynamical times. This means AGB dust production can be assumed to occur instantaneously at

Table 2.1. Condensation efficiencies for "Elemental" and "Species" implementations taken from Dwek (1998) and Zhukovska et al. (2008). Note that "Elemental" has efficiencies for each elemental species while "Species" has efficiencies for common dust types.

Variable	Elemental	Species
δ_i^{SNII}	0.0 for i = H,He,N,Ne,S,Ca 0.5 for i = C 0.8 for i = O,Mg,Si,Fe	0.00035 for i = silicate 0.15 for i = carbon 0.001 for i = iron 0.0003 for i = SiC
δ_i^{SNIa}	same as δ_i^{SNII}	0.005 for i = iron 0.0 otherwise
$\delta_i^{\mathrm{AGB,C/O>1}}$	0.0 for i = H,He,N,O,Ne,Mg,Si,S,Ca,Fe 1.0 for i = C	refer to Eq. 2.7
$\delta_i^{\mathrm{AGB,C/O<1}}$	0.0 for i = H,He,N,C,Ne,S,Ca 0.8 for i = O,Mg,Si,Fe	refer to Eq. 2.7

mass of the star particle. Since the Ferrarotti & Gail (2006) AGB dust production model uses an assumed AGB metal yields and mass-loss rate prescription different from that in FIRE-2, this can cause more dust to be produced than metals available. If this occurs, we scale down the amount of dust produced for any 'over-budget' dust species.

The overall AGB dust species production for both routines can be seen in Figure 2.2 for $t > 0.0375$ Gyr, which is when the transition between SNe II and SNe Ia/AGB dust production occurs. Owing to high condensation efficiencies assumed in the "Elemental" implementation, it produces far more carbonaceous dust compared to the "Species" implementation. This large difference is not immediately reconcilable since even detailed AGB dust production models calculated from either analytic or full integrated stellar evolution models vary considerably in the amount and type of dust produced across initial stellar masses and metallicities while still producing plausible results. Specifically, both models produce reasonable dust masses and present-time AGB dust production rates compared to those observed for the Magellanic Clouds (e.g. Zhukovska & Henning, 2013; Schneider et al., 2014).

the end of an AGB star's main sequence lifetime.

2.3.5 Dust Growth in the ISM

In dense interstellar clouds, dust grains can grow by the accretion of gas-phase metals onto preexisting dust cores (Draine, 1990). Following work done by Dwek (1998) and Hirashita (1999) we track the instantaneous fractional dust growth of element i via accretion for each gas cell as

$$\left(\frac{\dot{M}_{i,\mathrm{dust}}}{M_{i,\mathrm{dust}}}\right)_{\mathrm{growth}} = \left(1 - \frac{M_{i,\mathrm{dust}}}{M_{i,\mathrm{metal}}}\right)\left(\frac{1}{\tau_{\mathrm{g}}}\right), \tag{2.8}$$

where $M_{i,\mathrm{dust}}$ and $M_{i,\mathrm{metal}}$ are the corresponding element i total dust mass and total metal mass (gas-phase and dust) in the cell respectively and τ_{g} is the characteristic growth time-scale. The $\left(1 - \frac{M_{i,\mathrm{dust}}}{M_{i,\mathrm{metal}}}\right)$ term represents the free gas-phase metal mass fraction.

Elemental: For this implementation each element i accretes independently of one other and adopts a set growth time-scale for all elements, following derivations from Hirashita (2000) to calculate the time-scale τ_{g}. This assumes a set sticking efficiency, computing the growth time-scale as

$$\tau_{\mathrm{g}} = \tau_{\mathrm{g}}^{\mathrm{ref}}\left(\frac{\rho^{\mathrm{ref}}}{\rho}\right)\left(\frac{T^{\mathrm{ref}}}{T}\right)^{1/2}, \tag{2.9}$$

where ρ and T are the density and temperature of the gas cell, ρ^{ref} and T^{ref} are reference values for density and temperature, and $\tau_{\mathrm{g}}^{\mathrm{ref}}$ is an overall normalization factor influenced by the atom-grain collision sticking efficiency, grain cross-section, grain density, clumping factors in the ISM, and many other 'sub-grid' physical processes. Here these are simply taken to be constants, with values similar to those in McKinnon et al. (2016), specifically $\rho^{\mathrm{ref}} = 1$ H atom cm^{-3}, $T^{\mathrm{ref}} = 20$ K and $\tau_{\mathrm{g}}^{\mathrm{ref}} = 2$ Gyr. We note that McKinnon et al. (2016) uses $\tau_{\mathrm{g}}^{\mathrm{ref}} = 0.2$ Gyr which they 'tuned' to Milky Way-sized galaxies, but we will later show that this timescale is far too short for the MW-mass galaxy we simulate.

Species: For this implementation the accretion rate for each dust species j is limited by the key element for that species. This means Eq. 2.8 applies to the dust growth of said key element[10] (which is calculated at each time step) and each dust species j has its own characteristic growth time-scale. From Zhukovska et al. (2008) we use the characteristic accretion growth time-scale

$$\tau_{\mathrm{g},j} = \left(\rho_{\mathrm{c}} V_{\mathrm{grain}}\right) \left(\frac{1}{v_{j,\mathrm{th,m}}\, n_{\mathrm{m}}\, \sigma_{\mathrm{grain}}}\right) \left(\frac{1}{\xi_{\mathrm{m}}\, m_{\mathrm{added}}}\right), \tag{2.10}$$

where the terms in this equation from left to right are the mass of the dust grain, the interaction rate between the growth species[11] and dust grain, and the overall mass added to the dust grain after each interaction. The variables are as follows: ρ_{c} is the mass density of the solid dust grain (taken from Zhukovska et al. 2008), V_{grain} is the volume of the dust grain, $v_{j,\mathrm{th,m}} = \sqrt{\frac{8kT}{\pi A_{j,\mathrm{m}} m_{\mathrm{H}}}}$ is the thermal velocity of the growth species m, n_{m} is the maximum number density of the growth species (i.e. assuming no elements are locked up in dust), σ_{grain} is the surface area of the dust grain, ξ_{m} is the sticking efficiency for each collision, $m_{\mathrm{added}} = A_{j,\mathrm{c}}\, m_{\mathrm{H}}/\alpha_{j,\mathrm{c}}$ is the mass added to the dust grain with each collision, $A_{j,\mathrm{c}}$ and $A_{j,\mathrm{m}}$ are the atomic weight of one formula unit of the dust material under consideration and of the growth species respectively, and $\alpha_{j,\mathrm{c}}$ is the number of atoms of the key element contained in one formula unit of the condensed phase. Note, even with this complexity Eq. 2.10 makes many strong assumptions. It neglects clumping/cross-correlation factors and gas-dust kernel collision enhancement terms, and it assumes negligible dust drift velocity throughout the gas, a uniform internal grain density, and hard-sphere type encounters.

For simplicity we assume that the growth species is just the free atoms of the key element and that dust grains are spherical. With these assumptions, and averaging over the dust grain size distribution, the growth timescale can be written as

$$\tau_{\mathrm{g},j} = \frac{\rho_{\mathrm{c}}\, \langle a \rangle_3\, \alpha_{j,\mathrm{c}}}{3\xi_{\mathrm{m}} v_{j,\mathrm{th,m}} A_{j,\mathrm{c}} m_{\mathrm{H}}\, n_{\mathrm{m}}}, \tag{2.11}$$

[10] Once $\dot{M}_{i,\mathrm{dust}}$ is determined for the key element we assume appropriate masses for all other elements which comprise said dust species are also accreted. These masses are determined by the dust species' chemical composition mentioned previously.

[11] The growth species is the atomic or molecular species in the gas-phase which carries most of the key element for the dust species under consideration.

where $\langle a \rangle_3$ is the average grain size given by

$$\langle a \rangle_3 = \frac{\langle a^3 \rangle}{\langle a^2 \rangle} = \frac{\int_{a_{\rm min}}^{a_{\rm max}} \frac{dn_{\rm gr}(a)}{da}\, a^3\, da}{\int_{a_{\rm min}}^{a_{\rm max}} \frac{dn_{\rm gr}(a)}{da} D(a)\, a^2\, da}, \tag{2.12}$$

where $D(a)$ is the grain size dependent electrostatic enhancement factor which accounts for the change in cross section of an interaction between ionized gas-phase metals and charged dust grains (Coulomb enhancement) (Weingartner & Draine, 1999) and $n_{\rm gr}(a)$ is the grain size distribution with minimum and maximum grain sizes $a_{\rm min}$ and $a_{\rm max}$ respectively.

For simplicity we adopt a MRN size distribution $\frac{dn_{\rm gr}(a)}{da} \propto a^{-3.5}$ (Mathis et al., 1977) for all dust species with $a_{\rm min} = 4$ nm, and $a_{\rm max} = 250$ nm for all dust species besides Nano-iron, which has $a_{\rm min} = 1$ nm and $a_{\rm max} = 10$ nm. In diffuse ISM gas (CNM and diffuse molecular), for silicates and carbonaceous dust we adopt their respective CNM enhancement factors $D(a)$ from Weingartner & Draine (1999), for Nano-iron dust we adopt the enhancement factor for iron nanoparticles from Hensley & Draine (2017), and for Normal-iron dust we assume the same $D(a)$ as silicate dust. In dense molecular gas, where gas-phase metals are neutral, $D(a) = 1$ for all dust species.

For the sticking efficiency, we follow Zhukovska et al. (2016) and take a simple step function with $\xi_{\rm m} = 1$ for $T_{\rm gas} < 300K$ and $\xi_{\rm m} = 0$ for $T_{\rm gas} > 300K$, where $T_{\rm gas}$ is the overall temperature of the gas cell.[12]

Using the values above, Eq. 2.11 numerically evaluates to

$$\tau_{{\rm g},j} = \tau_{{\rm ref},j} \frac{\alpha_{j,{\rm c}}\, A_{j,{\rm m}}^{1/2}}{\xi_{\rm m} A_{j,{\rm c}}} \left(\frac{\rho_{\rm c}}{3\ {\rm g\ cm^{-3}}}\right) \left(\frac{10^{-2}\ {\rm cm^{-3}}}{n_{\rm m}}\right) \left(\frac{300\ {\rm K}}{T}\right)^{1/2}, \tag{2.13}$$

where $\tau_{{\rm ref},j}$ is the normalization calculated as given in Table 2.2 alongside $\rho_{\rm c}$.

[12]Zhukovska et al. (2016) notes that expected depletion trends are not sensitive to the exact shape of the sticking efficiency relation with gas temperature as long as it decreases, but our cutoff choice of $T = 300$K is somewhat arbitrary and prone to uncertainty due to the lack of any experimental data or theoretical calculations for most refractory elements.

Since we track the mass fraction of each gas cell which is in the dense molecular phase (f_{dense}), we replace $\tau_{\mathrm{ref},j}$ with an effective reference timescale $\tau_{\mathrm{ref},j}^{\mathrm{eff}}$ which is defined as

$$\left(\tau_{\mathrm{ref},j}^{\mathrm{eff}}\right)^{-1} = \frac{f_{\mathrm{dense}}}{\tau_{\mathrm{ref},j}^{\mathrm{dense}}} + \frac{1 - f_{\mathrm{dense}}}{\tau_{\mathrm{ref},j}^{\mathrm{diffuse}}} \tag{2.14}$$

where $\tau_{\mathrm{ref},j}^{\mathrm{diffuse}}$ is the reference timescale for dust species j in gas in the CNM and diffuse molecular phase where the electrostatic enhancement factor has to be taken into account and free gas-phase C atoms exist, and $\tau_{\mathrm{ref},j}^{\mathrm{dense}}$ is the reference timescale for dust species j in gas in the dense molecular phase where there is no electrostatic enhancement factor and all gas-phase C is locked into CO.

It should be noted, that for gas in cold ISM phases, our hydro-solver time steps are much shorter than the growth timescales of any dust species which means we can accurately time-resolve gas-dust accretion. Specifically, in molecular gas (with e.g. $n_{\mathrm{H}} = 10^3\ \mathrm{cm}^{-3}$, $T = 30$ K) with solar metal abundances the "Species" growth timescales for each of the dust species without Coulomb enhancing are for silicates $\tau_{\mathrm{g}} \approx 0.66$ Myr, for Normal-iron $\tau_{\mathrm{g}} \approx 8.4$ Myr, and for Nano-iron $\tau_{\mathrm{g}} \approx 0.85$ Myr and for "Elemental" is $\tau_{\mathrm{g}} \approx 1.6$ Myr for all elements. For CNM gas (with e.g. $n_{\mathrm{H}} = 30\ \mathrm{cm}^{-3}$, $T = 100$ K) with solar metal abundances, the "Species" growth timescales for each of the dust species with Coulomb enhancing are for silicates $\tau_{\mathrm{g}} \approx 2.2$ Myr, for Normal-iron $\tau_{\mathrm{g}} \approx 28$ Myr, for Nano-iron $\tau_{\mathrm{g}} \approx 0.19$ Myr, and for carbonaceous $\tau_{\mathrm{g}} \approx 12$ Myr and for "Elemental" is $\tau_{\mathrm{g}} \approx 30$ Myr for all elements. The simulation time steps, in contrast, range from $\sim 10^2 - \sim 10^4$ yr under these conditions.

2.3.6 Dust Destruction

Dust that has been injected and grown in the ISM is subjected to numerous destructive processes which destroy and shatter dust grains, shifting the grain size distribution and reducing the total dust mass. Since we do not evolve the grain size distribution, we explicitly follow destruction only. One process we intrinsically track is astration, the destruction of dust in gas which condenses into stars. Specifically, as star particles form from gas cells or fractions thereof,

Table 2.2. Summary of input constants assumed in our "Species" gas-dust accretion model. We assume SiC does not grow in the ISM and O-reservoir dust follows the prescription outlined in Sec. 2.3.3. The 'diffuse' label denotes the atomic or diffuse molecular gas regime where gas-phase metals are ionized and so accretion includes Coulomb enhancement and C is primarily atomic. The 'dense' label denotes the dense molecular gas regime where we assume essentially all gas-phase metals are neutral and so accretion does not include Coulomb enhancement; meanwhile we assume all gas-phase C is locked into CO, so gas-dust accretion of C cannot occur (the ∞ here).

Physical Quantity	Silicate	Carbon	Normal-iron	Nano-iron	SiC	O-reservoir
ρ_c (g cm^{-3})	3.13	2.25	7.86	7.86	3.21	—
$a_{\rm min}$ (nm)	4	4	4	1	4	—
$a_{\rm max}$ (nm)	250	250	250	10	250	—
$\langle a \rangle_3^{\rm diffuse}$ (nm)	5.8	35.4	5.8	0.038	31.6	—
$\langle a \rangle_3^{\rm dense}$ (nm)	31.6	31.6	31.6	3.2	31.6	—
$\tau_{\rm ref}^{\rm diffuse}$ (Myr)	4.4	26.7	4.4	0.029	∞	—
$\tau_{\rm ref}^{\rm dense}$ (Myr)	23.9	∞	23.9	2.42	∞	—
A_c	143.8	12.0	55.9	55.9	30.1	16.0

the corresponding (cell-averaged) amount of dust is removed (added to the stellar metallicity). The other major dust destruction processes we track are described below.

Thermal Sputtering

Dust grains residing in hot gas in the galactic halo can undergo thermal sputtering, which causes erosion of dust grains by energetic atoms and can limit the depletion of gas-phase metals onto grains. Protons and helium ions are the main sputtering agents, and predictions of thermal sputtering rates indicate that sputtering overwhelms dust growth via accretion for $T \gtrsim 10^5$K (Draine & Salpeter, 1979).

For both the "Elemental" and "Species" implementations we follow the prescription for thermal sputtering from Tsai & Mathews (1995). The sputtering rate for a grain of radius a in gas of density ρ and temperature T is then approximated by

$$\frac{da}{dt} = -(3.2\times 10^{-18}{\rm cm}^4{\rm s}^{-1}) \left(\frac{\rho}{m_{\rm p}}\right) \left[\left(\frac{T_0}{T}\right)^{\omega} + 1\right]^{-1}, \tag{2.15}$$

where m_p is the proton mass, $\omega = 2.5$ controls the low-temperature scaling of the sputtering rate and $T_0 = 2 \times 10^6$ K is the temperature above which the sputtering rate is approximately constant. It is important to note, this makes similar assumptions to Eq. 2.10 ignoring clumping/cross-correlation factors, unresolved phase structure, non-trivial grain compositions, or geometric structures, strong charge effects, dust drift, and many other terms which can significantly alter da/dt. The associated sputtering time-scale for the grain is

$$\tau_{\rm sp} = a\left|\frac{da}{dt}\right|^{-1} \approx (0.17\,{\rm Gyr})\left(\frac{a_{-1}}{\rho_{-27}}\right)\left[\left(\frac{T_o}{T}\right)^{\omega}+1\right], \tag{2.16}$$

where a_{-1} is the grain size in units of 0.1 μm, and ρ_{-27} is the gas density in units of 10^{-27}g cm^{-3}.

Assuming a constant solid grain mass density ρ_g and grain mass $m_g \propto a^3 \rho_g$, Equation 2.16 implies that grain mass changes according to the timescale $|m/\dot{m}| = \tau_{\rm sp}/3$. Averaging over the grain size distribution gives an average grain size similar to Eq. 2.12, but with no Coulomb enhancement ($D(a) = 1$). We again assume an MRN size distribution, $\frac{dn_{\rm gr}(a)}{da} \propto a^{-3.5}$, with $a_{\rm min}$ and $a_{\rm max}$ given in Sec. 2.3.5 which gives an average grain size of $a = \sqrt{a_{\rm min}\, a_{\rm max}} = 0.032$ μm for carbonaceous, silicate, and Normal-iron dust and $a = \sqrt{a_{\rm min}\, a_{\rm max}} = 0.0032$ μm for Nano-iron dust. For "Elemental" we assume $a = 0.032$ μm for all elements in dust.

Thus for each time step we calculate the fractional change in element or species i dust mass for every gas cell due to thermal sputtering as

$$\left(\frac{\dot{M}_{i,\rm dust}}{M_{i,\rm dust}}\right)_{\rm sp} = -\frac{1}{\tau_{\rm sp}/3}. \tag{2.17}$$

SNe Shocks

Supernovae remnants (SNR) destroy and shatter dust grains as they propagate through the ISM through grain-grain collisions, thermal sputtering, and non-thermal sputtering (e.g. Jones et al., 1996). As the SNR expands into the ISM and shock-heats the gas it destroys a fraction of the dust grains in the gas. This dust destruction efficiency, ϵ, depends on the speed of the shock.

For both the "Elemental" and "Species" implementations we follow the results from Cioffi et al. (1988) which consider a radiative SNR. Assuming a homogeneous, solar metallicity medium we calculate the amount of gas shocked to velocity of at least v_s for each SNe event as

$$M_{\rm s}(v_{\rm s}) = 2460 \frac{E_{51}^{0.95}}{n_0^{0.1} v_{\rm s7}^{9/7}} M_{\odot}, \tag{2.18}$$

where n_0 is the number density of the surrounding medium, E_{51} is the energy released in a typical supernova in units of 10^{51} erg, and $v_{\rm s7}$ is the shock velocity in units of 100 km s^{-1}. We take the shock velocity to be $v_{s7} = 1$, i.e. the destruction is only efficient when the shock velocity is larger than $\sim$100 km/s which also roughly corresponds to when the SNR begins to rapidly cool, and assume an average dust destruction efficiency for the shocked gas to be $\bar{\epsilon} \approx 0.4$, meaning typically all dust is destroyed in 980 $M_{\odot}$ of gas by a single SNR. Note this gas mass cleared of dust (and in particular $\bar{\epsilon}$) encompasses numerous parameters such as the detailed SNR structure, grain physics, grain size distribution, etc. which can have large uncertainties, but our prescription is roughly consistent with detailed hydrodynamical simulations of dust destruction via thermal and non-thermal sputtering in SN shocks assuming an MRN grain size distribution (Hu et al., 2019) for all but the most diffuse gas ($n_{\rm H} < 10^{-2}$ cm^{-3}). We then couple the amount of gas cleared of dust to the surrounding gas cells by using the weights calculated in Hopkins et al. (2018b) for mechanical SNe feedback. We also assume the dust is thoroughly mixed so all dust elements/species have equal fractions destroyed. To account for the possible double counting of destruction via thermal sputtering due to our separate thermal sputtering and SNe dust destruction routines, we prevent thermal sputtering from occurring in gas which has been affected by an SNe event in the past 0.3 Myr, which is the typical time it takes for all dust destruction process to cease after a single SNe event (Hu et al., 2019, see Appendix A).

It should be noted that while we keep this prescription for all resolutions, the highest resolution FIRE simulations $m_{\rm gas} \ll 2460\ M_{\odot}$ (which is the case for many simulations of dwarf galaxies, e.g. Wheeler et al. (2019)) can resolve the SNe cooling radius. While actually resolving the processes that destroy dust in SNR (Hu et al., 2019) is beyond the current resolution of FIRE, these high resolution simulations will need a more detailed, time-resolved prescription which tracks the dust destruction efficiency based on the individual shock velocities for surrounding gas cells, but we save this for future work.

2.4 Results

To test both implementations, we simulate an idealized, non-cosmological Milky Way-like galaxy as described in Sec. 2.3.2. The galaxy was simulated for ~1.5 Gyr, long enough for all dust evolution models to reach close to a steady-state D/Z ratio and dust population composition. For all results listed we only consider gas cells within the galactic disc with $r < 20$ kpc from the galactic center and $|z| < 2$ kpc from the disc plane.

We first investigate the sensitivity of the steady-state D/Z of each model to free parameters in Sec. 2.4.1. We then analyze the resulting relation between gas-phase element depletions and D/Z with column and physical gas density along with the effects of our O-reservoir and Nano-iron dust prescriptions and compare with MW observations in Sec. 2.4.2. Lastly, we compare to extragalactic observations of spatially-resolved D/Z in Sec. 2.4.3.

2.4.1 Testing Free Parameters

Due to the numerous uncertainties and assumptions made in both implementations we first evaluate the sensitivity of each fiducial implementation to free parameters and variations in each stage in the dust life cycle. Specifically, we individually vary, by an order of magnitude, the accretion rate ($\tau^{-1}_{\rm ref,g}$), SNe destruction efficiency ($\bar{\epsilon}$), and stellar dust production efficiencies ($\delta_i^{\rm AGB}$ and $\delta_i^{\rm SN}$), including switching efficiencies between the two implementations, and individually turning off each creation and destruction mechanism. We then compare each of these variations by analyzing their resulting steady-state galaxy-integrated D/Z, a commonly used '0$^{\rm th}$ order' metric for comparing dust evolution models. Of these variations, we found turning off thermal sputtering has negligible effects and changes to the stellar dust creation efficiencies only affect the initial build up of dust but has little effect on the steady-state D/Z with results for these shown in Appendix 2.C. However, variations to accretion and SNe destruction processes have noticeable effects on the resulting D/Z for both implementations. This reinforces the paradigm that stellar dust production provides the 'seeds' for dust growth, while the steady-state D/Z is determined by the balance between gas-dust accretion and SNe destruction (Draine, 1990) and suggests resolving the ISM phase structure, to accurately track gas-dust accretion, is crucial for dust studies.[13] Below we evaluate these variations for each implementation and show how they both can be predicted by analytic models.

Elemental

For the "Elemental" implementation noticeable changes were found when increasing accretion rates by a factor of 10 or enhancing the SNe dust destruction efficiency by a factor of 2 or more. The time evolution of the galaxy-integrated D/Z, dust creation source contribution, and dust species composition for these tests are shown in Fig. 2.3. In all cases accretion quickly takes over as the dominant source of dust mass, producing a steady-state D/Z and dust population. Since accretion occurs in all gas environments for this implementation, we can analytically predict the steady-state D/Z by determining the equilibrium between accretion and SNe destruction (e.g Mattsson & Andersen, 2012; Aniano et al., 2020). The fractional change in dust mass for a given element i in a gas cell, ignoring stellar dust creation, is then given by

$$\frac{\dot{M}_{i,\rm dust}}{M_{i,\rm dust}} = \frac{1-f_{\rm i}}{\tau_{\rm acc}} - \frac{1}{\tau_{\rm d}} \tag{2.19}$$

where $f_i = M_{i,\rm dust}/M_{i,\rm metal}$ is the degree of condensation of a given element i bound in dust, $\tau_{\rm acc}$ is the median accretion growth timescale, and $\tau_{\rm d} = \frac{M_{\rm ISM}\tau_{\rm SN}}{\bar{\epsilon} M_{\rm s}(1)} \sim 0.77$ Gyr is a characteristic dust

[13]Strictly speaking, the galaxy steady-state D/Z changes with times since gas-dust accretion scales with Z which increases with time. However, for MW-like galaxies with $Z \sim Z_{\odot}$ and steady star formation, the galactic metal enrichment timescale is significantly longer than the time it takes for the galactic dust population to reach a steady-state.

destruction timescale due to SNe taken from Eq. 18 in McKee (1989) where $M_{\rm ISM} = 6.5\times10^9 M_\odot$ is the gas mass of the ISM and $\tau_{\rm SN}^{-1} \sim \frac{1}{120\,{\rm yr}}$ is the galactic SNe rate in our simulation at its final time, and $\bar{\epsilon}M_{\rm s}(1)$ is the ISM mass wherein all dust is destroyed per SNe, on average given as $\sim 980\ M_\odot$ in Eq. 2.18. Putting these together, one obtains the very simple expectation $f_i \sim \max[(1 - \frac{\tau_{\rm acc}}{\tau_{\rm d}}), 0]$. Given $\tau_{\rm acc} = 330$ Myr from our simulations, the equilibrium degree of condensation is $f_i = 0.57$ for each refractory element i, which yields D/Z = 0.45 assuming solar metal abundances. Increasing the accretion rates by a factor of 10 or increasing the SNe dust destruction efficiency by a factor of 2 predict a steady-state D/Z = 0.75 and D/Z = 0.11 respectively, but only the former matches well with our resulting D/Z shown in Fig. 2.3. This discrepancy is most likely due to this model's assumption that all SNe destroy dust equally. Since we time-resolve SNe events, SNe that occur in the bubbles of previous SNe will destroy less dust causing the 'true' dust destruction timescale to be longer than $\tau_{\rm d}$ (Hu et al., 2019).

Species

For the "Species" implementation, we find noticeable changes if we remove the accretion temperature cutoff, or enhance the SNe dust destruction efficiency by a factor of 2 or more, or increase the accretion rate by a factor of 10. The time evolution of the galaxy-integrated D/Z, dust creation source contribution, and dust species composition for these tests are shown in Fig. 2.4. Similar to the "Elemental" implementation, accretion prevails as the dominant source of dust mass growth, producing a steady-state D/Z and dust population. Since accretion only occurs in relatively dense environments with T < 300 K for this implementation, we can analytically predict the steady-state D/Z ratio based on the average D/Z between gas inside and outside of cold neutral regions. To determine these values we need to determine the degree of condensation of the key element for dust species j inside and outside of cold gas/clouds ($f_{{\rm in},j}$ and $f_{{\rm out},j}$). To determine $f_{{\rm in},j}$ we use Eq. 45 in Zhukovska et al. (2008) which is a simple fit to the average degree of condensation of the key element, assuming it condenses in cold clouds which form and

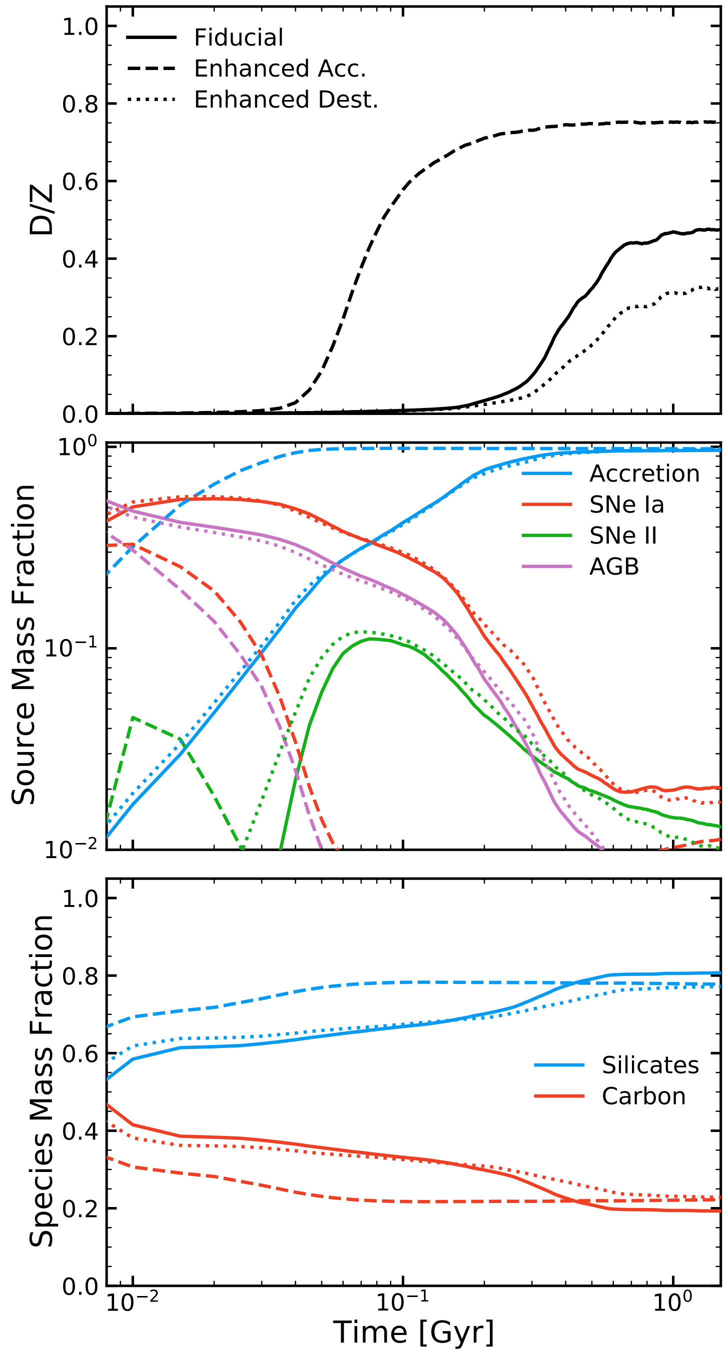

Figure 2.3. "Elemental" time evolution of galaxy-integrated D/Z ratio (*top*), fraction of total dust mass from each source (*middle*), and fraction of total dust mass composed of each dust species (*bottom*) for an idealized Milky Way-like galaxy. We ran the "Elemental" implementation with the fiducial model (*solid*), order of magnitude increased gas-phase accretion rates (*dashed*), and doubled SNe dust destruction efficiency (*dotted*). In all cases the dust population reaches a steady-state by simulation end, with accretion becoming the dominant source of dust mass. Note the fiducial model's accretion rate is 'tuned' to produce reasonable D/Z as noted in Sec. 2.3.5

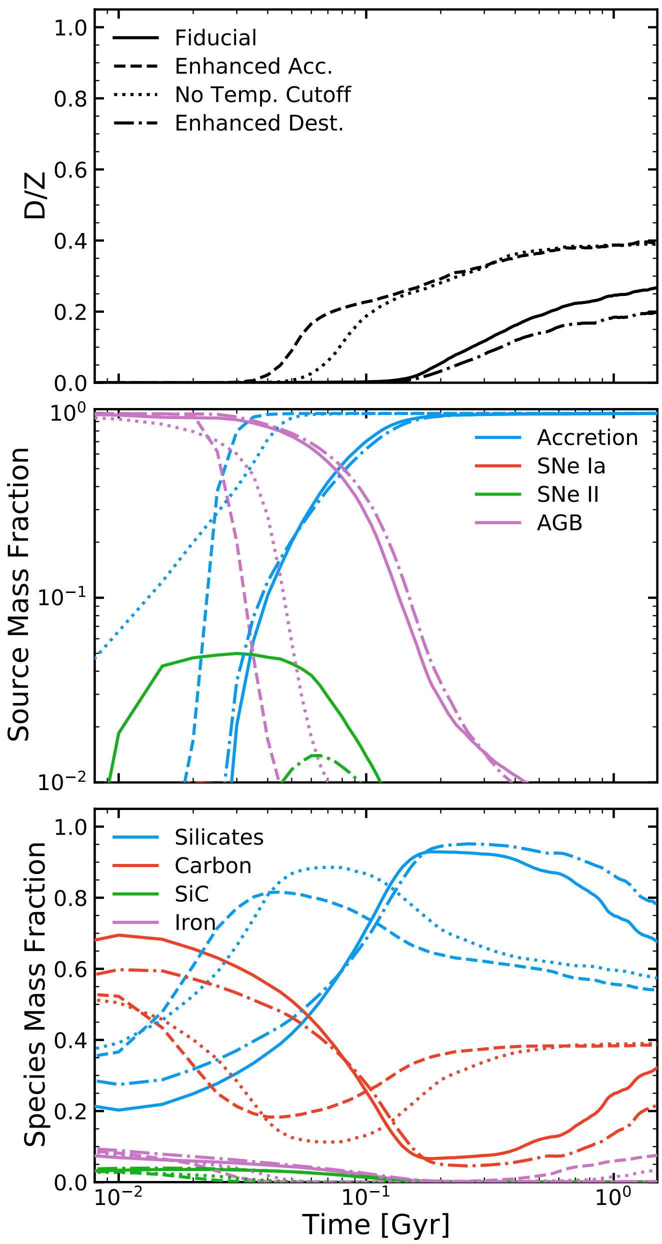

Figure 2.4. "Species" time evolution of galaxy-integrated D/Z ratio (*top*), fraction of total dust mass from each source (*middle*), and fraction of total dust mass composed of each dust species (*bottom*) for an idealized Milky Way-like galaxy. We ran the "Species" implementation with the fiducial model (*solid*), order of magnitude increased gas-phase accretion rates (*dashed*), no temperature restriction for gas-dust accretion (*dotted*), and doubled SNe dust destruction efficiency (*dash-dotted*). In all cases they reach a near steady-state D/Z by simulation end, with accretion becoming the dominant source of dust, but the composition of the dust population differs. This difference is mainly due to the amount of carbonaceous dust that can form before CO takes up any remaining gas-phase C in dense environments.

disperse over some timescale $\tau_{\rm cloud}$, maintaining a statistically steady-state abundance,

$$f_{{\rm in},j} = \left(\frac{1}{f_{{\rm o},j}^2 (1+\tau_{\rm cloud}/\tau_{{\rm g},j})^2} + 1 \right)^{-1/2} \tag{2.20}$$

where $\tau_{\rm cloud} \sim 10$ Myr is the typical mean cloud lifetime in similar simulations as estimated in Benincasa et al. (2020), $f_{{\rm o},j} = f_{{\rm out},j}$ is the average initial degree of condensation when the gas enters the cold cloud, and $\tau_{{\rm g},j}$ is the median effective accretion growth timescale for dust species j given the gas properties at simulation end. Specifically in our fiducial model implementation, we have approximately $\tau^{\rm eff}_{\rm g,sil} \sim 10$ Myr, $\tau^{\rm eff}_{\rm g,carbon} \sim 40$ Myr, and $\tau^{\rm eff}_{\rm g,iron} \sim 100$ Myr.

To determine the average degree of condensation outside of cold clouds we use

$$f_{{\rm out},j} = \left(1 - \frac{\tau_{\rm cycle}}{\tau_{\rm d}}\right) f_{{\rm in},j} \tag{2.21}$$

where $\tau_{\rm cycle} = \tau_{\rm cloud}\frac{1-X_{\rm cloud}}{X_{\rm cloud}}$ is the average time it takes to cycle all ISM material from the cold cloud phase through the diffuse/warm ISM phases and back into cold clouds required to give a steady-state fraction $X_{\rm cloud}$ of the mass of the ISM with T<300K (where we have $X_{\rm cloud} \sim 0.30$ at simulation end), and $\tau_{\rm d}$ is again the characteristic SNe dust destruction timescale defined above.

With Eq. 2.20 and 2.21 we find that the average mass weighted degree of condensation $f_{{\rm avg},j} = (1-X_{\rm cloud}) f_{{\rm out},j} + X_{\rm cloud} f_{{\rm in},j}$ which gives an average D/Z = 0.29 assuming solar metal abundances and silicate composition given in Sec. 2.3.3. Increasing the growth rate by a factor of 10 or increasing the SNe dust destruction efficiency by a factor of 2 yield a steady-state D/Z = 0.42 and D/Z = 0.27 respectively, all of which match well with our simulated D/Z. For removing the accretion temperature cutoff, we can simply approximate D/Z by Eq. 2.19 (but using the rates only for the key element of each dust species) giving D/Z = 0.44.

While this model produces lower steady-state D/Z compared to the "Elemental" model, it is more robust to changes in $\tau_{\rm g}$ and $\tau_{\rm d}$ because of the model's 'two-phase' scheme, with efficient growth within cold clouds and efficient destruction outside them. So even if dust accretion growth is infinitely efficient, D/Z will not increase more than X_{cloud} as long as destruction is efficient. On the other hand if dust destruction is infinitely efficient, D/Z cannot decrease below X_{cloud} if growth there is still efficient.

As shown, both models can produce galaxy-integrated D/Z values near the canonical MW D/Z ~ 0.4, depending primarily on the gas-dust accretion and SNe dust destruction timescales. However, both dust evolution models depend directly on the local gas environment, which can produce large D/Z variations within a galaxy compared to the galaxy-integrated value. A better gauge we can use to further analyze and test these implementations is the resulting relationship between D/Z and local gas properties compared with observations.

2.4.2 Element Depletions and D/Z

Sight Line Element Depletions

Element depletions are a commonly used method for estimating interstellar dust abundances. The gas-phase abundance of refractory elements are compared to an assumed reference abundance, with any elements missing from the gas-phase assumed to be locked in dust. The gas-phase depletion of element X assuming solar reference abundances, $(N_{\mathrm{X}}/N_{\mathrm{H}})_{\odot}$, is usually represented logarithmically as

$$\left[\frac{\mathrm{X}}{\mathrm{H}}\right]_{\mathrm{gas}} = \log\left(\frac{N_{\mathrm{X}}}{N_{\mathrm{H}}}\right)_{\mathrm{gas}} - \log\left(\frac{N_{\mathrm{X}}}{N_{\mathrm{H}}}\right)_{\odot}. \tag{2.22}$$

where N_{X} and N_{H} are the gas-phase column density of element X and column density of neutral hydrogen ($N_{\mathrm{H,neutral}} = N_{\mathrm{H\,I}} + 2N_{\mathrm{H_2}}$) respectively. Similarly, the linear depletion of element X is

$$\delta_{\mathrm{X}} = 10^{[\mathrm{X/H}]_{\mathrm{gas}}}. \tag{2.23}$$

Observationally, measuring individual element depletions necessitates obtaining high-resolution UV spectroscopy with a high signal-to-noise ratio (S/N), and so detailed observations are mainly limited to the Milky Way. Also since depletions require observing spectral absorption features they mainly sample dust in low density environments. The most comprehensive review of Milky Way element depletions was compiled by Jenkins (2009), including over 243 lines of sight probing a wide range of physical conditions. To compare directly to these observations, we created a set of 10,000 sight lines for each simulation, deriving $N_{\rm X}$ and $N_{\rm H,neutral}$ from the total element abundances, amount of each element in dust, and neutral H number densities for gas cells intersected along each line of sight assuming these properties are uniform within each cell. Similar to the sight lines compiled in Jenkins, each simulated sight line ends at the solar galactic radius ($r \sim 8$ kpc) with a sight line distance chosen from a uniform distribution of 0.2 to 2 kpc. For simplicity each sight line was orientated parallel with the galactic disk in a random direction[14]. We binned these sight lines in logarithmic neutral H column density bins and calculated the median and 16-/84-percentile for C[15], O, Mg, Si, and Fe depletions. Note we use the local element abundances tracked in our simulation along each sight line when calculating depletions instead of assuming solar element abundances as is done with observations. The resulting relation between sight line element depletion and $N_{\rm H,neutral}$ for each element can be seen in Fig. 2.5 resulting from the fiducial "Elemental" model, the fiducial "Species" model along with optional O-reservoir and Nano-iron dust species included. We also include the observed sight line depletions from Jenkins (2009).

Special attention is given when comparing to C depletions from Jenkins (2009)[16] due to the scarcity of data and apparent excess of gas-phase C compared to the amount needed to be locked up in carbonaceous dust. Sofia et al. (2011); Parvathi et al. (2012) suggest that these gas-phase C values are too high by a factor of ~2 when comparing C abundances determined from strong and weak C II transition lines. For this reason we decrease all sight line C depletions

[14]We leave further investigation of the sensitivity of these sight line results to free parameters (e.g. sight line inclination with disk, choice of sight line start points, gas mass resolution, etc.) to fully cosmological simulations.

[15]We include C in CO in our measured gas-phase C as is done with observations.

[16]Jenkins' definition of $[{\rm C/H}]_{\rm gas}$ does not explicitly include C in CO but it is assumed there is only a negligible amount of CO in the environments observed.

from Jenkins (2009) by a factor of 2. We also include observations from Parvathi et al. (2012)[17] of carbon depletion and $N_{\mathrm{H,neutral}}$ along 21 sight lines in the Milky Way. Note that since a handful of these sight lines have C abundances greater than the reference Lodders (2003) solar abundances (C/H = 288 ± 26 ppm) used in Jenkins', we take the maximum abundance from this data set (C/H = 464 ± 57 ppm) as the reference abundance. This reduces the resulting depletion values by a factor of ~40%.

Local Gas Element Depletions

Individual sight lines probe various gas phases and sight lines with similar $N_{\mathrm{H,neutral}}$ but different lengths can probe vastly different gas environments. This makes sight line observations less suited for constraining our dust evolution models since they depend on local gas environments. Since the total element abundances and the amount of each element in dust are tracked for all gas cells in our simulations, we can also directly measure the depletion for each element as a function of physical gas density. This means Eq. 2.22 becomes

$$\left[\frac{\mathrm{X}}{\mathrm{H}}\right]_{\mathrm{gas}} = \log\left(\frac{n_{\mathrm{X}}}{n_{\mathrm{H}}}\right)_{\mathrm{gas}} - \log\left(\frac{n_{\mathrm{X}}}{n_{\mathrm{H}}}\right)_{\odot}, \tag{2.24}$$

where n_{X} and n_{H} are the local, gas-phase number density of element X and neutral H ($n_{\mathrm{H,neutral}} = n_{\mathrm{H}} + 2n_{\mathrm{H_2}}$) respectively and $(n_{\mathrm{X}}/n_{\mathrm{H}})_{\odot}$ is the total abundance (gas+dust) of element X in the gas cell. To do this we bin the gas cells in logarithmic neutral gas density and calculate the median values and 16-/84-percentiles for C, O, Mg, Si, and Fe depletions. The resulting relation between element depletion and neutral gas density, $n_{\mathrm{H,neutral}}$, for each element can be seen in Fig. 2.6 resulting from the fiducial "Elemental" model, and fiducial "Species" model along with optional O-reservoir and Nano-iron dust species included.

Comparing to observations, Jenkins (2009) derived an empirical fit between element depletions and the average neutral gas density along lines of sight $\langle n_{\mathrm{H}}\rangle^{\mathrm{min}}_{\mathrm{neutral}} = N_{\mathrm{H,neutral}}/d$, where

[17] Parvathi specifically includes CO in their calculations of $[\mathrm{C/H}]_{\mathrm{gas}}$ but CO takes up < 1% of gas phase C for most sight lines.

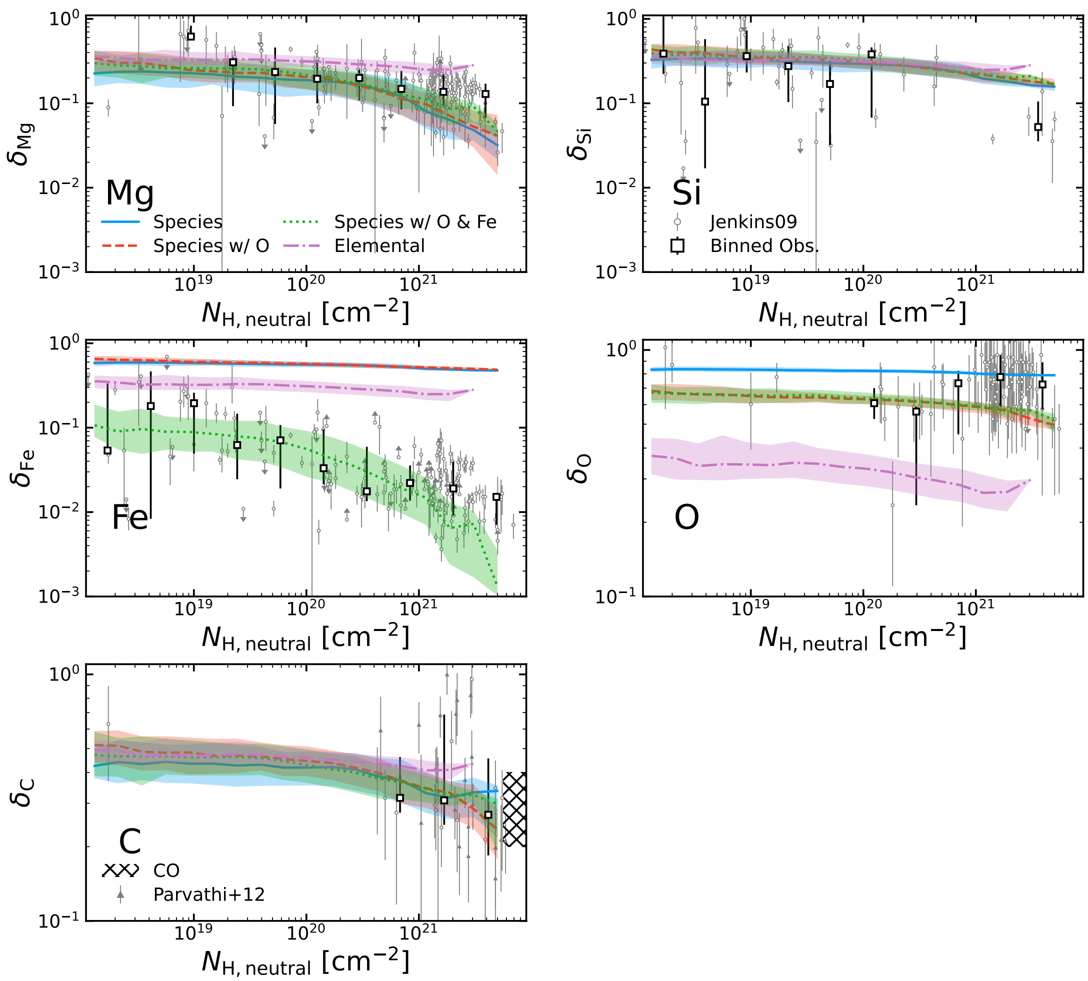

Figure 2.5. Predicted sight line C, O, Mg, Si, and Fe depletion versus $N_{\mathrm{H,neutral}}$ from 10,000 sight lines at the solar galactic radius in an idealized Milky Way-like galaxy for our fiducial “Species” model, “Species” with O-reservoir dust species, “Species” with O-reservoir and Nano-iron dust species, and the fiducial “Elemental” model. For each, 16-/84-percentile ranges are represented by shaded regions. We compare with observed elemental depletion along sight lines in the Milky Way from Jenkins (2009) (*circles*). For C we decreased the Jenkins data by a factor of 2 based on observations from Sofia et al. (2011) and Parvathi et al. (2012). We also include 21 sight line observations from Parvathi et al. (2012) (*triangles*) along with a range of expected minimum depletions in dense environments (*hatched*) based on observations of 20% to 40% of C in CO. We also show the binned median and 16-/84-percentile ranges for the Jenkins and Parvathi data (*squares*). The “Elemental” model produces a relatively flat depletion relation that is near identical for all elements and under-depletes Mg, Si, and Fe while it over-depletes O at high $N_{\mathrm{H,neutral}}$. The “Species” model produces a more complex relation, transitioning from a shallow to steep slope for increasing $N_{\mathrm{H,neutral}}$, which matches well with observations. Si is the only element that does not show this transition, but this is due to the metal yield prescription in FIRE-2 as shown in Appendix 2.E. For "Species" model, the inclusion of O-reservoir and Nano-iron dust is needed to match the observed depletions of O and Fe.

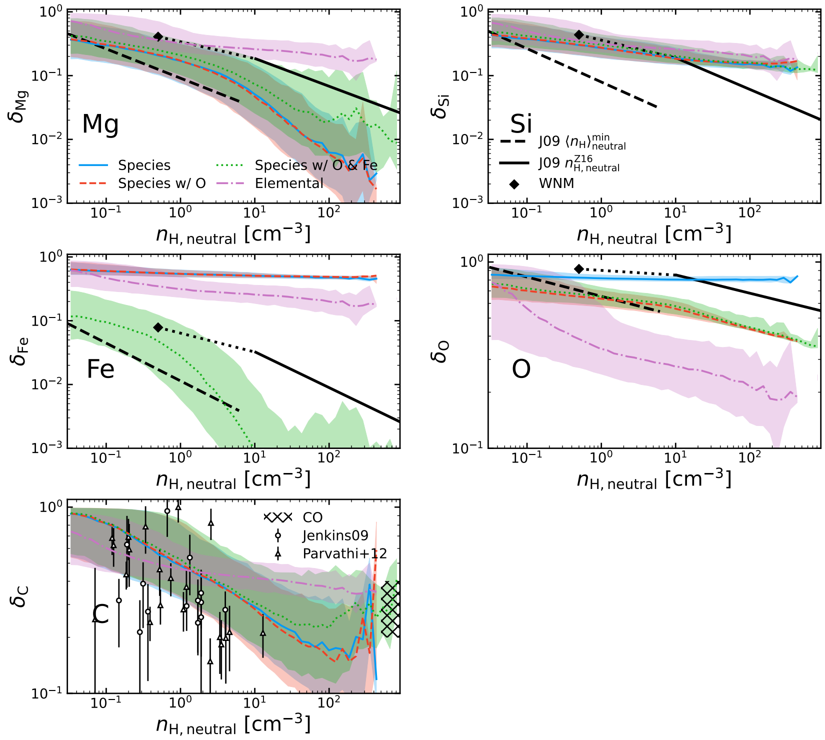

Figure 2.6. Predicted C, O, Mg, Si, and Fe depletion versus $n_{\mathrm{H,neutral}}$ in an idealized Milky Way-like galaxy for our fiducial "Species" model, "Species" with O-reservoir dust species, "Species" with O-reservoir and Nano-iron dust species, and the fiducial "Elemental" implementation. For each, 16-/84-percentile ranges are represented by shaded regions. We compare with observed elemental depletions in the Milky Way from Jenkins (2009) assuming mean sight line density is the physical density (*black-dashed*), this can be treated as a lower limit, and using Zhukovska et al. (2016, 2018) mean sight line density to physical density fit (*black-solid*). For O, Mg, Si, and Fe we include estimates for the WNM depletions (*diamond*) along with an interpolation to the Jenkins' relation (*black-dotted*). For C we only include the individual sight line depletions from Jenkins (*triangles*) decreased by a factor of 2 based on observations from Sofia et al. (2011) and Parvathi et al. (2012). We also include 21 sight line observations from Parvathi et al. (2012) (*circles*) as another lower bound along with a range of expected minimum depletions in dense environments (*hatched*) based on observations of 20% to 40% of C in CO. The "Elemental" model produces a relatively shallow sloped depletion relation that is near identical for all elements and either under-depletes Mg, Si, and Fe or over-depletes O at high $n_{\mathrm{H,neutral}}$. The "Species" model produces a relation which transitions from a shallow to steep slope for increasing $n_{\mathrm{H,neutral}}$ matching well with observations. Si is the only element which does not show this transition, but this is due to the metal yield prescription in FIRE-2. Updated yields in the next version of FIRE (Hopkins et al., 2023)) produce much better agreement with observations as shown in Appendix 2.E. For this model, the inclusion of the O-reservoir and Nano-iron dust species are also needed to match the observed strong depletions for both O and Fe respectively. For both models, our sub-resolved CO prescription produces a flattening of the C depletion relation in the densest environments due to gas-phase C becoming locked in CO and halting carbonaceous dust growth.

d is the distance to the background UV source viewed in absorption.[18] We include these volume- and sight line-averaged relations between element depletions and $\langle n_{\rm H} \rangle^{\rm min}_{\rm neutral}$ in Fig. 2.6.

Note for C, due to the paucity of observed data and resulting poor fit in Jenkins we opt to only show the individual sight lines from Jenkins (2009) and Parvathi et al. (2012) and not the fitted relation[19]. Allowing for any realistic degree of inhomogeneity in the ISM, $\langle n_{\rm H} \rangle^{\rm min}_{\rm neutral}$ will always be significantly lower than the true physical density of the cold gas in which a majority of the dust and neutral column density along a line of sight resides. Therefore, this should be considered a lower bound for the "true" $n_{\rm H,neutral}$ of interest in the simulations.

To compare to a reasonable estimation of element depletions in dense environments we also compare the estimated relation between $[{\rm Si/H}]_{\rm gas}$ and $n_{\rm H,neutral}$ from Zhukovska et al. (2016), who used fine-structure excitations of neutral carbon from Jenkins & Tripp (2011) measured for a subset of the sight lines from Jenkins (2009) to try to infer a better estimate of the true $n_{\rm H,neutral}$ for the same sight lines. This effectively gives the following relationship between $\langle n_{\rm H} \rangle^{\rm min}_{\rm neutral}$ and $n^{\rm Z16}_{\rm H,neutral}$ of $n^{\rm Z16}_{\rm H,neutral} = 147.2 \left(\frac{\langle n_{\rm H} \rangle^{\rm min}_{\rm neutral}}{1 \ {\rm cm}^{-3}} \right)^{1.05} \ {\rm cm}^{-3}$, which is restricted to $n^{\rm Z16}_{\rm H,neutral} = 10 - 10^3 \ {\rm cm}^{-3}$ since the method used is biased to denser gas. We further modify this by reducing the depletions for Mg, Si, and Fe by 0.2 dex as recommended by Zhukovska et al. (2018) to account for the increase in depletion due to contamination by the warm neutral medium (WNM) along sight lines, since only the high density gas is probed by C I which will have lower depletions than the contaminating WNM. We do not account for this for O and C since their depletion slopes are quite shallow compared to the other elements and so the WNM contamination should have a comparatively small effect.

To gain a general constraint on element depletions in low density environments we included the depletions for O, Mg, Si, and Fe at $F_* = 0.12$ from Jenkins (2009) which they

[18] For clarity, Jenkins does not derive a direct fit for each element depletion but instead for the F_* parameter which represents the total strength of all element depletions along a line of sight ($F_* = 0$ is the least depleted and $F_* = 1$ is the depletions for ζ Oph, one of the most depleted sight lines in their sample). This fit also only includes sight lines with $\log[N_{\rm H,neutral}] > 19.5$ to avoid contamination from ionized H.

[19] Note, we do use the fitted relation for C depletion when aggregating element depletions to determine the expected D/Z.

recommend for the WNM based on matching depletion values with those given in Savage & Sembach (1996) for the WNM in the Galactic disk. In Fig. 2.6 we place this depletion at the typical density of the WNM, $n_{\mathrm{H}} \sim 0.5$ cm^{-3}. We exclude this for C due to the reasons mentioned above.

Since the total dust population is an aggregate of all element depletions, we also investigate the resulting distribution of D/Z with neutral gas density for the same models. The median D/Z and 16-/84-percentile are shown in Fig. 2.7. Aggregating the observed element depletions, we include an upper bound on the expected D/Z along with an estimate for the WNM[20] based on depletions from Jenkins (2009) along with a reasonable estimate of D/Z in dense environments following the aforementioned relation from Zhukovska et al. (2016, 2018).

We will remark here that the large scatter in the simulated depletion values and consequently D/Z arises from the diverse histories of gas with the same density, particularly depending on what stage the gas is in the molecular cloud life cycle. If the gas is being ejected from the molecular cloud phase and on its way to the WNM phase, it will have higher depletions than gas that has resided in the WNM for an extended period, being subject to various destruction processes. Similarly, gas that quickly collapses into the molecular cloud phase or spends a relatively long amount of time in the WNM phase will have lower depletions than gas that takes a long time to collapse or resides in the WNM phase for a short period of time.

Elemental

Since this implementation uses the same gas-dust accretion timescales for all elements, any differences between element depletions due to the initial dust population vanish in the long term, producing identical depletion relations with column $N_{\mathrm{H,neutral}}$ and physical $n_{\mathrm{H,neutral}}$ for each element. This inherently cannot match observed depletions as shown in Fig. 2.5 & 2.6, which clearly vary element by element. C is the only element that deviates in this model, due to our accounting of C trapped in CO which produces a ≤ 0.15 increase in the depletion at any

[20]To account for the uncertainty in the observed WNM D/Z owing to the lack of measured sight line C depletions in this regime we include error bars representing 80% (assuming 20% in CO) of C or no C in dust.

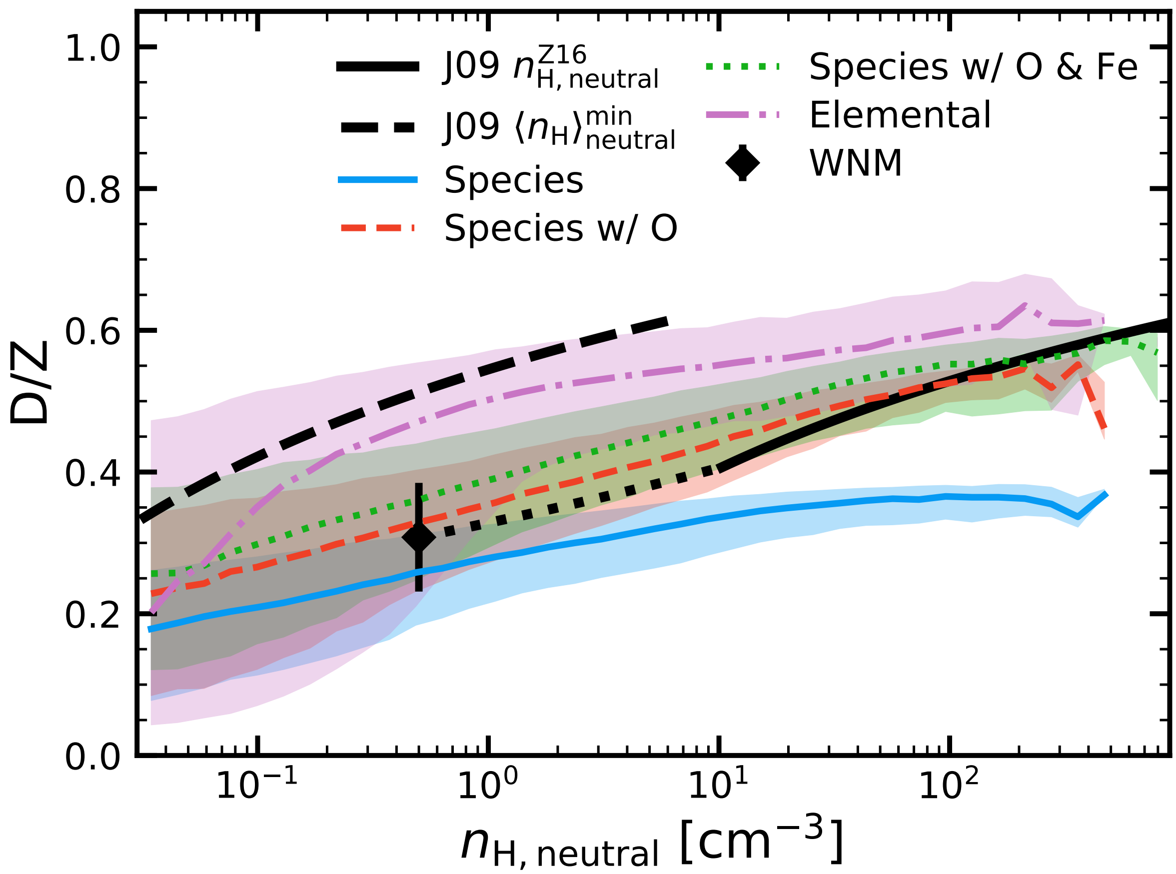

Figure 2.7. Relation between D/Z ratio and $n_{\rm H,neutral}$ in an idealized Milky Way-like galaxy for "Species" and "Elemental" implementations, with 16-/84-percentiles represented by shaded regions. We compare with observed D/Z values derived from observed elemental depletions (summing depletions from Fig. 2.6) in the Milky Way from Jenkins (2009) and assuming mean sight line density is the physical density (*black-dashed*), which can be treated as an upper limit, and using Zhukovska et al. (2016, 2018) mean sight line density to physical density fit (*black-solid*). We also include an estimate of the expected D/Z in the WNM (*diamond*) with error bars assume 0-80% of C locked up in dust along with an interpolation to the Jenkins (2009) fit (*black-dotted*). The "Elemental" model produces a shallow sloped D/Z relation across the observed range which over-predicts the amount of dust in low-density environments. The "Species" model produces a more strongly sloped relation, but the fiducial model does not produce the high D/Z values observed in dense environments. The addition of the O-reservoir dust species largely fixes this issue and steepens the D/Z slope. On the other hand, the inclusion of the Nano-iron dust species only produces a small increase in the overall D/Z relation.

given column or physical density. Ultimately this model can only match depletion observations for one element at a time, while heavily over- or under-depleting the rest of the elements. This is especially problematic for O since it makes up a large fraction of the ISM metal mass. The resulting relation also has a relatively shallow slope across the observable range, with depletions increasing by ~0.1 or ~0.2 from the WNM to the dense molecular regime for the column and physical density respectively, compared to the steeper relations observed in the MW for Mg, Si, and Fe. This shallow relation arises predominantly from the lack of a temperature restriction on dust growth and subordinately on the identical gas-dust accretion treatment for each element and generalized dust chemical composition. Dust residing in diffuse, warm gas for significant amounts of time grows appreciably, replacing dust destroyed by SNe remnants and thermal sputtering and leading to relatively small changes in element depletions for all but the most diffuse gas.

In regards to the total dust population, this produces reasonable D/Z values at high densities but the slope of the relation is again relatively shallow as seen in Fig. 2.7. While this does produce a range of D/Z values in the WNM regime which overlap with observations, the typical D/Z is still well above this.

Species

Since many details and optional dust physics modules for this implementation are motivated by observed depletions of individual elements, we review each element depletion relation with column $N_{\mathrm{H,neutral}}$ and physical $n_{\mathrm{H,neutral}}$ as shown in Fig. 2.5 & 2.6 in detail below. A brief overview of which dust physics modules for this implementation affect individual element depletions and/or overall D/Z is provided in Table 2.3.

Magnesium and Silicon: Mg and Si are expected to have nearly identical depletion relations and almost entirely reside in silicate dust grains, so we will examine both elements together. Focusing at first on Mg, our fiducial model is able to reasonably match observed depletion trends with respect to both H column density and local gas density, with the predictions transitioning from a shallow to steep slope with increasing density. This change in slope arises from the transition between the diffuse medium where dust is destroyed by SNe and thermal sputtering to dense neutral gas where the dust rapidly grows via gas-dust accretion. On the other hand, our model does not produce a similar change in slope for Si depletion, instead exhibiting a constant shallow slope (shallower than inferred from observations). This result stems not from a failing of our dust model per se, but from the metal yield prescription in FIRE-2. The IMF-integrated SNe yields in FIRE-2 produce more Si than Mg, leading to a galaxy wide overabundance of Si compared to Mg after ~100 Myr into our simulations. This, in turn, leads to Mg being the key element for silicate dust growth. The next version of the FIRE model (Hopkins et al., 2023) uses an updated set of metal yields which predict modestly higher Mg production. This has the effect of making Si the key element, and, as we show in Appendix 2.E, producing much better agreement with observations.

The inclusion of either the O-reservoir and/or Nano-iron dust species has only modest effects on the resulting Mg and Si depletion relations. It should again be noted that the Nano-iron module assumes the metallic iron nanoparticle inclusions in silicate dust provide the needed Fe for the silicate chemical structure instead of atomic, gas-phase Fe. Without this assumption, Fe becomes the key element for silicate dust growth and the resulting Mg and Si depletions end up far too low compared to observations.

Oxygen: Our fiducial model demonstrates that, as expected, pure silicate dust alone cannot reproduce the large dispersion in observed O depletions in dense environments, sequestering ~20% of available O and producing a relatively flat depletion relation with almost no scatter. Adding an O-reservoir dust species partly rectifies this issue, producing a similar change in slope to Mg and Si and a larger scatter, which produce a better match to both H column density and local gas density observations. While the O-reservoir species parameters are implicitly designed to match observed depletions at high densities, the shallow slope in diffuse environments arises purely from gas cycling out of neutral gas and being exposed to SNe dust destruction and thermal sputtering.

Iron: It is already known that purely silicate dust alone cannot reproduce the extreme depletions of gas-phase iron. Adding the Normal-iron species, as used in our fiducial model, does not fix this issue. Such metallic iron dust grows too slowly, even with accounting for Coulomb enhancement in our model. The addition of the Nano-iron dust species produces a depletion relation more in line with observations, with a similar transition from a shallow to steep slope as Mg and Si but with a far steeper slope in dense environments with both high H column density and local gas density. The combination of small grain sizes and Coulomb enhancement gives this metallic iron species an extremely short accretion timescale depleting nearly all gas-phase Fe in dense environments. The Coulomb enhancement term being especially important, as shown in Appendix 2.D. In combination, the reduced destruction efficiency of these grains due to them being modeled as shielded inclusions allows for the still relatively high depletions in the low density regime, compared to other elements.

Carbon: Of the elements we track in dust, carbon is the least constrained by observations, with only a handful of sight line depletion observations over a narrow range of $N_{\rm H}$ and observed fractions of C in CO (~20%−40%) providing a constraint in dense molecular environments[21]. Moreover, our treatment of carbonaceous dust is quite restrictive compared to silicate, with growth via accretion only occurring in CNM and diffuse molecular environments before the gas transitions to the dense molecular phase, where we assume CO takes up any remaining gas-phase C, halting carbon dust growth. Even with these constraints, our predicted C depletions fall well within observational bounds, producing a steep slope between the WNM and CNM phases ($0.1\ {\rm cm}^{-3} < n_{\rm H,neutral} < 50\ {\rm cm}^{-3}$), which in turn yields a steep slope for $N_{\rm H,neutral} > 2\times10^{20}\ {\rm cm}^{-2}$, while still leaving enough gas-phase C at high densities to match observed CO abundances. The scatter in C depletions at high density also matches surprisingly well with the range of observed values for C in CO. This dispersion arises from the variable history of individual gas parcels in the simulation, with gas that quickly transitions to the dense molecular phase forming less

[21] In diffuse and dense neutral gas regime CO is directly observed via absorption or emission features (e.g Sheffer et al., 2008). These CO observations give a lower limit to the gas-phase C abundance.

dust and allowing a larger amount of C to be locked in CO, while gas which slowly transitions forms more dust and leaves less gas-phase C to form CO. This suggests that the large range in observed C in CO fractions (20%-40%) can be attributed to the history of the gas in question. We also tested our "Species" model without any accounting for CO, allowing carbonaceous dust to grow in dense molecular gas akin to the other (non-C) dust species above, but the resulting C depletions are too low, leaving far too little gas-phase C in dense environments compared to observations of CO as shown in Appendix 2.D. This highlights the need for an accounting of C in CO to accurately model the evolution of carbonaceous dust. Our results also suggest very little carbonaceous dust should exist at low local gas densities ($n_{\rm H,neutral} < 0.1$ cm^{-3}) compared to silicate dust, although this prediction is sensitive to our assumptions about dust sizes and destruction in SNe. This could have considerable effects on the effective attenuation law in such environments. However, these results may be due to this being an idealized galaxy without a realistic corona/disc-halo interface, or due to the details of cooling/heating and neutral gas physics used in FIRE-2 (Appendix 2.E). Investigation with fully cosmological simulations will be needed to explore this further.

D/Z: Our fiducial model produces too little dust in dense environments, per Fig. 2.7, leading to the low galaxy-integrated D/Z shown in Sec. 2.4.1. This failing is a direct result of our adopted dust composition constraints, specifically of O. When we include the O-reservoir dust species this issue is largely resolved, with the D/Z slope steepening for $n_{\rm H,neutral} > 1$ cm^{-3}, in plausible consistency with observations and increasing the galaxy-integrated value to D/Z ~ 0.34. Adding the Nano-iron dust species produces an overall shift in D/Z of ≤ 0.04 but does not change the shape of the relation, suggesting that tracking a separate metallic iron dust species is not essential when modeling steady-state dust populations. In any case, all versions of this implementation produce a non-negligible median D/Z ≥ 0.2 even in the most diffuse gas. This suggests a sizeable fraction of metals are trapped in dust no matter the gas phase, but again this may be a consequence of this being an idealized galaxy or due to details of the gas phase structure.

Table 2.3. Table summarizing whether or not a given piece of our assumed dust physics strongly influences either the D/Z ratio or element-by-element depletion trends.

	D/Z	Element Depletion
O-reservoir	Yes	Yes
Nano-iron	No	Yes
C in CO	No	Yes
Coulomb Enh.	Yes	Yes

In summary, the "Elemental" implementation's near identical treatment of all refractory elements in dust prevents it from matching observed variable element depletions and its allowance for unrestricted gas-dust accretion produces relatively flat element depletions and D/Z across the observed range of H column and local gas densities. Conversely, the "Species" implementation's accounting for dust chemical composition is able to match observed element depletion, but the inclusion of some additional theoretical O-reservoir and Nano-iron dust species are needed to match O and Fe depletions respectively. In addition, the T<300K restriction on gas-dust accretion along with Coulomb enhancement produces a steep slope in element depletion and D/Z relations with both H column density and local gas density.

2.4.3 Spatially Resolved D/Z Beyond the MW

Looking to extragalactic observations of dust, direct measurements of element depletions are very challenging with current instruments (i.e. key refractory elements, notably carbon, are not observable via absorption outside the MW; Roman-Duval et al. 2019a,b; Péroux & Howk 2020). An alternative, albeit somewhat model-dependant, method for estimating D/Z is to combine separate, multi-wavelength estimates of dust mass, gas mass, and metallicity. This method relies on matching dust emission spectra to infer a dust mass and so mainly probes denser environments compared to depletion-based observations, and does build in some implicit dependence on assumed dust chemistry and size distributions. While this method has yielded a plethora of galaxy-integrated studies of D/Z (e.g. Rémy-Ruyer et al., 2014; De Vis et al., 2019), these observations are less suited for constraining our dust evolution models since our models depend on the local gas environments within the galaxy and we only simulate one Milky Way-like galaxy. A more useful constraint for our purposes here is spatially resolved D/Z studies of individual galaxies, but few of these studies exist with only the Magellanic Clouds (Jenkins & Wallerstein, 2017; Roman-Duval et al., 2014, 2017) and M31 (Draine et al., 2014) being mapped until recently. Recent work by Chiang et al. (2021) investigated the spatially resolved D/Z-environment relations (using the technique above) for five nearby galaxies: IC 342, M31, M33, M101, and NGC 628. We compare our simulations with these observations in Fig. 2.8 examining the relation between D/Z, neutral gas surface density ($\Sigma_{\rm gas,neutral}$), and galactocentric radius. We specifically show their derived D/Z values using the Bolatto et al. (2013) $\alpha_{\rm CO}$ prescription ($\alpha_{\rm CO}^{\rm B13}$), which Chiang et al. (2021) argued yields the most reasonable D/Z. To match the observational resolution we bin the simulation gas in 2 kpc face-on square pixels and calculate D/Z = $\Sigma_{\rm dust}/\Sigma_{\rm metals}$ for each pixel. We then group these pixels across $\Sigma_{\rm gas,neutral}$ and galactocentric radius and calculate the median D/Z values and 16-/84-percentiles for each.

Both the fiducial "Elemental" implementation and "Species" implementation with included O-reservoir and Nano-iron dust species are consistent with observations, falling near the middle and lower end of the observed range respectively for D/Z relative to both $\Sigma_{\rm gas,neutral}$ and galactocentric radius. On the other hand, the fiducial "Species" implementation produces too low D/Z in all gas environments, again emphasizing the importance of an additional O depletor beyond purely silicate dust. Chiang et al. (2021) also points out that there is an offset between emission based and depletion based observations, with emission producing higher D/Z across all gas metallicities they observe. This offset is either due to them probing different gas phases (HI- vs H_2-dominated), or due to any of the many systematic uncertainties in both methods, most notably the assumed dust population/emissivity model (Chastenet et al., 2021). Further study utilizing fully cosmological simulations with a sample of different galaxies is needed to better compare both our models with these observations due to the variable properties and histories of these galaxies.

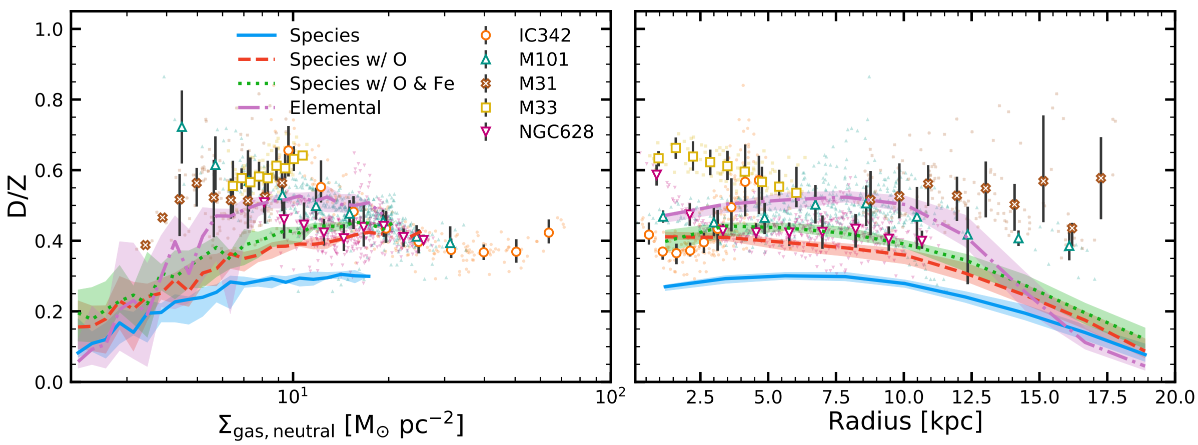

Figure 2.8. Relation between median D/Z ratio and neutral gas surface density (*left*) and galactocentric radius (*right*) in 2 kpc bins at simulation end for the "Elemental" and "Species" implementations with 16-/84-percentiles represented by the shaded regions. We compare with dust emission based observations of spatially-resolved D/Z for a few local galaxies (IC 342, M101, M31, M33, and NGC 628) from Chiang et al. (2021) with 2 kpc resolution and $\alpha_{\mathrm{CO}}^{\mathrm{B13}}$ conversion factor. We also show each observed galaxy's binned median and 16-/84-percentile ranges for D/Z with respect to each given property. We emphasize that the observed galaxies' physical sizes and metallicities do not closely correspond to our idealized galaxy and so this comparison is only an illustration of these dependencies and should not be used for strong quantitative comparison without proper matching of galactic properties which we will do with fully cosmological simulations in future work.

2.5 Conclusions

In this work we implemented two separate dust evolution models, labeled "Elemental" and "Species", into the GIZMO code base and coupled them with FIRE-2 stellar feedback and ISM physics. Both models account for dust creation in stellar outflows, dust growth from gas-phase accretion, dust destruction from SNe shocks, thermal sputtering, and astration, and turbulent dust diffusion in gas. The "Elemental" model tracks the dust yields of individual elements incorporated into carbonaceous and generalized silicate dust which are treated near identically in all physical processes and utilizes a 'tunable' dust growth routine. The "Species" model tracks the yields of specific dust species (silicates, carbon, silicon carbide, and iron), treating each uniquely depending on their chemical composition, along with optional nano-particle metallic iron (Nano-iron) dust species and an unknown oxygen based (O-reservoir) dust species, and incorporates a physically motivated dust growth routine. We also devised and integrated a sub-resolution dense molecular gas scheme with both models to account for different efficiencies of Coulomb enhancement for gas-dust accretion (in the "Species" model) and the reduction in carbon dust accretion due to the lock-up of gas-phase C into CO in dense molecular gas (Appendix 2.B).

Using both dust models, we ran idealized non-cosmological simulations of a Milky Way-mass galaxy to test their sensitivity to free parameters and compare to observations of D/Z and elemental depletions. We summarize our findings below:

1. Both implementations reaffirm that the steady-state galaxy-integrated D/Z ratio depends on the balance between gas-phase accretion and dust destruction by SNe, with the efficiency of initial stellar dust production having little effect as long as some "seeds" exist so that accretion can take over as the dominant dust source (Appendix 2.C). The fiducial "Species" implementation is able to produce a reasonable, but slightly low, D/Z $\sim$ 0.27 (Fig. 2.4), which increases to D/Z $\sim$ 0.34 or D/Z $\sim$ 0.38 with the inclusion of either the O-reservoir dust species or both the O-reservoir and Nano-iron dust species respectively (Fig. 2.7). The

fiducial "Elemental" model produces a reasonable D/Z ~ 0.47 (Fig. 2.3), but this requires manually "tuning" the gas-phase accretion rate for our simulation. While both models can produce, or be 'tuned' to produce, reasonable galaxy-integrated D/Z ratios, the predicted relations between element depletions and local gas properties vary dramatically.

2. The "Elemental" implementation is inherently unable to reproduce the variation in observed MW element depletions (Fig. 2.5 & 2.6), owing to its uniform treatment of accretion for each element in dust. This is especially problematic for O, which makes up a large portion of the metal mass. Furthermore, since there are no restrictions on gas-dust accretion for this implementation, dust that resides in hot gas for long periods can grow faster than it is destroyed by SNR or thermal sputtering, thus producing a relatively flat D/Z-$n_{\rm H,neutral}$ relation in all but the most diffuse gas (Fig. 2.7).

3. The fiducial "Species" model is only able to match observed Mg, Si, and C depletions in the Milky Way using our default standard model for silicates and carbonaceous grains with fixed chemical compositions. The inclusions of some additional theoretical O-reservoir and Nano-iron dust species are needed to match observed O and Fe depletions respectively for the model variations we study (Fig. 2.5 & 2.6). This additional O depletion is also critical to match observed D/Z ratios in the Milky Way, with the resulting D/Z-$n_{\rm H,neutral}$ relation being consistent with observations (Fig. 2.7). In this model, a temperature restriction on gas-dust accretion produces low D/Z ratios in diffuse environments, while high gas-phase accretion rates in the cold ISM (in conjunction with Coulomb enhancement; Appendix 2.D) yield large D/Z ratios in dense environments.

4. Extragalactic observations of spatially-resolved D/Z are, at present, roughly consistent with both models, provided these models also reproduce the MW D/Z (Fig. 2.8).

5. An accounting of C locked in CO ($f_{\rm CO}$; Appendix 2.B) can have important effects on depletion patterns, especially for C (Appendix 2.D).

Our results show that while a simplistic one-phase "dust by element" evolution model can produce reasonable galaxy-integrated dust properties, a more complex, chemically motivated two-phase "dust by species" evolution model is needed to reproduce observed spatial dust variability, in both amount and composition, within a galaxy. In a companion paper, we will further investigate and compare both models in a fully cosmological context for a wide range of galaxy halo masses to study the relation between dust and various galactic properties and the effects of integrating 'live' dust evolution with radiative transfer/feedback and cooling and heating ISM physics on galaxy evolution (as opposed to assuming a constant D/Z). These studies will provide further tests for the current dust population and chemical composition paradigm.

We stress that our dust models are in no way "complete" and, beyond the major uncertainties we detail, our models lack important dust physics which could have drastic effects on our results. First and foremost we do not track the evolution of the dust grain size distribution, and with it grain coagulation and shattering physics, which can greatly affect the accretion rate (small grains dominate gas-dust accretion) and SNe destruction efficiency (small grains are more easily destroyed compared to large grains). We also do not account for polycyclic aromatic hydrocarbons (PAHs), a subspecies of carbonaceous dust grains which are extremely small (<1 nm) and could dominate carbonaceous gas-dust accretion (but these may only be produced via grain shattering and would require tracking the aromatization of dust grains due to the local radiation field; Rau et al. 2019). Our dust models also do not incorporate a full, non-equilibrium chemical network even though molecular formation depends on the exact amount and size of dust grains either directly, by forming on grain surfaces (e.g. H_2), or indirectly, by depending on molecules which form on dust grains (e.g. CO). With these in mind, our goal here is to lay a solid foundation for the incorporation and investigation of such physics in future works.

2.6 Acknowledgements

We thank I-Da Chiang, Lichen Liang, and Alexander J. Richings for insightful suggestions and advice. CC and DK were supported by NSF grants AST-1715101 and AST2108314 and the Cottrell Scholar Award from the Research Corporation for Science Advancement. Numerical calculations were run on the UC San Diego Triton Shared Computing Cluster, and allocations AST20016 & TG-AST140023 supported by the NSF and TACC. Support for PFH was provided by NSF Research Grants 1911233 & 20009234, NSF CAREER grant 1455342, NASA grants 80NSSC18K0562, HST-AR-15800.001-A. KS was supported by National Science Foundation grant No. 1615728. CAFG was supported by NSF through grants AST-1715216, AST-2108230, and CAREER award AST-1652522; by NASA through grant 17-ATP17-0067; by STScI through grant HST-AR-16124.001-A; and by the Research Corporation for Science Advancement through a Cottrell Scholar Award. The data used in this work were, in part, hosted on facilities supported by the Scientific Computing Core at the Flatiron Institute, a division of the Simons Foundation. This work also made use of MATPLOTLIB (Hunter, 2007), NUMPY (Harris et al., 2020), SCIPY (Virtanen et al., 2020), the yt project (Turk et al., 2011), and NASA's Astrophysics Data System.

2.A Effects of variations in initial conditions

In Fig. 2.9 and Fig. 2.10 we show the resulting element depletions and D/Z relation versus $n_{\rm H,neutral}$ at the end of the simulation for the "Species" implementation (including Nano-iron and O-reservoir dust species) with our fiducial initial conditions, initial gas cell and stellar metallicity of $Z_{\rm init} = 0.5 Z_\odot$ with no initial dust population, and initial gas cell and stellar metallicity of $Z_{\rm init} = Z_\odot$ with an initial dust population for all gas cells. Specifically the initial dust population is assumed to be entirely from SNe II and is set by $\delta_{\rm Si} = 0.5$ with $\delta_{\rm Mg}$ and $\delta_{\rm O}$ set to match our defined silicate dust composition, $\delta_{\rm Fe} = 0.5$, and $\delta_{\rm C} = 0.25$ such that the silicate-to-carbon ratio ~2.5. This results in an initial D/Z~0.2. The $Z_{\rm init} = 0.5 Z_\odot$ simulation was evolved for 1.5 Gyr and resulted in a median gas metallicity of $Z = 0.75 Z_\odot$ while the initial dust population simulation was evolved for 0.7 Gyr (the time at which $\sim 90\%$ of the galactic dust mass is composed of "new" dust produced by gas-phase accretion compared to the initial SNe II dust population) and resulted in a median gas metallicity of $Z = 1.15 Z_{\odot}$. The results are roughly consistent across the observed range with similar depletion trends for all elements, but there are small systematic offsets compared to our fiducial run largely due to the overall lower median gas metallicity at simulation end which reduces the gas-dust accretion rate. The largest difference is the drastically reduced element depletions and D/Z in the most diffuse gas for the $Z_{\rm init} = 0.5 Z_{\odot}$ simulation. This is due to the reduced cycling of gas into and out of cool, dense environments. The reduced metallicity reduces the efficiency of metal-line cooling in hot gas which in turn reduces the amount of cool, dense gas that is formed in the galaxy by a factor of $\sim$0.5. Fully cosmological simulations will be needed to further investigate the effects of galactic metallicity on the resulting element depletions and D/Z.

2.B Sub-Resolution treatment of dense molecular gas chemistry

In order to accurately model gas-dust accretion for carbonaceous dust grains and account for Coulomb enhancement terms we must track the mass fraction of the gas that is in the dense molecular phase ($f_{\rm dense}$), where we assume that (1) nearly all gas-phase metals are neutral (so Coulomb enhancement terms are negligible) and (2) specifically gas-phase carbon is almost completely molecular in the form of CO (e.g. Snow & McCall, 2006) and unavailable for carbonaceous dust growth.[22] Note in this work we do not use $f_{\rm dense}$ to account for sub-resolution density/temperature structure in our gas-dust accretion routine.

To calculate $f_{\rm dense}$ we employ a method similar to Krumholz & Gnedin (2011), which is used in FIRE-2 to estimate the molecular mass fraction ($f_{\rm H_2}$) of gas cells. Specifically, this method assumes the gas cell is an idealized spherical cloud immersed in a isotropic dissociating

[22]In extremely dense, cold environments ($n_{\rm H} \geq 10^5$ cm^{-3}, $T < 20$ K) CO does 'freeze-out', forming icy mantles on the surface of dust grains (e.g. Boogert et al., 2015) but we do not track this.

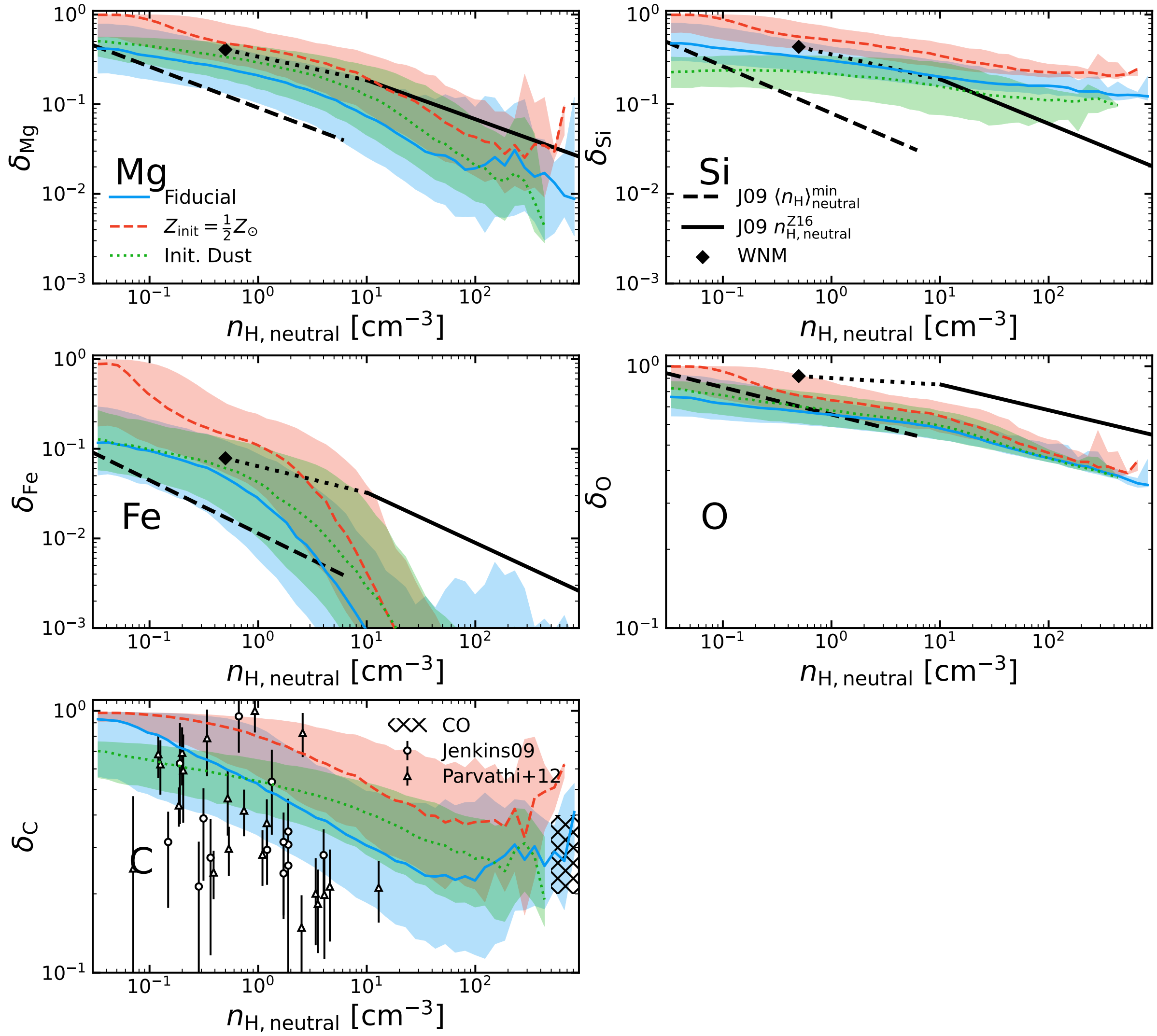

Figure 2.9. Same as Fig. 2.6 comparing our "Species" implementation (including Nano-iron and O-reservoir dust species) with our fiducial initial conditions (*solid*), with initial gas and stellar metallicity of $Z_{\rm init} = 0.5 Z_\odot$ (*dashed*), and with an initial dust population in all gas cells (*dotted*). Overall the resulting element depletions are quite similar for the different initial conditions, but with a small systematic offsets due to differences in gas-dust accretion rates which depend on the gas metallicity. The large differences for the $Z_{\rm init} = 0.5 Z_\odot$ run at low densities is due to the reduced efficiency of metal-line cooling which reduces the cycling of gas into and out of cool, dense environments.

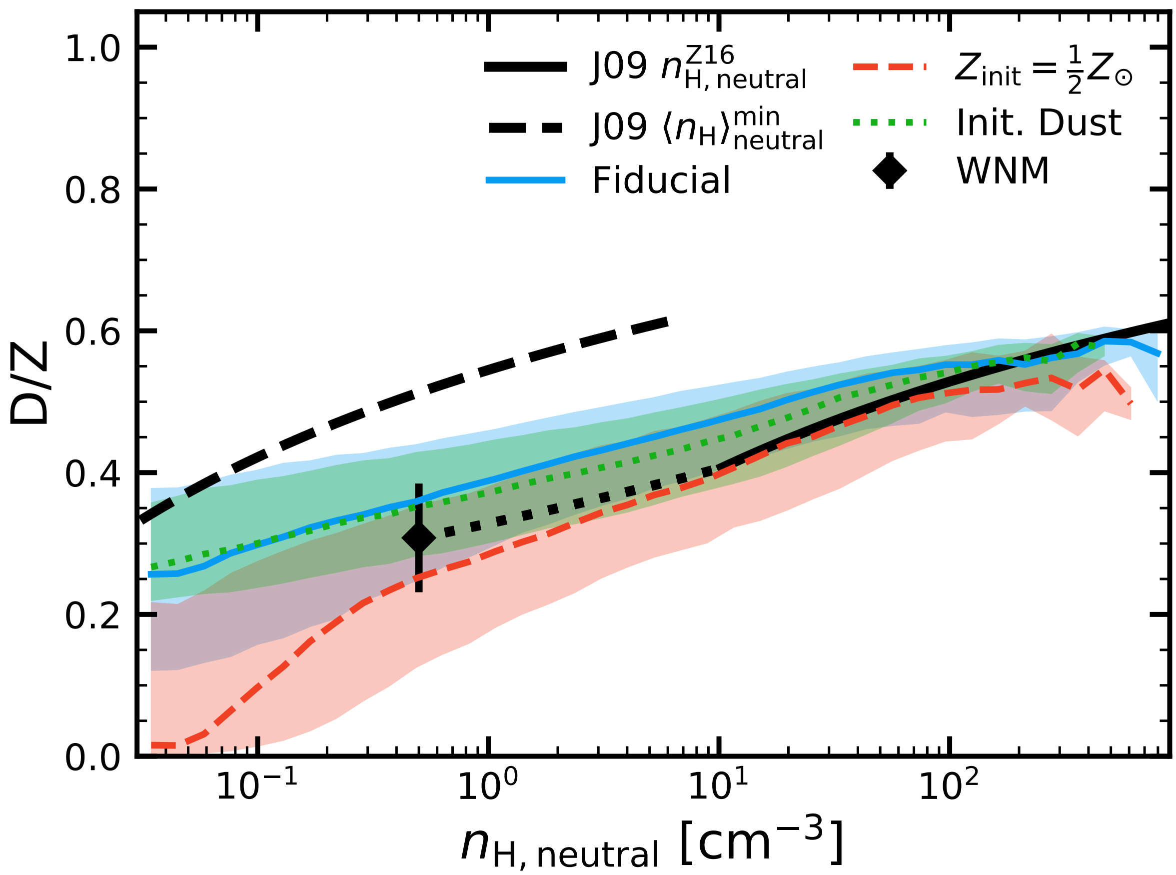

Figure 2.10. Same as Fig. 2.7 comparing our "Species" implementation (including Nano-iron and O-reservoir dust species) with our fiducial initial conditions (*solid*), with initial gas and stellar metallicity of $Z_{\rm init} = 0.5 Z_\odot$ (*dashed*), and with an initial dust population in all gas cells (*dotted*). The small systematic offsets between the runs for $n_{\rm H,neutral} \geq 0.5$ is due to differences in gas-dust accretion rates which depend on the gas metallicity. The sharp decrease in D/Z for the $Z_{\rm init} = 0.5 Z_\odot$ run at $n_{\rm H,neutral} < 0.5$ is due to the reduced efficiency of metal-line cooling which reduces the cycling of gas into and out of cool, dense environments.

radiation field, with an assumed shielding length ($r_{\rm shield}$) and metallicity used to estimate the total integrated column density of the gas cell to this radiation. Based on the column density, a depth into the cloud is then determined beyond which the gas is self-shielded and molecular, which in turn determines $f_{\rm H_2}$. FIRE-2 uses a Sobolev+cell approximation for $r_{\rm shield}$ which accounts for the average contribution of neighboring gas cells and actual contribution of the main cell to the column depth respectively (see Hopkins et al. 2018a). In a similar fashion, for determining $f_{\rm dense}$ we assume a spherical gas cell with radius equal to the Sobolev+cell shielding length. We then look to observations to determine what column depths are typical for gas to transition between the diffuse/C-rich and dense molecular/CO-rich phase. Observations have found that CO quickly takes over as the dominant form of gas-phase C over a very narrow range of sight line H_2 column densities (Liszt, 2007; Sheffer et al., 2008), and so we assume a critical H_2 column density ($N^{\rm crit}_{\rm H_2}$) above which carbon immediately converts to CO and the gas is in dense molecular phase (we also for simplicity assume the same threshold for where the ionized metal fraction becomes negligible, although this may occur at different column densities in reality). With this assumption, along with assuming the H_2 tracked by $f_{\rm H_2}$ in FIRE is evenly distributed within the gas cell, we calculate the depth into the gas cloud needed to reach this critical H_2 column density as

$$d = \frac{2N^{\rm crit}_{\rm H_2}}{f_{\rm H_2} n_{\rm H}} \tag{2.25}$$

where $n_{\rm H}$ is the hydrogen number density of the gas cell tracked in our simulation. We then assume that all gas past this depth within the cell is in the dense molecular phase. Thus we determine the fraction of gas cell in the dense molecular phase as

$$f_{\rm dense} = \frac{(r_{\rm shield} - d)^3}{r^3_{\rm shield}}. \tag{2.26}$$

We then track and update $f_{\rm dense}$ at each time-step in our simulation and with this we also track the fraction of total C (in gas and dust) locked in CO ($f_{\rm CO}$) for each gas cell based on the current fraction of atomic gas-phase C (not in dust or CO), $f_{\rm C,gas}$, specifically $f_{\rm CO}^{\rm new} = f_{\rm CO}^{\rm old} + \frac{(f_{\rm dense}^{\rm new} - f_{\rm dense}^{\rm old})}{1 - f_{\rm dense}^{\rm old}} f_{\rm C,gas}$. Note $f_{\rm C,gas}$ can change between time steps due to the injection of gas-phase C from metal producers or turbulent diffusion and/or the accretion of gas-phase C onto dust. Also, since we do not follow the exact physical location of CO in our gas cells, when $f_{\rm dense}$ decreases between time steps we simply reduce $f_{\rm CO}$ such that $f_{\rm CO}^{\rm new} = \frac{f_{\rm dense}^{\rm new}}{f_{\rm dense}^{\rm old}} f_{\rm CO}^{\rm old}$. It should also be noted that since we average the contribution of neighboring gas cells and assume they have similar H_2 densities, this could overestimate $f_{\rm dense}$, and thus $f_{\rm CO}$, in complex configurations such as near the edge of molecular clouds where there could be a sharp gradient in $f_{\rm H_2}$ and $n_{\rm H}$ for neighboring gas cells.

We tested the sensitivity of $f_{\rm dense}$ to the $N_{\rm H_2}^{\rm crit}$ parameter, with the resulting relations between $f_{\rm H_2}$, $f_{\rm dense}$, gas number density, and temperature given in Fig. 2.11. Using the "Species" dust model, we decided on a $N_{\rm H_2}^{\rm crit} = 1.5 \times 10^{21}$ cm^2 which produces an average $f_{\rm CO} \approx 30\%$ in the densest environments at simulation end, which falls in the middle of the observed $f_{\rm CO}$ range (e.g. Irvine et al., 1987; van Dishoeck et al., 1993; van Dishoeck & Blake, 1998; Lacy et al., 1994). This choice of $N_{\rm H_2}^{\rm crit}$ is also in good agreement with observations, falling roughly in the middle of the observed transition between diffuse and dense molecular gas and low to high $N_{\rm CO}$ (Sheffer et al., 2008, see Fig. 7).

2.C Effects of variations in stellar dust formation prescriptions

Fig. 2.12 and 2.13 show resulting galaxy-integrated D/Z and dust mass fractions (as Fig. 2.3 and 2.4) for models where we arbitrarily vary the rates of dust formation/creation from stellar AGB outflows and SNe. For the "Elemental" implementation we tested a model in which we (1) decreased the mass of dust created in SNe by a systematic factor of 10, (2) did the same for dust created by AGB stars, and (3) replaced our default "Elemental" dust creation rates with the default creation rates from the "Species" model. For the "Species" implementation we tested

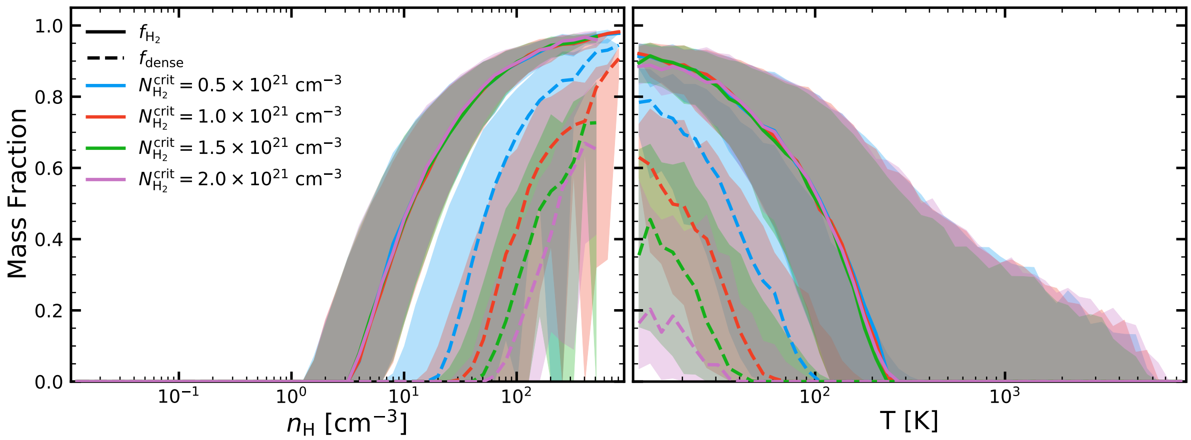

Figure 2.11. Resulting median molecular mass fraction (f_{H_2}) (*solid*) predicted in our simulated galaxy's ISM gas and median mass fraction of gas in dense molecular phase (f_{dense}) (*dashed*) produced by our model (Appendix 2.B) versus n_H (*left*) and T (*right*) of all simulation gas cells, with 16-/84-percentile represented by shaded regions. We show the sensitivity of these results to our choice of $N_{H_2}^{crit}$ (Eq. 2.25). Note f_{H_2} does not depend on $N_{H_2}^{crit}$ and so any differences between runs is purely stochastic.

(1) increasing the mass of dust formed by SNe by a systematic factor of 10, (2) did the same for dust produced by AGB stars, and (3) replaced our default "Species" dust creation rates with the default creation rates from the "Elemental" model. These variations cause the initial dust population to differ drastically, in composition and amount, at early times but these differences quickly subside as gas-dust accretion takes over, becoming the dominant source of dust mass growth and producing near identical galaxy-integrated D/Z and dust composition at simulation end.

2.D Importance of the Coulomb Enhancement and Molecular CO Terms

In Fig. 2.14 and Fig. 2.15 we show the resulting element depletions and D/Z relation versus $n_{H,neutral}$ at the end of the simulation for the "Species" implementation (including Nano-iron and O-reservoir dust species) with and without including our default Coulomb enhancement term and removing the fraction of C locked in CO. Examining the element depletions for Mg, Si, and Fe it is apparent that at least for our default assumptions, without accounting for the Coulomb

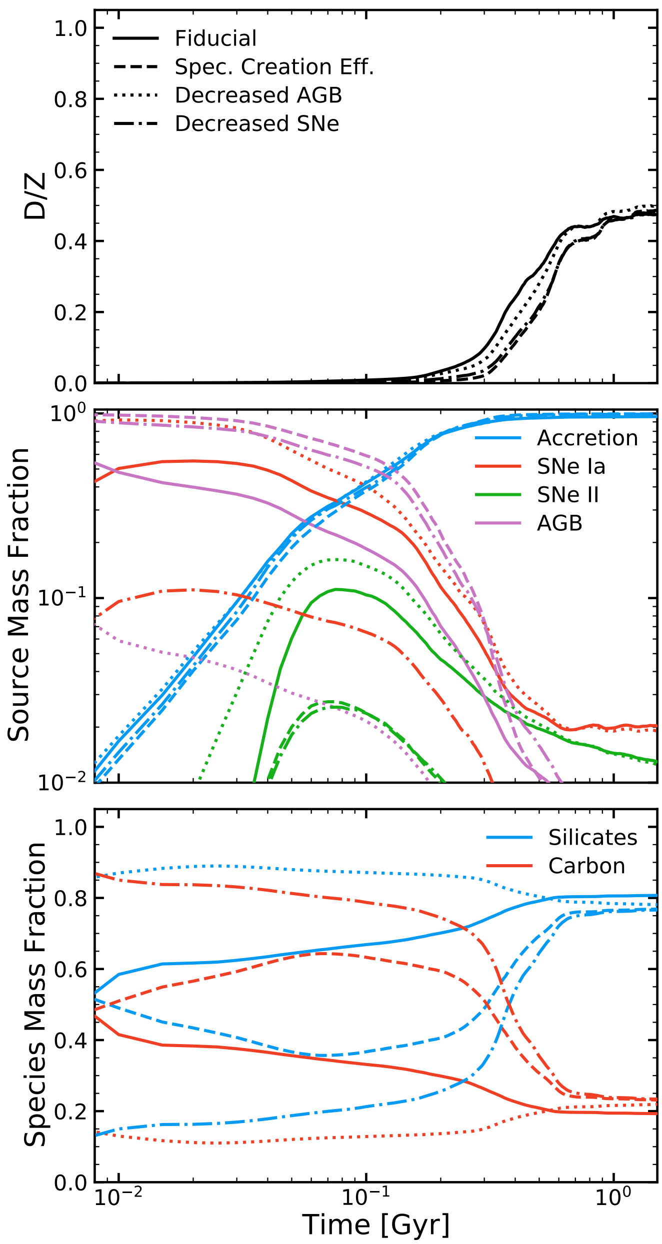

Figure 2.12. Same as Fig. 2.3 but varying our assumed creation/formation efficiencies for the "Elemental" implementation of dust. We compare the "Elemental" implementation with the fiducial model (*solid*), using default "Species" SNe and AGB dust production rates (*dashed*), factor of 10 decrease in AGB dust production (*dotted*), and factor of 10 decrease in SNe dust production (*dash-dotted*). The effects at simulation end are small.

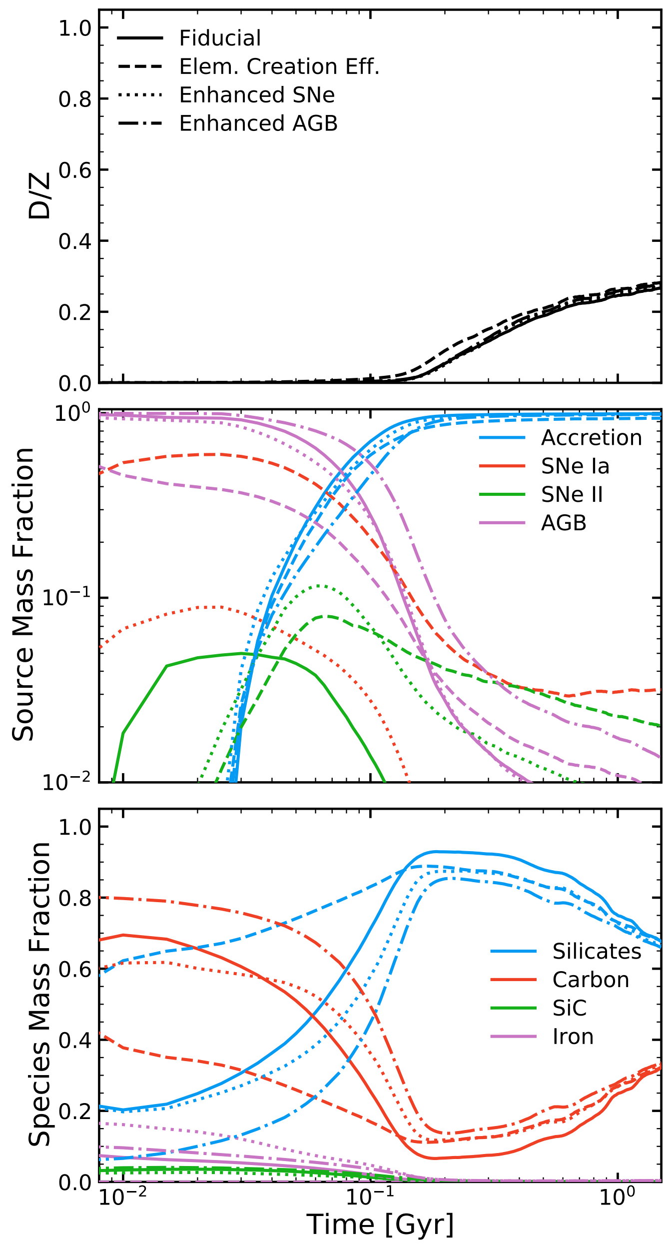

Figure 2.13. Same as Fig. 2.4 but varying our assumed dust creation/formation efficiencies for the "Species" implementation of dust. We compare the "Species" implementation with the fiducial model (*solid*), using default "Elemental" SNe and AGB dust production rates (*dashed*), factor of 10 increase in SNe dust production (*dotted*), and factor of 10 increase in AGB dust production (*dash-dotted*). The effects are generally small, as the system rapidly reaches steady-state in which gas-dust accretion dominates. Note the differences in SNe II dust source fractions at early times is due to run-to-run variations in SNe II events and our galaxy being initially free of dust.

enhancement term, accretion onto silicates and metallic iron dust is too slow, sequestering too little metal mass into dust. In the case of C, accretion rates for carbonaceous dust are hardly changed by Coulomb enhancement (see Table 2.2), but explicitly accounting for the fraction of C in CO has noticeable effects. When C in CO is not accounted for, the expected C depletion in dense environments is too high, consuming nearly all C (so, by construction, not enough residual C would be available for the observed CO). These changes to the element depletions result in a systematically lower D/Z relation for all but the densest gas, but even here this is a result of too much C being locked up in dust.

2.E Effects of Different Metal Yields - A Comparison between FIRE-2 and FIRE-3

All our simulations in the main text used the FIRE-2 version of the FIRE code, following Hopkins et al. (2018a) with minor modifications as described in Section 2.3.1. The next version of FIRE, FIRE-3 (Hopkins et al., 2023), makes a variety of improvements to the stellar inputs and numerical methods, focusing in particular on updating the stellar evolution tracks used for stellar feedback and nucleosynthesis with newer, more detailed models, as well as improving the detailed thermochemistry of cold atomic and molecular ISM gas, and adopting the newer Asplund et al. (2009) proto-solar reference abundances with $Z \sim 0.014$. We have made a preliminary comparison, running simulations with our dust models (specifically the "Species" model including both O-reservoir and Nano-iron species) coupled to the FIRE-3 instead of FIRE-2 models. While there are a variety of small differences, we find that the most important is related to the updated nucleosynthetic yields. The FIRE-3 yields include updated AGB mass loss rates which are reduced compared to FIRE-2 in better agreement with recent observational constraints (e.g. Kriek et al., 2010; Melbourne et al., 2012; Zibetti et al., 2013; Smith, 2014; Höfner & Olofsson, 2018), making the dust creation somewhat more dominated by SNe (though as with our default model, this has weak overall effect). The primary difference comes from the

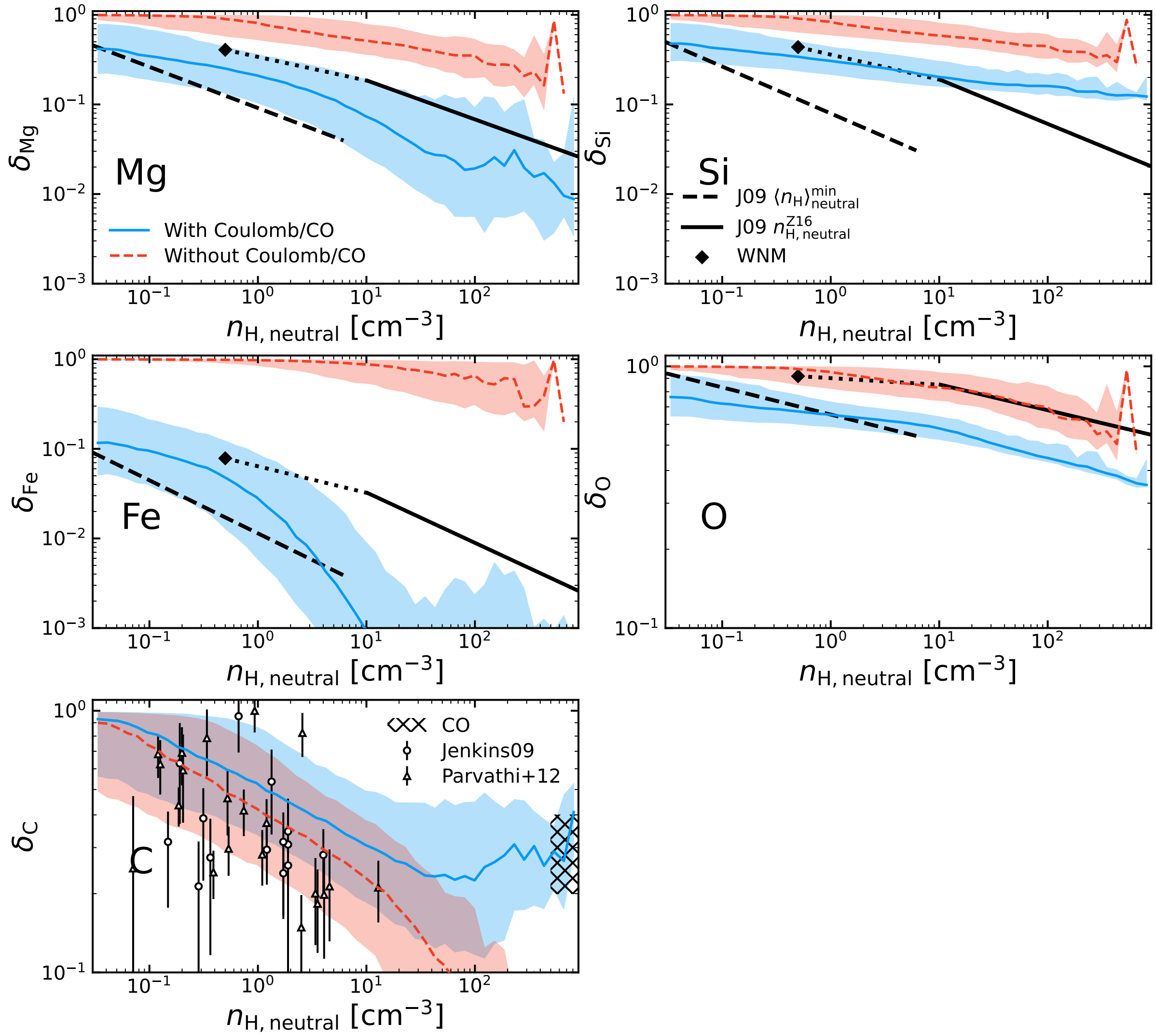

Figure 2.14. Same as Fig. 2.6 comparing our default "Species" implementation (including Nano-iron and O-reservoir dust species) with (*solid*) and without (*dashed*) the default terms which attempt to account for Coulomb enhancement of gas-phase accretion rates, and the fraction of C unavailable to dust as it is locked into CO. The former has an appreciable effects on the predicted depletion of Mg, Si, Fe, and O. The latter only influences C depletion at high densities: without it, all C is locked in dust which of course would be inconsistent with observed CO abundances.

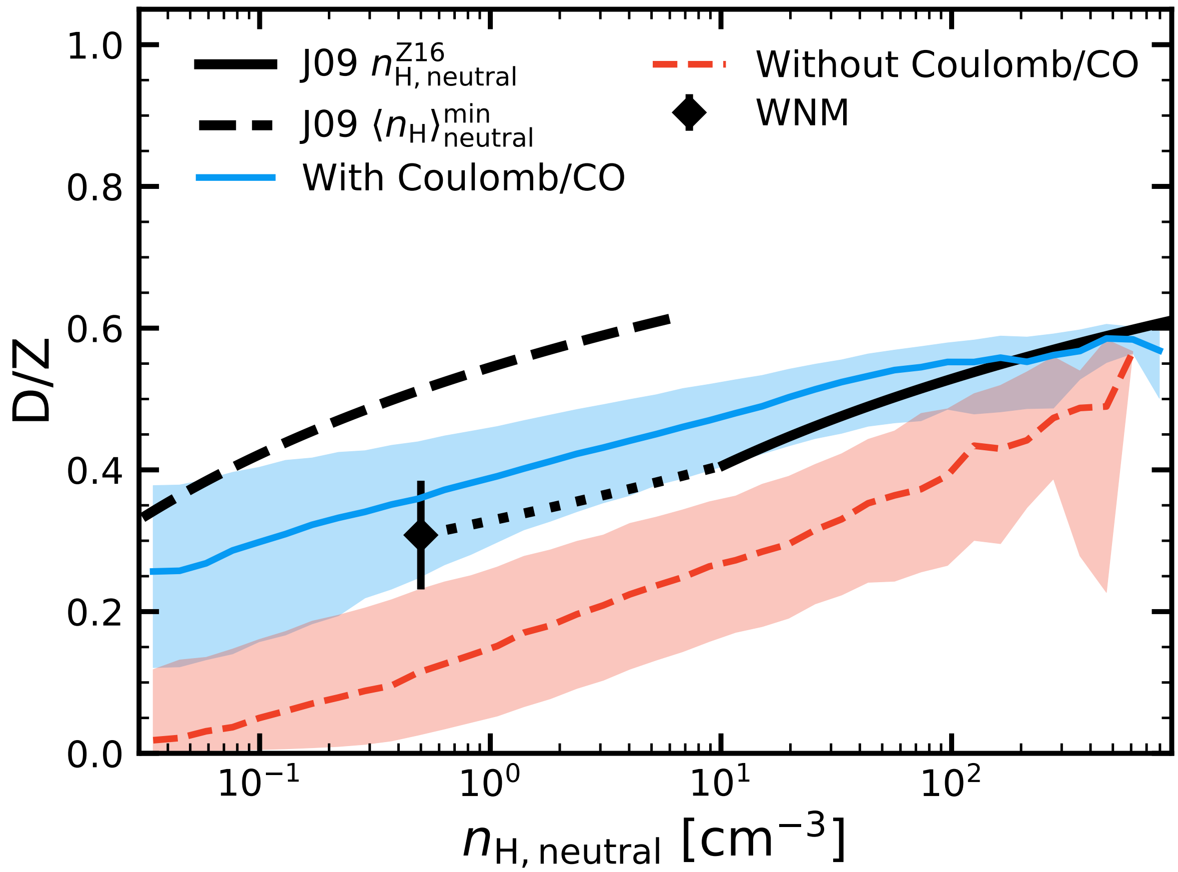

Figure 2.15. Same as Fig. 2.7 comparing our default "Species" implementation (including Nano-iron and O-reservoir dust species) with (*solid*) and without (*dashed*) the default terms which attempt to account for Coulomb enhancement of gas-phase accretion rates, and the fraction of C unavailable to dust as it is locked into CO. The former systematically lowers D/Z at all densities. The latter increases the D/Z in dense gas but is the result of near all C locked in dust.

FIRE-3 core-collapse SNe yields, based on a synthesis of the updated yield models in Nomoto et al. (2013); Pignatari et al. (2016); Sukhbold et al. (2016); Limongi & Chieffi (2018); Prantzos et al. (2018). These are compared to FIRE-2 in Fig. 2.16. While C and O yields differ from FIRE-2 at an appreciable level, these actually have little effect on the steady-state dust population (influencing only the early-time production, for the reasons in Section 2.4.1). The most subtle but interesting change is that Mg is produced more promptly while Si is slightly reduced: this slightly increases the ratio of Mg to Si in FIRE-3, making Si instead of Mg the key element for silicate dust growth. In Fig. 2.17 & 2.18, we see this produces a significantly steeper depletion-density relation for Si while not appreciably changing the other element depletions and D/Z trends across the range of observations. It is however important to note that this is somewhat degenerate with our assumed dust chemical compositions: we could also make Si the key element in FIRE-2 by decreasing the assumed Mg-to-Si ratio "$A_{\rm Mg}/A_{\rm Si}$" for the mean silicate composition (see Section 2.3.3).

Chapter 2, in full, is a reformatted version of the published material in *Monthly Notices of the Royal Astronomical Society*, Caleb R. Choban; Dušan Kereš; Philip F. Hopkins; Karin M. Sandstrom; Christopher C. Hayward; Claude-André Faucher-Giguère Volume 514, Issue 3, August 2022, Pages 4506–4534. The dissertation author was the primary investigator and author of this paper.

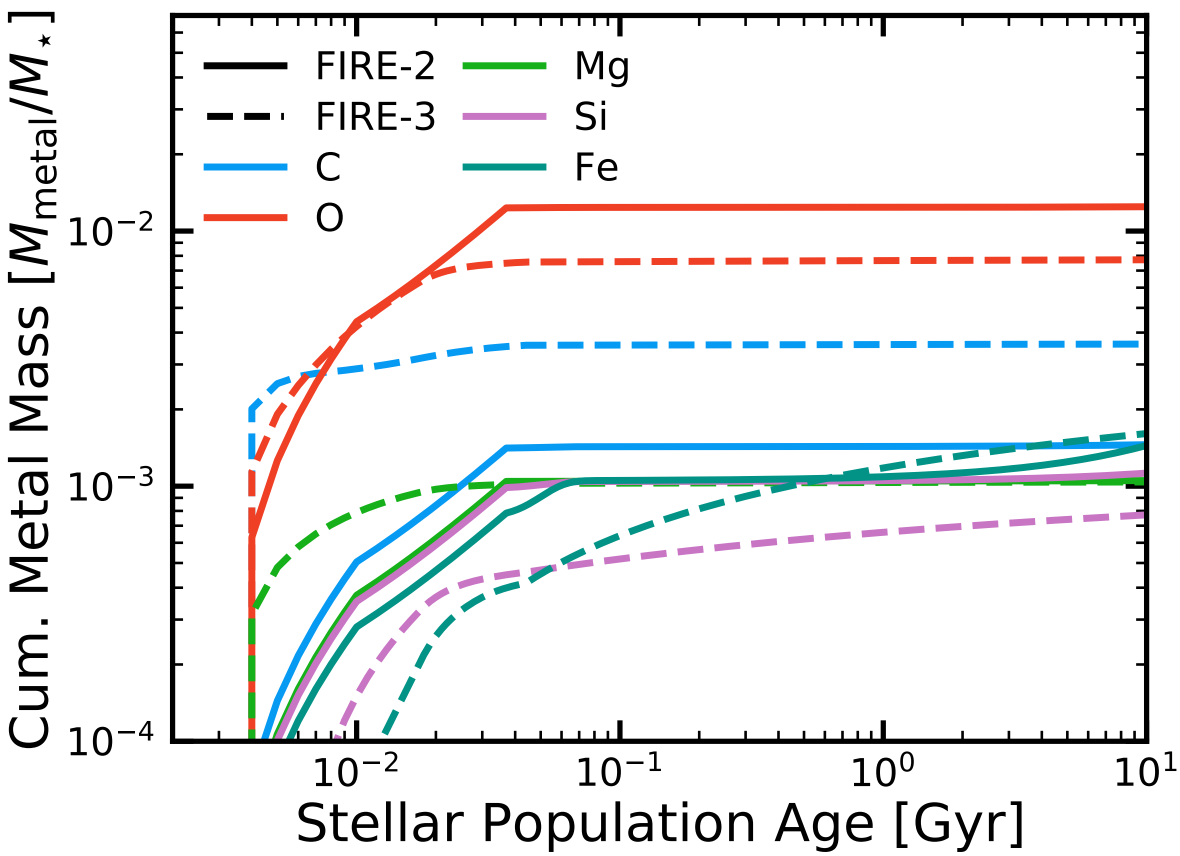

Figure 2.16. Cumulative SNe metal yields per stellar mass for main refractory elements in dust over a stellar population's life for the assumed yield models in FIRE-2 (from Nomoto et al. 2006) and FIRE-3 (from the synthesis of Nomoto et al. 2013; Pignatari et al. 2016; Sukhbold et al. 2016; Limongi & Chieffi 2018; Prantzos et al. 2018). Note these yields are not metallicity dependant.

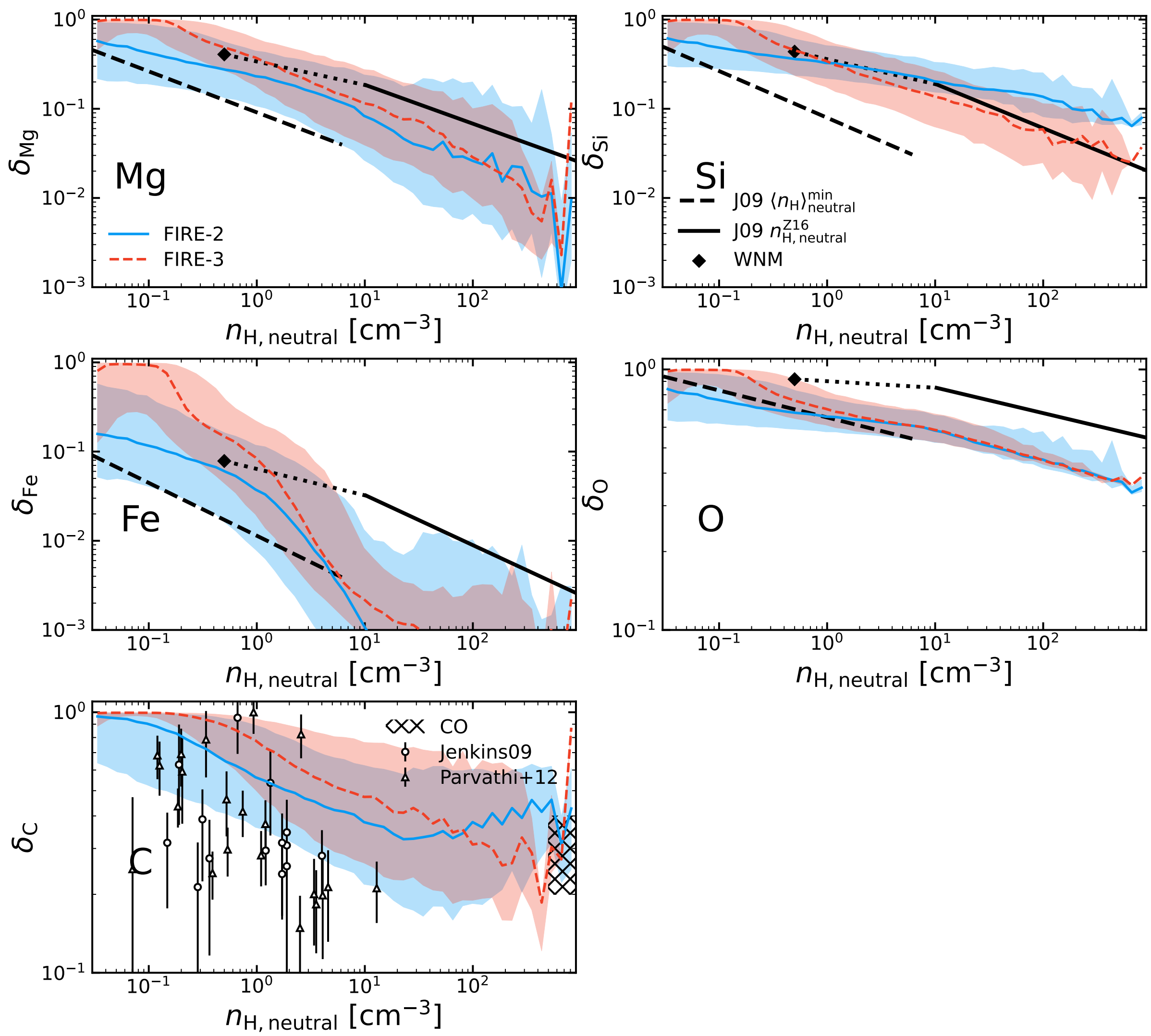

Figure 2.17. Same as Fig. 2.6 comparing the "Species" implementation with O-reservoir and Nano-iron dust species integrated with FIRE-2 or FIRE-3 stellar feedback and ISM physics. The updated nucleosynthetic yields of FIRE-3 produce a better match to expected depletion trends for Si while not appreciably changing the depletion trends of the other elements over the range of observations.

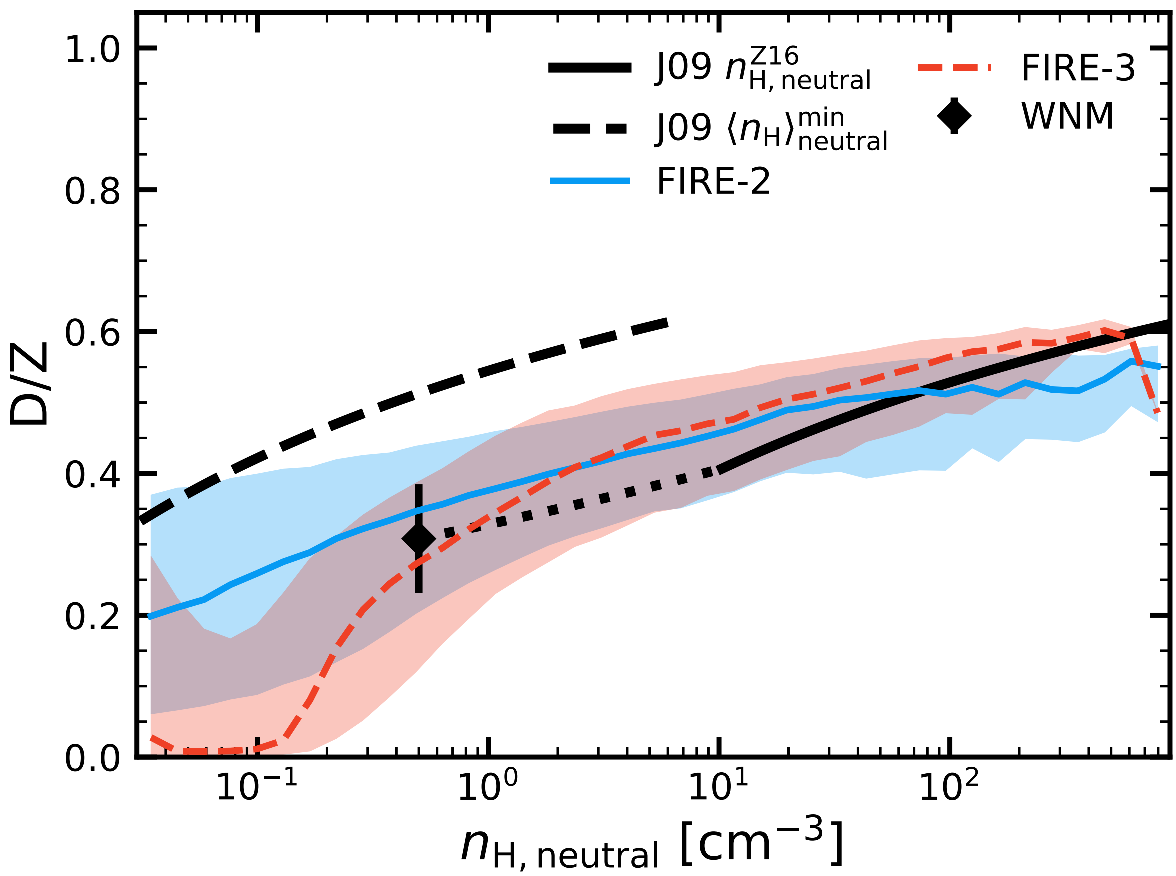

Figure 2.18. Same as Fig. 2.7 comparing the "Species" implementation including Nano-iron and O-reservoir dust species integrated with FIRE-2 and FIRE-3 stellar feedback and ISM physics. The resulting D/Z trends do not diverge appreciably over the range of observations.

Chapter 3

A Dusty Locale: Evolution of Galactic Dust Populations from Milky Way to Dwarf-Mass Galaxies

3.1 Abstract

Observations indicate dust populations vary between galaxies and within them, suggesting a complex life cycle and evolutionary history. Here we investigate the evolution of galactic dust populations across cosmic time using a suite of cosmological zoom-in simulations from the Feedback in Realistic Environments (FIRE) project, spanning small to large halo mass galaxies ($M_{\rm vir}$=10^{9-12}M$_{\odot}$; M_{*}=10^{6-11} M$_{\odot}$). Our simulations incorporate a dust evolution model that accounts for the dominant sources of dust production, growth, and destruction and follows the evolution of specific dust species with set chemical compositions. All galactic dust populations in our suite exhibit similar evolutionary histories, with gas-dust accretion being the dominant producer of dust mass for all but the most metal-poor galaxies. The onset of efficient gas-dust accretion occurs above a 'critical' metallicity threshold ($Z_{\rm crit}$). This threshold varies between dust species due to differences in key element abundances, dust physical properties, and life cycle processes resulting in $Z_{\rm crit}$~$0.05{\rm Z}_{\odot}, 0.2{\rm Z}_{\odot}, 0.5{\rm Z}_{\odot}$ for metallic iron, silicates, and carbonaceous dust, respectively. This variation in $Z_{\rm crit}$ could explain the relative lack of small carbonaceous grains observed in the Large and Small Magellanic Clouds. We also find a delay between the

onset of gas-dust accretion and when a dust population reaches equilibrium, which we call the equilibrium timescale ($\tau_{\rm equil}$). The relation between $\tau_{\rm equil}$ and the metal enrichment timescale of a galaxy, determined by its recent evolutionary history, can contribute to the scatter in the observed relation between galactic D/Z and metallicity.

3.2 Introduction

Observations of the Milky Way (MW) and the Large and Small Magellanic Clouds (LMC & SMC) reveal significant variations in their respective dust populations. The 2175 Å feature/bump in dust extinction curves, which correlates with the abundance of small carbonaceous grains[1], shows a strong decrease between the Milky Way and LMC, and an almost complete lack of the feature for the SMC (e.g. Pei, 1992; Weingartner & Draine, 2001a). Mid-infrared dust emission produced by polycyclic aromatic hydrocarbons (PAHs) shows a dramatic decrease in the average fraction of dust mass comprised of PAHs ($q_{\rm PAH}$; Draine & Li 2007) from the Milky Way (~4.6%) to the LMC (~3.3%) and SMC (~1.0%) (Li & Draine, 2001; Weingartner & Draine, 2001a; Chastenet et al., 2019). Gas-phase element depletions in the MW, LMC, and SMC reveal a considerable variation in dust chemical composition and an overall decreasing fraction of metals locked in dust (dust-to-metals ratio; D/Z), which corresponds with their relative metallicities (Roman-Duval et al., 2022a). However, the lack of observed C and O depletions in the LMC and SMC results in an incomplete picture of their dust chemical composition.

Looking further afield, extragalactic observations of local galaxies tell a similar story. Dust emission surveys find an overall increase of galaxy-integrated D/Z with metallicity along with a large (>1 dex) scatter at any given metallicity, but the exact relation varies between studies (Rémy-Ruyer et al., 2014; De Vis et al., 2019). These studies also find a linear dependence of

[1]While it is currently unknown whether PAHs or small carbonaceous grains (i.e. amorphous graphite) are the dominant candidate for the 2175 Å feature, their life cycles could be intimately linked. One proposed formation mechanism for PAHs is through photoprocessing, where hydrogen atoms are removed from small carbonaceous dust grains (i.e. aromatization; Rau et al., 2019; Hirashita & Murga, 2020; Narayanan et al., 2023). Although other possible formation sources in AGB winds (Galliano et al., 2008) or directly through low-temperature chemical channels in dense molecular clouds (Parker et al., 2012) have not been ruled out.

$q_{\rm PAH}$ with logarithmic metallicity and a threshold galactic metallicity of $12+\log_{10}(\rm O/H) \sim 8.0$ above which $q_{\rm PAH}$ rapidly increases (Draine et al., 2007; Rémy-Ruyer et al., 2015; Aniano et al., 2020). Local and high-z dust attenuation curves in galaxies exhibit a wide range of 2175 Å feature strengths (e.g. Salim & Narayanan, 2020; Shivaei et al., 2022). However, it is unclear whether the strength/absence of this feature is due to the underlying dust population derived extinction curve or radiative transfer effects caused by interstellar medium (ISM) clumpiness, star-dust geometry, and albedo effects (Granato et al., 2000; Panuzzo et al., 2007; Seon & Draine, 2016; Narayanan et al., 2018). Observations of damped Lyα systems (DLAs) show increasing gas-phase element depletions with metallicity and no clear relation with redshift (Péroux & Howk, 2020; Roman-Duval et al., 2022b). These observations suggest an evolving dust population in both amount and chemical composition, with a decreasing total fraction of metals locked in dust and a scarcity of carbonaceous dust in low metallicity environments. The exact cause of this is unknown, but detailed dust evolution models that account for the main processes of the dust life cycle coupled with galaxy formation models can help elucidate this issue.

The current dust life cycle paradigm posits all dust grains begin their life in the ejecta of Type II supernovae (SNe II) and stellar winds of asymptotic giant branch (AGB) stars, where a fraction of metals within these winds coalesce into dust (Draine, 1990; Todini & Ferrara, 2001; Ferrarotti & Gail, 2006). The grains are then primarily destroyed by SNe shocks, and in isolation, stellar dust production alone cannot explain the dust content of either the Milky Way (e.g. McKee, 1989; Draine, 2009) or LMC (Zhukovska & Henning, 2013), requiring another growth/production mechanism. Observations of gas-phase element depletions (Jenkins, 2009; Roman-Duval et al., 2021) and dust emission (Roman-Duval et al., 2014, 2017; Clark et al., 2023) show D/Z increases from diffuse to dense regions of the Milky Way and Local Group galaxies. These provide strong evidence that dust grows via the accretion of gas-phase metals in dense environments and could be the main producer of dust mass within these galaxies. However, the exact details of the accretion process are poorly understood, and many questions have yet to be completely answered. *When does gas-dust accretion become efficient, and does it differ between dust species? How long does it take for accretion to build up a sizable dust mass within a galaxy? Can accretion explain dusty galaxies at high redshift?*

Analytical galactic dust evolution models were first developed to answer these questions, giving rise to the concept of a 'critical' metallicity ($Z_{\rm crit}$) threshold (Inoue, 2011; Asano et al., 2013; Zhukovska, 2014; Feldmann, 2015; Popping et al., 2017; Triani et al., 2020). While the exact definition varies between works, they all agree there is a 'critical' metallicity above which gas-dust accretion becomes the dominant source of dust mass, rapidly increasing the expected galactic D/Z[2]. Inoue (2011) found that $Z_{\rm crit}$ is determined by the competition between growth via accretion and destruction via SNe shocks. However, equilibrium models developed by Feldmann (2015) suggest the dilution of dust via dust-poor gas inflows dominates over destruction via SNe shocks when determining $Z_{\rm crit}$, especially for dwarf galaxies. Zhukovska et al. (2008) developed analytical models which tracked the evolution of specific dust species and found that for a Milky Way-mass galaxy, silicates, carbonaceous, and metallic iron dust species have different $Z_{\rm crit}$. In later works, this model was used to investigate the evolution of dust within late-type dwarf galaxies experiencing episodic starbursts (Zhukovska, 2014). They concluded that such galaxies have lower $Z_{\rm crit}$ than galaxies with constant star formation due to long quiescent periods between starbursts where dust has ample time to grow.

More recently, numerical dust evolution models integrated into galaxy formation and evolution simulations have been put to the task (e.g. Bekki, 2015a; McKinnon et al., 2016; Zhukovska et al., 2016; McKinnon et al., 2017; Aoyama et al., 2020; Granato et al., 2021). The dust evolution models utilized in these works differ in their methodology and included physics and the galaxy simulations employed primarily encompass cosmological volumes, relying on varying sub-resolution star formation, feedback, and ISM prescriptions. Despite these differences, they all agree with the 'critical' metallicity concept (albeit with a large range $Z_{\rm crit}{\sim}0.03-0.2\mathrm{Z}_\odot$)

[2]These findings are not unanimous among all works. In particular, Priestley et al. (2022) suggests the contribution of dust growth via accretion may be overestimated if high stardust creation efficiencies and increased SNe dust destruction in low metallicity environments are assumed

above which the average galactic D/Z rapidly increases due to dust growth via accretion (Hou et al., 2019; Li et al., 2019; Graziani et al., 2020; Parente et al., 2022). A majority of these works also find that $Z_{\rm crit}$ and resulting relation between D/Z and Z have little evolution over redshift[3]. However, the exact cause of the large scatter in observed D/Z at any given Z is debated. Parente et al. (2022) predicts this is due to the fraction of cold gas in each galaxy, with higher cold gas fractions allowing for the faster build-up of dust via accretion. Li et al. (2019) proposes a more complex dependence on galactic metal enrichment history reflected by Z and M_*, and evolutionary stages quantified by gas content and depletion timescales. Li et al. (2021) adds that variance in galactic mass-averaged grain sizes (and thus gas-dust accretion rates) can also drive this scatter. Regarding the differences in the evolution between silicate and carbonaceous dust species, Granato et al. (2021); Parente et al. (2022) predict that silicate growth lags behind carbonaceous growth due to the overall lower abundance of Si compared to C, with silicate dust only dominating the dust mass past $Z_{\rm crit} \gtrsim 0.15 \mathrm{Z}_\odot$, $M_* \gtrsim 10^{8.5} \mathrm{M}_\odot$.

While these models generally agree in terms of galaxy-integrated dust observations, they have major limitations which make them ill-suited tools for investigating the gas-dust accretion process. They do not resolve the multi-phase ISM, which is necessary to accurately model each process in the dust life cycle. Furthermore, most do not track the evolution of chemically distinct dust species, instead assuming a single, chemically ambiguous dust population, affecting how gas-dust accretion is modeled. Choban et al. (2022, C22 hereafter) developed two separate dust evolution models to investigate the effects of both these assumptions. They found that only a model which tracks the evolution of chemically-distinct dust species and incorporates a physically motivated, two-phase dust growth routine can reproduce the observed scaling relation between individual element depletions and D/Z with column density and local gas density in the Milky Way. This relation results from the equilibrium between SNe dust destruction and dust growth via accretion. Therefore, such a model is crucial for investigating the evolution

[3]We point the reader to Popping & Péroux (2022) for a direct comparison of the predicted relation between D/Z and Z and its evolution over redshift for a selection of analytical and numerical dust models.

of galactic dust populations and testing the importance of gas-dust accretion in that evolution. However, C22 only utilized simulations of an idealized, non-cosmological Milky Way-like galaxy. Due to their idealized nature, these simulations do not capture the formation and hierarchical growth of galaxies across cosmic time and do not include a realistic corona/disc-halo interface. Consequently, these predictions may not hold for the entire evolutionary history of a galaxy or lower-mass galaxies.

In this work, we present a subset of cosmological zoom-in simulations of Milky Way to dwarf-halo mass galaxies from the Feedback in Realistic Environments (FIRE) project[4] rerun with the integrated "Species" dust evolution model presented in C22. This model tracks the evolution of specific dust species with set chemical compositions and incorporates a physically motivated dust growth routine. With these simulations, we investigate how galactic dust populations evolve in both their amount and chemical composition, focusing on the determining factors for when gas-dust accretion dominates and how it differs between dust species. We find that gas-dust accretion is the dominant producer of dust mass for all but the most metal-poor galaxies and, in the case of the MW, dominates for the majority of the galaxy's life. We discover that the onset of rapid growth via gas-dust accretion differs between dust species, arising from differences in their key element abundances, physical properties, and life cycle processes. These differences can explain the variable dust population, in both amount and composition, in the MW, LMC, and SMC. We also find a delay between the onset of rapid dust growth via accretion and when a dust population reaches equilibrium between growth and destruction processes. The relation between this delay and the metal enrichment timescale of a galaxy can contribute to the scatter in observed D/Z at any given metallicity.

This paper is organized as follows. In Section 3.3, we provide a brief overview of our simulation sample along with the galaxy formation and dust evolution model used. In Section 3.4, we present the results of our simulations, focusing on the evolution of the galactic and dust population properties for each galaxy in Section 3.4.1 and comparing them with local

[4] http://fire.northwestern.edu

observations in Section 3.4.2 & 3.4.3. We discuss the concept of a 'critical' metallicity threshold, which marks the onset of efficient gas-dust accretion, in Section 3.5.1 and an 'equilibrium' timescale, which is the time over which a dust population's mass builds up via accretion to an effective equilibrium, in Section 3.5.2. Finally, we present our conclusions in Section 3.6.

3.3 Methodology

To study the evolution of galactic dust populations within Milky Way to dwarf-mass galaxies, we reran a subset of cosmological simulations from the FIRE suite presented in Hopkins et al. (2018a) and El-Badry et al. (2018). We selected 7 galaxies with a broad range of stellar ($10^6\,M_\odot < M_* < 10^{11}\,M_\odot$) and halo ($10^9\,M_\odot < M_{\rm vir} < 10^{12}\,M_\odot$) masses at present day. We give the exact details of the z=0 halo virial mass, virial radius, stellar mass, stellar half-mass radius, and mass resolution for each simulation in Table 3.1.

All simulations in this work are run with the GIZMO code base (Hopkins, 2015) in the meshless finite-mass (MFM) mode with FIRE-2 (Hopkins et al., 2018a) model of star formation and stellar feedback. FIRE-2 incorporates multiple sources of stellar feedback, specifically stellar winds (O/B and AGB), ionizing photons, radiation pressure, and supernovae (both Types Ia and II). Gas cooling is followed self-consistently for T = 10 - 10^{10} K including free-free, Compton, metal-line, molecular, fine-structure, and dust collisional processes while gas is also heated by cosmic rays, photo-electric, and photoionization heating by both local sources and a uniform but redshift dependent meta-galactic background (Faucher-Giguère et al., 2009), including the effect of self-shielding[5]. Star formation is only allowed in cold, molecular, and locally self-gravitating regions with number densities above $n_{\rm H} = 1000\,{\rm cm}^{-3}$.

Each star particle represents a stellar population with a known mass, age, and metallicity assuming a Kroupa (2002) initial mass function (IMF) from $0.1 - 100\,M_\odot$. The luminosity,

[5]Note that all cooling and heating processes and radiative transfer modeled in FIRE-2 are not coupled with our dust evolution models. Specifically, dust heating and cooling, radiative transfer, and H_2 formation assume a constant D/Z ratio, and metal-line cooling assumes no metals are locked in dust. In future works, we will fully integrate our dust evolution models with FIRE and investigate the effects on galaxy evolution.

Table 3.1. Parameters describing initial conditions of simulations in this paper. The m11v simulation is unique since there are two galaxies (labeled halo0 and halo2) about to merge at simulation end (~70 kpc away), with halo2's dark matter halo being a subhalo of halo0. **(1)** Name of simulation. **(2)** Virial mass of dark matter halo at z=0. **(3)** Virial radius of dark matter halo at z=0. **(4)** Stellar mass within $\leq 3R_{1/2}$ of the galactic center at z=0. **(5)** Stellar half-mass radius at z=0. **(6)** Mass of gas and star particles. **(7)** Additional notes for each simulation.

Name	$M_{\rm vir}$ ($M_\odot$)	$R_{\rm vir}$ (kpc)	M_* ($M_\odot$)	$R_{1/2}$ (kpc)	Resolution ($M_\odot$)	Notes
m12i	9.5E11	203	7.2E10	2.9	7100	MW-mass spiral
m11v_halo0	2.6E11	131	1.6E9	4.13	7100	intermediate-mass dwarf (SMC/LMC-like)
m11d	2.4E11	131	3.9E9	2.77	7100	LMC-like (several mergers before z~1)
m11e	1.3E11	107	1.4E9	1.89	7100	LMC-like (merger at z~0.1)
m11v_halo2	5.3E10	34.4	2.1E9	3.1	7100	intermediate-mass dwarf (LMC-like)
m11i	6.0E10	82.4	1.9E8	2.32	7100	intermediate-mass dwarf (SMC-like)
m10q	6.6E9	38.6	1.8E6	0.49	500	low-mass dwarf

mass loss rates, and SNe II rates of each star particle are calculated based on the STARBURST99 (Leitherer et al., 1999) libraries, and SNe Ia rates following Mannucci et al. (2006). Metal yields from SNe II, Ia, and AGB winds are taken from Nomoto et al. (2006), Iwamoto et al. (1999), and Izzard et al. (2004) respectively. Evolution of eleven species (H, He, C, N, O, Ne, Mg, Si, S, Ca, and Fe) is tracked for each gas cell. Sub-resolution turbulent metal diffusion is modeled as described in Su et al. (2017) and Escala et al. (2018). FIRE-2 adopts the older Anders & Grevesse (1989) solar metal abundances with $Z{\sim}0.02$ so whenever we mention solar abundances we are referring to the Andres & Gravesse abundances.

FIRE is ideally suited to investigate galactic dust evolution over cosmic time given its success in matching a wide range of observations related to galaxies, including the mass-metallicity relation and its evolution over redshift (Ma et al., 2016) and the Kennicutt–Schmidt star formation law (Orr et al., 2018). This success is owed to the high resolution, star formation criteria, cooling to low temperatures, and multi-channel stellar feedback of FIRE, all of which result in a reasonable ISM phase structure and giant molecular cloud (GMC) mass function (Benincasa et al., 2020). These also lead to the self-consistent development of galactic winds that eject large amounts of gas (Muratov et al., 2015; Anglés-Alcázar et al., 2017) and metals (Muratov et al., 2017; Hafen et al., 2019; Pandya et al., 2021) out of galaxies, preventing excessive star formation and leading to a plausible stellar-halo mass relation.

Our simulations utilize the integrated "Species" dust evolution model presented in C22, which we refer to the reader for full details. This model includes the dominant sources of dust production, tracking and differentiating between dust created from SNe Ia and II, AGB stars, and dust growth from gas-phase accretion in the ISM. It includes the dominant dust destruction mechanisms, accounting for dust destroyed by SNe shocks, thermal sputtering, and astration (dust destroyed during the formation of stars). These processes are modeled self-consistently, owing to the FIRE model's in-depth treatment of the multi-phase ISM and capacity to time-resolve individual SNe events (Hopkins et al., 2018b). Notably, we restrict gas-dust accretion to cool ($T \leq 300$ K) gas and destroy dust locally around individual SNe events, allowing us to track the local variability of dust in the ISM. We also follow the evolution of specific dust species (carbonaceous, silicates, and silicon carbide) and theoretical oxygen-bearing (O-reservoir) and nanoparticle metallic iron (Nano-iron) dust species with set chemical compositions. Consequently, this means each dust species has a key element[6] that limits their individual accretion growth rates and the maximum formable amount of said dust species. We also incorporate sub-resolution turbulent dust diffusion, which follows the metal diffusion prescription in FIRE, and a dense molecular gas scheme. This scheme is critical to account for Coulomb enhancement of gas-dust accretion in atomic/diffuse molecular gas and the reduction in carbonaceous dust accretion due to the lock-up of gas-phase C into CO in dense molecular gas.

3.4 Results

We first showcase mock HST *ugr* composite images of each galaxy to highlight the breadth of galaxy types and their varying dust structure contained in our simulation suite. Fig. 3.1 shows face-on and edge-on images of **m12i**, **m11d**, and **m11v_halo2**, and Fig. 3.2 shows face-on images for **m11v_halo0**, **m11e**, **m11i**, and **m10q** all at $z = 0$. These images use STARBURST99 (Leitherer et al., 1999) to compute the stellar spectra for each star particle given their age and metallicity. These are then ray-traced through the ISM using the tracked D/Z for each gas cell produced by our dust model along with assumed MW, LMC, or SMC dust opacities from Pei (1992) depending on the median gas cell silicate-to-carbonaceous dust mass (Sil-to-C) ratio[7] in each galaxy (MW~3, LMC~5., SMC~10)[8]. We then volume-render the observed images in each band and construct a *ugr* composite image as seen by a distant observer. **m12i**, **m11d**, **m11v_halo2**, **m11v_halo0**, and **m11e** show prominent and detailed dust structure to varying degrees, with dark patches produced by the attenuation of UV/optical light from dust tracing the dense gas in each galaxy. **m11i** and **m10q** have no distinguishable features produced by dust due

[6]Here key element refers to the element for which n/i has the lowest value, where n is the number abundance of the element and i is the number of atoms of the element in one formula unit of the dust species under consideration.

[7]We define this ratio as Sil-to-C $=(M_{\rm sil}+M_{\rm iron}+M_{\rm O-res})/M_{\rm carb}$ in our simulations.

[8]Assuming only MW dust opacities produces no noticeable differences in the color bands used for these images.

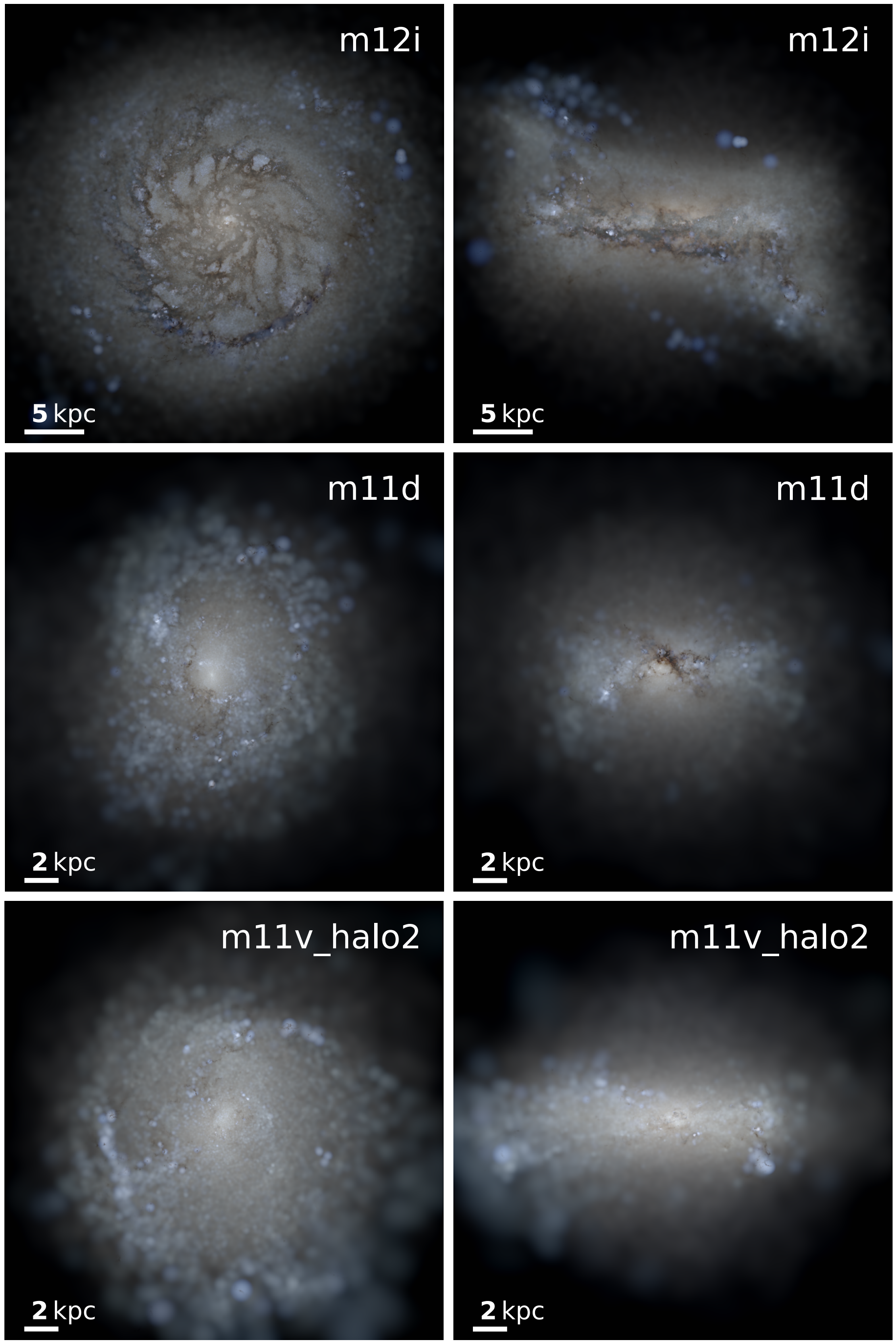

Figure 3.1. Face-on and edge-on images of our spiral and dwarf spiral galaxies at $z = 0$. Each image is a mock Hubble Space Telescope *ugr* composite. **m12i**: A compact, Milky Way-mass spiral galaxy that experienced multiple minor mergers which produced prominent flares at the disk's edge. **m11d**: An LMC-mass galaxy with noticeable voids and a thick disk resulting from bursty star formation and multiple mergers throughout its life. **m11v_halo2**: An LMC-mass galaxy with faint spiral arms that evolved in isolation for a majority of its life.

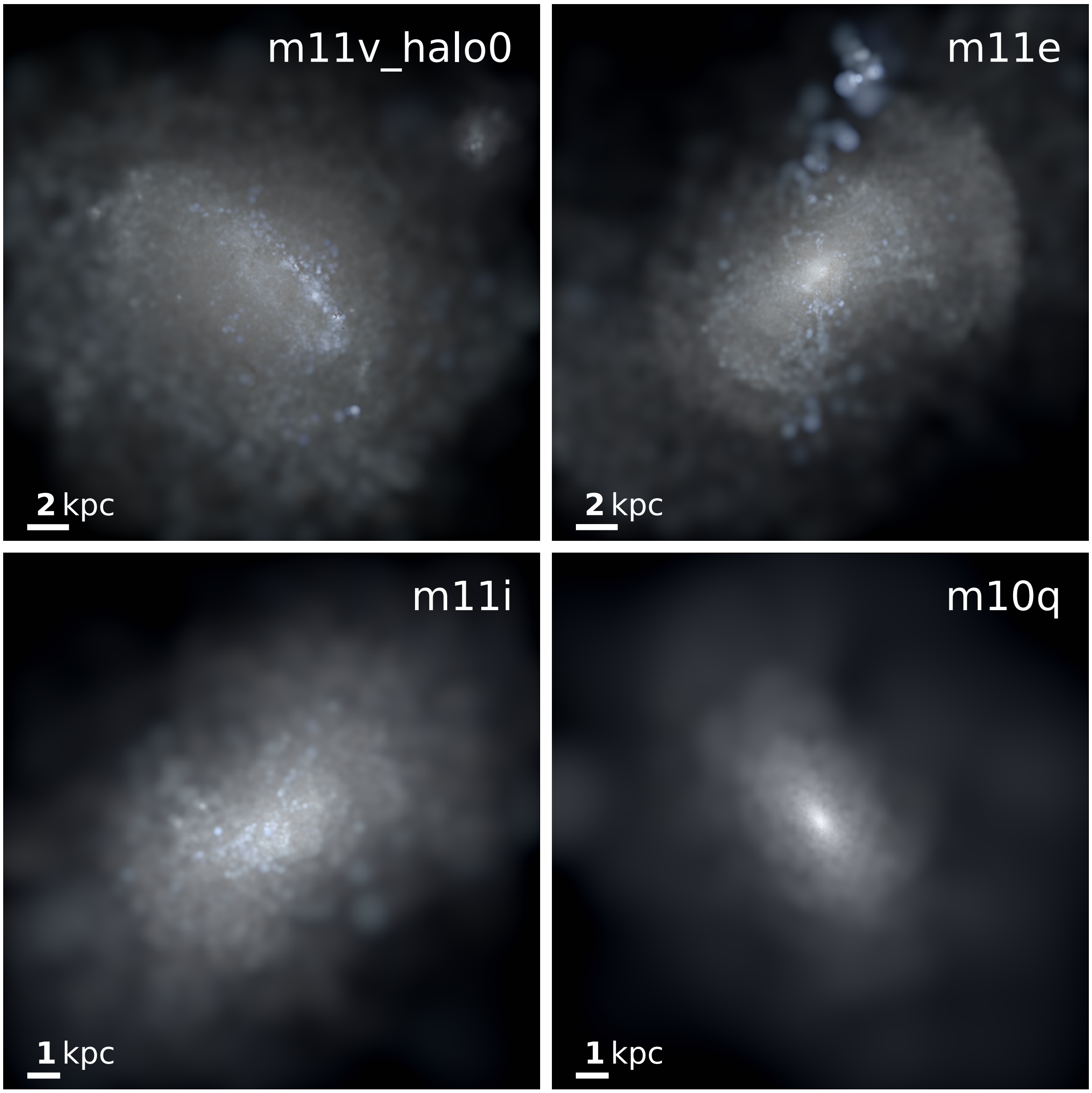

Figure 3.2. Mock images, same as Fig. 3.1, of our irregular dwarf galaxies. **m11v_halo0**: An LMC-mass galaxy that evolved in isolation for a majority of its life and experienced a recent burst in star formation. **m11e**: An irregular dwarf galaxy that spent most of its life as a compact dwarf, similar to the SMC in mass, until it experienced a recent major merger producing prominent stellar shells. **m11i**: A sub-SMC-mass galaxy that experienced multiple merger events and a bursty star formation history that has successively stripped gas from the galaxy. **m10q**: A low-mass dwarf galaxy that evolved in isolation and experienced a major blowout event.

to extremely low D/Z for **m11i** and the complete lack of both dust and gas for **m10q**.

We present the evolution of each galaxy in terms of galactic properties and their dust population, in both composition and amount, in Sec. 3.4.1. We then compare our simulations to present-day observations, focusing on gas-phase element depletions in Sec. 3.4.2 and galaxy-integrated and spatially-resolved IR dust emission in Sec. 3.4.3.

3.4.1 Cosmic Evolution

Galactic Properties

In Fig. 3.3, we show the evolution of various properties for each galaxy, specifically total gas mass, stellar mass, star formation rate (SFR), mass-weighted median gas-phase metallicity, median D/Z, and median Sil-to-C ratio. These values are determined from star particles and gas cells within 10 kpc of the galactic center for all galaxies[9]. Below we briefly describe the evolution of each galaxy in our simulation suite to highlight the variety of evolutionary histories probed.

m12i: A Milky Way-mass compact spiral galaxy that experiences multiple minor mergers throughout its life. At z~0.7 an edge-on minor merger torqued the galactic disk, producing noticeable flared ends to the spiral that persist to the present day. The subsequent infall of pristine, metal-poor gas from this event and the fly-by of two minor satellites produce a minor increase in star formation rate and a minor decrease in galactic metallicity at z~0.2.

m11v_halo0 and m11v_halo2: Two LMC-mass galaxies within the same zoom-in box, which evolve in isolation for the majority of their lives. By $z = 0$ they are on a collision course, with their galactic centers ~70 kpc apart. Despite their similar stellar/gas masses and evolutionary history, **m11v_halo2** has a disky shape with faint spirals while **m11v_halo0** has an elongated shape.

[9]We avoid using $0.1R_{\rm vir}$, or any other evolving radius, as our cutoff when determining galactic properties in order to avoid jumps in $R_{\rm vir}$ due to merger events. A radius of 10 kpc encompasses the ISM of each galaxy while not including a sizable fraction of the galactic halo, which is sufficient for our focus on interstellar dust.

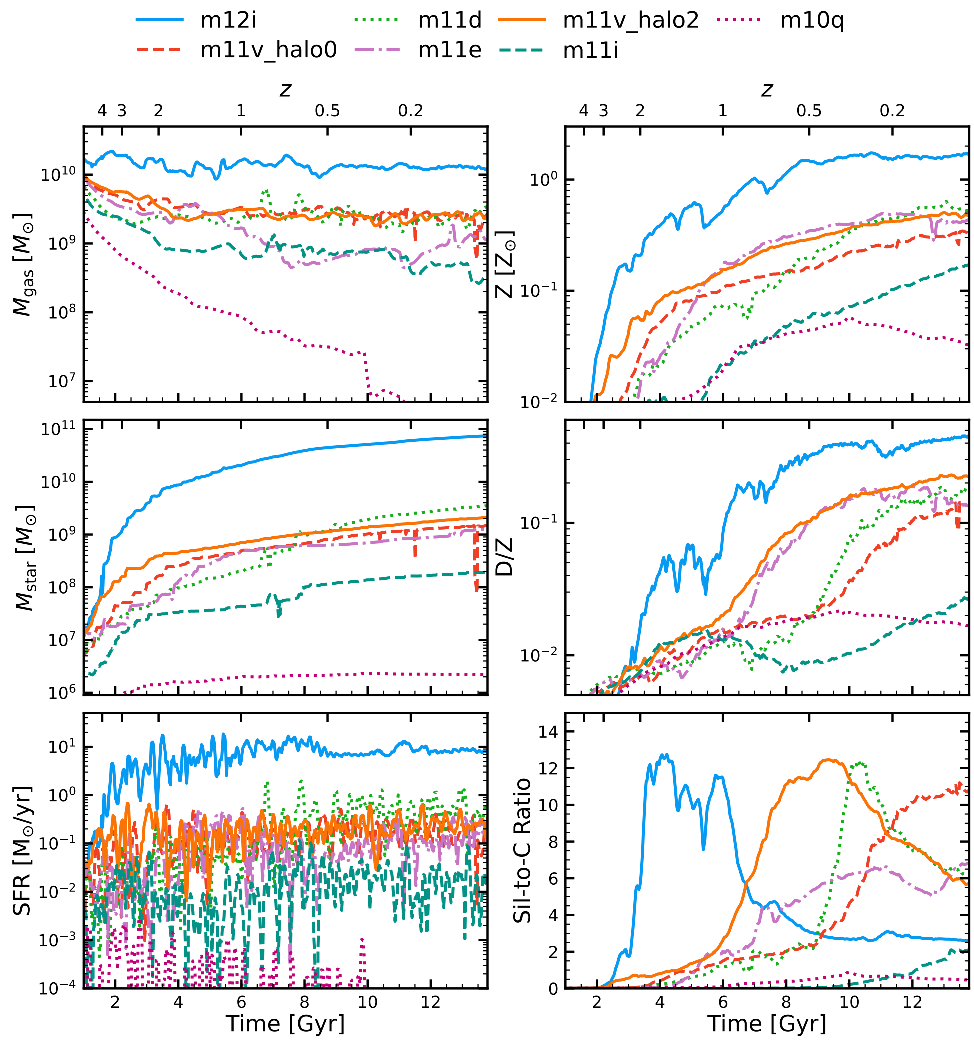

Figure 3.3. Evolution of total galactic gas, stellar, and dust properties for our simulated galaxies for all gas/stars within 10 kpc of the galactic center. Specifically, total gas mass (*top left*), median gas metallicity (*top right*), total stellar mass (*middle left*), median D/Z ratio (*middle right*), star formation rate averaged in 10 Myr intervals (*bottom left*), and median silicate-to-carbonaceous dust mass ratio (*bottom right*). Our simulation suite covers a wide range of evolutionary histories, star formation rates, and metallicities. However, the resulting dust population evolution is relatively similar for all galaxies. Initially, the dust population is dominated by carbonaceous dust produced by SNe II, and later AGB stars, which results in a low D/Z~0.01 and Sil-to-C~0. Eventually, gas-dust accretion becomes efficient for first metallic iron dust, then silicates, and finally carbonaceous dust. The largest increase in D/Z occurs when silicate dust grows efficiently, as can be seen by the rapid increase in Sil-to-C due to silicates dominating the dust mass. When carbonaceous dust begins to grow efficiently, Sil-to-C correspondingly decreases and eventually settles at the typical MW value of ~3. Note that **m10q** experiences a complete blowout event at ~10 Gyr, evacuating almost all gas and dust from the galaxy.

m11d: A bursty LMC-mass galaxy that experiences several merger events before z~0.5, producing a thick disk with sizable voids.

m11e: A compact dwarf galaxy that evolves in isolation for most of its life similar in mass to the SMC. At z~0.1 it experiences a major merger, producing prominent stellar shells and an elongated shape.

m11i: A dwarf/SMC-mass galaxy that experiences a fly-by and major merger from z~0.8−0.5, generating numerous blow-out events. It then evolves in isolation to the present day, experiencing bursty star formation, which successively strips away gas.

m10q: A low-mass dwarf galaxy that evolves in isolation for the majority of its life. Its bursty star formation slowly expels gas until a final starburst at z~0.4 permanently blows out all gas and dust from the galaxy.

Dust Population

In Fig. 3.4 & 3.5 we show a detailed breakdown of each galaxy's metal and dust population evolution, including the mass-weighted gas cell median metallicity, median D/Z, dust creation source contribution, and dust species composition for all gas within 10 kpc of the galactic center. We also include the breakdown for each gas phase: cold neutral gas ($T < 10^3$ K), warm neutral gas (10^3 K $\leq T < 10^4$ K), and warm/hot ionized gas ($T \geq 10^4$ K). While the evolution of each galaxy varies considerably, their dust populations follow similar evolutionary trends which we describe below.

1. SNe-Dominated: Initially, as the first massive stars die, SNe II are the dominant producer of dust mass. This 'stardust' population is dominated by carbonaceous dust, arising from the high SNe II carbonaceous dust production efficiency adopted in our model ($\delta^{\rm SNII}_{\rm carb}$=15%). This produces an extremely low median D/Z~0.01.

2. AGB-Dominated: As stellar populations age and low-mass stars transition to the AGB phase, dust production by AGB stars becomes a sizable component of the dust mass. However, this only dominates the dust population for the lowest-mass dwarf galaxies, which have little

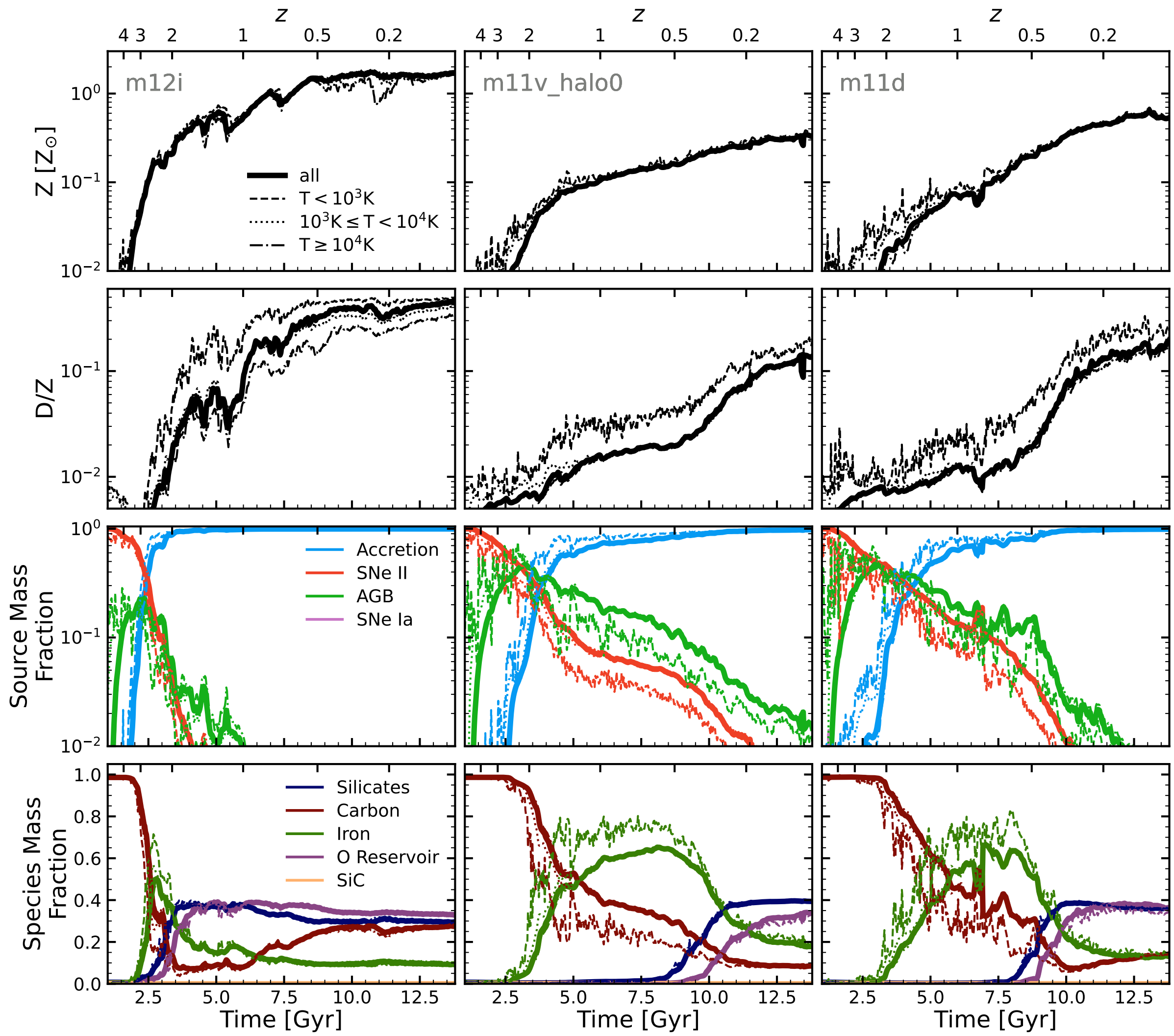

Figure 3.4. Time evolution of metallicity (*top*), D/Z (*second from top*), dust creation source mass fraction (*second from bottom*), and dust species mass fraction (*bottom*) for **m12i** (*left*), **m11v_halo0** (*middle*), and **m11d** (*right*). Median values are given for all gas within 10 kpc of the galactic halo (*solid*), cold gas (*dashed*), warm neutral gas (*dotted*), and warm/hot ionized gas (*dash-dotted*). The dust population of all galaxies is initially dominated by carbonaceous dust from SNe II stars, but this produces an extremely low D/Z. Carbonaceous dust from AGB stars eventually takes over as the dominant dust creation source as long as accretion remains inefficient due to low galactic metallicity, but D/Z changes little compared to the SNe II stardust-dominated population. If the galactic metallicity passes a critical threshold, accretion becomes efficient, becoming the dominant dust creation source and increasing the median D/Z in cool, dense gas. The onset of rapid growth via accretion for metallic iron, silicates, and carbonaceous dust species can be seen in the rapid increase of their corresponding species mass fraction. Overall, the growth of silicate dust via accretion produces the largest change in median D/Z.

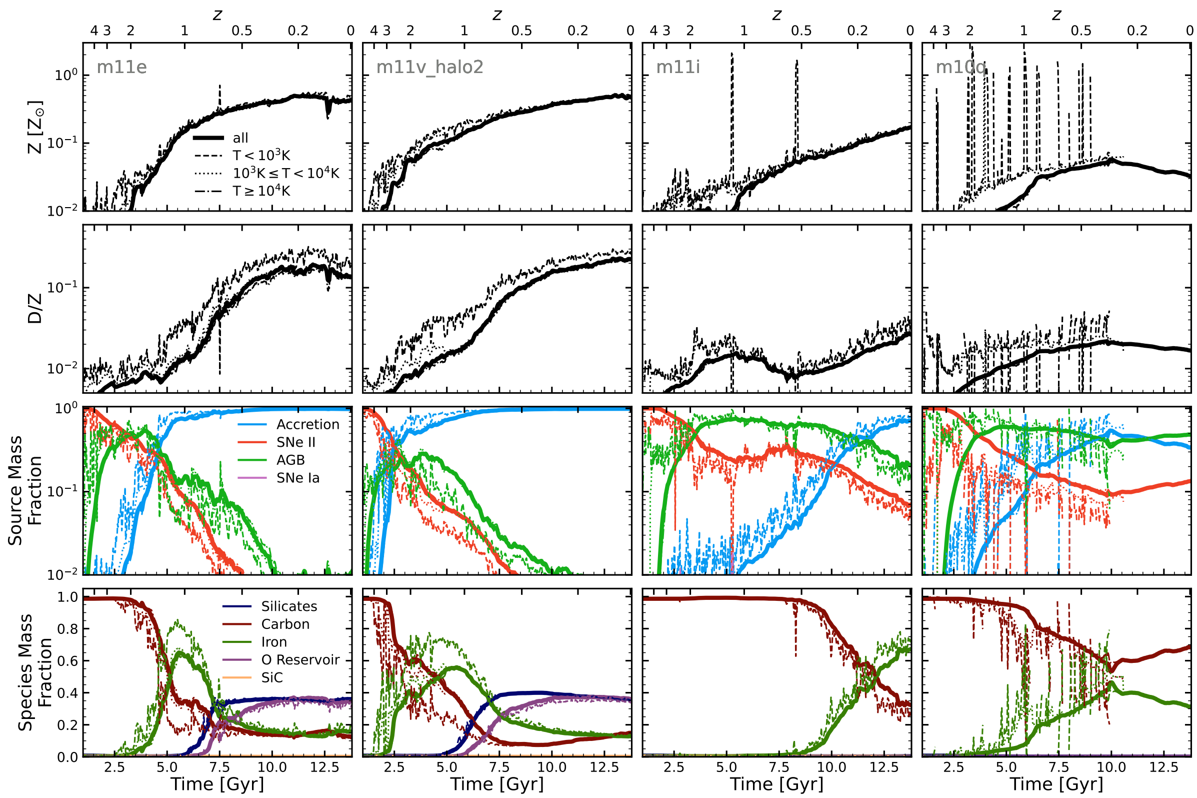

Figure 3.5. Same as Fig. 3.4 for **m11e** (*left*), **m11v_halo2** (*middle left*), and **m11i** (*middle right*) and **m10q** (*right*). Note that bursty star formation in the low-mass dwarf galaxies evacuates a majority of their cold gas which produces sudden increases in Z and decreases in dust for only cold gas.

or extremely late dust growth via accretion. For our model, low metallicity AGB stars produce primarily carbonaceous dust and only x2-3 more dust than SNe II over the lifetime of a stellar population (see Fig. 2 in C22). For these reasons, the median D/Z and dust composition exhibit little change between SNe and AGB-dominated dust regimes.

3. Onset of Accretion: Once the gas within a galaxy reaches a 'critical' metallicity threshold (i.e. key element number abundance), dust growth via gas-dust accretion becomes more efficient than dust destruction by SNe shocks. The exact 'critical' metallicity varies between dust species (metallic iron, silicates, carbonaceous) due to differences in their key element abundances, physical properties, and life cycle processes, which we discuss in Sec. 3.5.1. Metallic iron is the first dust species to grow efficiently via accretion, then silicates, and last carbonaceous dust. Each successively increases the median D/Z, up to D/Z~0.02, ~0.2, and ~0.3 respectively.

4. Build Up & Equilibrium: Once a dust species begins to grow efficiently via accretion, its dust mass builds up over time until an equilibrium is reached, which we discuss in Sec. 3.5.2. Once all dust species grow via accretion, the dust population of the galaxy reaches saturation, with the maximum amount of each dust species effectively forming. This produces an equilibrium dust population similar in composition to the Milky Way (D/Z~0.4 and Sil-to-C~3:1) and is relatively constant over time.

To gauge the accuracy of this predicted trend in dust population evolution, we must compare to observations of galactic dust population amount and chemical composition and observed dust population variability within galaxies.

3.4.2 Element Depletions & Aggregate D/Z

Element depletions provide a detailed accounting for how much of each element is locked in dust and are a strong constraint for our model. Observationally, element depletions are measured using detailed UV spectral absorption features from sight lines to bright standard candles, usually O/B type stars or quasars. Sight line column densities for ionized refractory elements and neutral hydrogen are determined from fits to their absorption profiles, and relative abundances between each element and hydrogen are determined. These relative abundances are then compared to known reference abundances and any missing elements from the gas-phase are then assumed to be locked in dust. The gas-phase depletion of element X is represented logarithmically as

$$\left[\frac{\mathrm{X}}{\mathrm{H}}\right]_{\mathrm{gas}} = \log\left(\frac{N_{\mathrm{X}}}{N_{\mathrm{H}}}\right)_{\mathrm{gas}} - \log\left(\frac{N_{\mathrm{X}}}{N_{\mathrm{H}}}\right)_{\mathrm{ref}}, \tag{3.1}$$

and linearly as

$$\delta_{\mathrm{X}} = 10^{[\mathrm{X}/\mathrm{H}]_{\mathrm{gas}}}, \tag{3.2}$$

where N_{X} and N_{H} are the gas-phase column density of element X and column density of neutral hydrogen ($N_{\mathrm{H,neutral}} = N_{\mathrm{H\,I}} + 2N_{\mathrm{H_2}}$) respectively and $(N_{\mathrm{X}}/N_{\mathrm{H}})_{\mathrm{ref}}$ is the assumed reference abundance.

Due to the high resolution needed for such observations, they are mainly limited to Milky Way, LMC, and SMC[10]. Observations of Milky Way depletions compiled by Jenkins (2009) show C, O, Mg, Si, and Fe depletion increases with increasing H column density. Mg, Si, and Fe depletion observations in the LMC (Roman-Duval et al., 2021) and SMC (Jenkins & Wallerstein, 2017) show similar trends to those in the MW but offset correlating with the relative differences in metallicity between the galaxies (Roman-Duval et al., 2022a). However, direct observations of C and O depletions are limited only to the Milky Way due to either saturated or extremely weak absorption lines, so C and O depletion trends for the SMC and LMC are usually inferred from the MW relation between Fe and C or O depletions respectively (Roman-Duval et al., 2022a,b).

To compare directly to these observations, we created a set of sight lines for each galaxy that originate from young star particles (formed within <10 Myr). For **m12i**, the sight lines terminate within the galactic disk at a distance of $0.1-2$ kpc from the star to simulate depletion observations within the Milky Way. For the dwarf galaxies (**m11v_halo2**, **m11d**,

[10]Element depletions have been observed for damped Lyα systems (DLAs) via quasar absorption lines (Péroux & Howk, 2020). However, DLAs probe a variety of systems (Prochaska & Wolfe, 1997; Wolfe et al., 2005; Faucher-Giguère & Kereš, 2011; Rhodin et al., 2019) and their reference abundances can be difficult to determine due to dust depletions (Roman-Duval et al., 2022b). For these reasons, we forgo comparing to DLA depletion observations.

m11e, **m11v_halo0**, and **m11i**), the sight lines terminate ~50 kpc outside the galaxy to simulate observations of the LMC and SMC. For each sight line we then calculated $N_{\rm H,neutral}$ and C, O, Mg, Si, and Fe depletions. The specifics of our sight line methodology are described in detail in Appendix 3.A. We binned these sight lines in logarithmic $N_{\rm H,neutral}$ bins and calculated the median values and 16-/84-percentiles for C, O, Mg, Si, and Fe depletions. The resulting relation between sight line element depletion and $N_{\rm H,neutral}$ for each element can be seen in Fig. 3.6 for each galaxy. We include the 243 observed Milky Way sight line depletions from Jenkins (2009) and the carbon depletions from Parvathi et al. (2012), the 32 sight line depletions of the LMC from Roman-Duval et al. (2022a), and the 18 sight line depletions of the SMC from Jenkins & Wallerstein (2017). We modify the carbon depletions from Jenkins (2009) and Parvathi et al. (2012) similar to Sec. 3.2.1 in C22 to correct for differences in depletion estimates determined from strong and weak C II transition lines and total C abundances.

We can also directly measure the depletion for each element as a function of physical gas density $n_{\rm H,neutral}$ since our simulations track the total abundance of each element locked in dust for all gas cells. This is valuable for understanding sight line depletions since individual sight lines probe various gas phases and sight lines with similar $N_{\rm H,neutral}$ can probe vastly different gas environments. We therefore bin the gas cells in logarithmic neutral gas density and calculate the median values and 16-/84-percentiles for C, O, Mg, Si, and Fe depletions. The resulting relation for each element depletion and neutral gas density, $n_{\rm H,neutral}$, is shown in Fig. 3.7 for each galaxy. We also include fits to the sight line depletion trends in the Milky Way from Jenkins (2009) assuming mean sight line density is the physical density as a lower bound, and using Zhukovska et al. (2016, 2018) mean sight line density to physical density fit (see C22 Sec. 3.2.2 for details).

O, C, Mg, Si, and Fe show similar depletion trends for all galaxies, transitioning from a shallow to steep slope with increasing density ($N_{\rm H,neutral}$ and $n_{\rm H,neutral}$) similar to observations. This is due to the cycling of gas into cold, dense regions, where metallic iron, silicates, and/or carbonaceous dust grow via gas-dust accretion, and out to hot, diffuse regions where all species are destroyed via sputtering and SNe shocks similar to the results found in C22 for an idealized MW. The trends for C and Mg, in particular, flatten at high density ($n_{\rm H,neutral} > 10^2\,{\rm cm}^{-3}$; not visible at high $N_{\rm H,neutral}$) for all galaxies but for different reasons. C depletions flatten due to our sub-resolution dense molecular cloud prescription. This prescription assumes gas-phase C is rapidly converted to CO in dense molecular gas, halting carbon dust growth. Mg depletions flatten due to the relative abundances of Si and Mg and silicate dust being the only depletion source of Mg in our model. Si is the key element for silicate dust for all galaxies, so there will always be some leftover gas-phase Mg once the maximum amount of silicate dust has formed[11].

Comparing predicted trends between galaxies, all depletions exhibit a staggered offset from one another. These offsets roughly correlate with each galaxy's median gas-phase metallicity, with **m11i** having the weakest and **m12i** having the strongest depletion trends, similar to what is seen in the MW, LMC, and SMC. These offsets are caused by differences in the average gas-dust accretion rate for each galaxy, which scales with gas-phase metallicity (see Eq.20 in C22). Galaxies with higher average gas-phase metallicity will have higher gas-dust accretion rates in dense environments and, therefore, stronger element depletions in these environments. C depletion trends exhibit the largest offset between galaxies and decreasing slopes at high densities. This decrease is so dramatic that only **m12i**, **m11d**, and **m11v_halo2** produce noticeable increases in depletion with increasing density while **m11e**, **m11v_halo2**, and **m11i** have entirely flat relations. This is due to the turn-off of efficient carbonaceous dust growth via accretion. Galaxies with metallicities below a 'critical' metallicity threshold needed for efficient carbonaceous dust growth will produce flat depletion relations set by the creation of dust in SNe and AGB winds. This can also be seen in the flat O, Mg, and Si depletion relations for **m11i** due to the lack of silicate dust growth via accretion.

We further aggregate the element depletions into total D/Z to determine the resulting

[11]We note that the simulations presented in C22 predicted that Mg is the key element for silicates. This was due to the idealized nature of the simulations, whose initial conditions assumed uniform gas and stellar metallicities of Z=$Z_\odot$ and a uniform stellar age distribution over 13.8 Gyr. The metal abundances arising from such a simulation are invariably different from those produced by a realistic stellar population successively built over the age of the universe.

distribution of D/Z with $n_{\mathrm{H,neutral}}$ and temperature for each galaxy. We binned the gas cells in logarithmic neutral gas density and temperature bins, calculating the median D/Z and 16-/84-percentiles shown in Fig. 3.8. Aggregating the observed Milky Way element depletions, we include an upper bound on the expected D/Z relation with $n_{\mathrm{H,neutral}}$ along with an estimate for the WNM[12] based on depletions from Jenkins (2009). We also include a reasonable estimate of D/Z in dense environments following the relation from Zhukovska et al. (2016, 2018).

The exhibited D/Z relations with $n_{\mathrm{H,neutral}}$ mirror the individual element depletion trends for each galaxy, transitioning from a shallow to steep slope with increasing density and offset from one another in proportion to each galaxy's relative metallicity. This transition is less prominent in **m12i**, but it matches reasonably well with observations of the Milky Way. In regards to temperature, the resulting D/Z relation for all galaxies can be broken into three regimes. **(i) Cool/Warm Gas (T < 10^4K):** As hot gas cools, gas-dust accretion eventually 'turns on' and dust begins to grow, steadily increasing D/Z with decreasing temperature. Our model assumes this 'turn on' point occurs when T<300K, which can be seen as a moderate increase in D/Z. **(ii) Ionized Gas (T = $10^4 - 10^5$ K):** This regime is primarily comprised of gas that has recently experienced SNe feedback, with dust residing in gas cells immediately around the SNe being destroyed. This produces a relatively flat D/Z for all galaxies, which lies at ~40% of the maximum D/Z at low temperatures for each galaxy. This matches surprisingly well with the set dust destruction efficiency of $\bar{\epsilon}\approx 40\%$ assumed for gas shocked to $v_s \geq 100$ km/s in our SNe dust destruction routine. This indicates that, on average, our routine predicts all gas in this regime has been shocked to $v_s \geq 100$ km/s once. However, the large scatter in D/Z indicates this varies considerably between gas cells, with some being shocked multiple times and others not shocked at all. **(iii) Coronal Gas (T > 10^5 K):** Dust destruction via thermal sputtering becomes efficient in this regime, with D/Z rapidly dropping with increasing temperature. For gas with $T \gtrsim 10^6$ K, on average, all dust is destroyed.

[12]To account for the uncertainty in the observed WNM D/Z owing to the lack of measured sight line C depletions in this regime we include error bars representing 80% (assuming 20% in CO) of C or no C in dust.

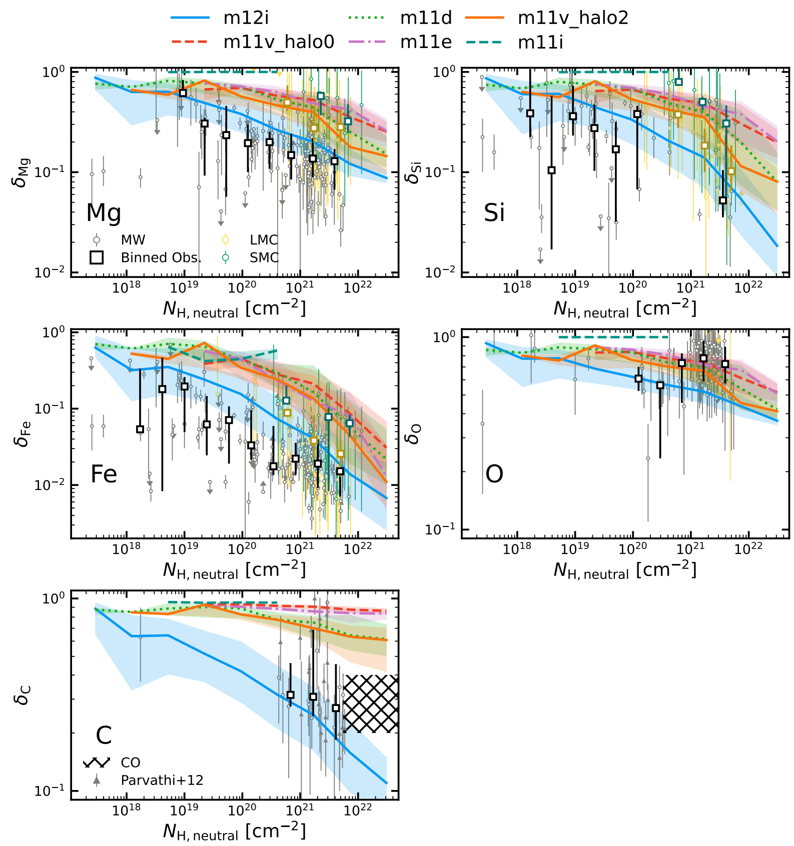

Figure 3.6. Predicted median sight line C, O, Mg, Si, and Fe depletion versus $N_{\mathrm{H,neutral}}$ from in-disk sight lines for **m12i** and face-on sight lines for **m11v_halo0**, **m11d**, **m11e**, **m11v_halo2**, and **m11i** following the sight line methodology outlined in Appendix 3.A. For each, 16-/84-percentile ranges are represented by shaded regions. We compare with observed elemental depletion along sight lines in the Milky Way from Jenkins (2009) (*grey circles*), of the LMC from Roman-Duval et al. (2022a) (*yellow circles*), and of the SMC from Jenkins & Wallerstein (2017) (*teal circles*). For C depletions, we decreased the Jenkins data by a factor of 2 based on observations from Sofia et al. (2011) and Parvathi et al. (2012). We also include 21 sight line observations in the Milky Way from Parvathi et al. (2012) (*triangles*) along with a range of expected maximum depletions in dense environments (*hatched*) based on observations of 20% to 40% of C in CO in the Milky Way (e.g. Irvine et al., 1987; van Dishoeck et al., 1993; van Dishoeck & Blake, 1998; Lacy et al., 1994). We also show the binned median and 16-/84-percentile ranges for each data set (*squares*). All galaxies (besides **m11i**) produce a Mg, Si, Fe, and O relation which transitions from a shallow to steep slope for increasing $N_{\mathrm{H,neutral}}$, but each relation is offset roughly corresponding with each galaxy's median metallicity. The C relations exhibit a weaker transition and a larger offset, with the lowest metallicity galaxies (**m11e**, **m11v_halo0**, and **m11i**) producing a nearly flat relation. This is due to the 'turn-off' of carbonaceous growth via accretion since these galaxies lie below the 'critical' metallicity threshold. **m11i** exhibits flat depletion relations for all but Fe since only metallic iron dust grows efficiently in this galaxy. Overall the predicted trends are a good match with observations, but the lack of C or O depletions outside the Milky Way paints an incomplete picture.

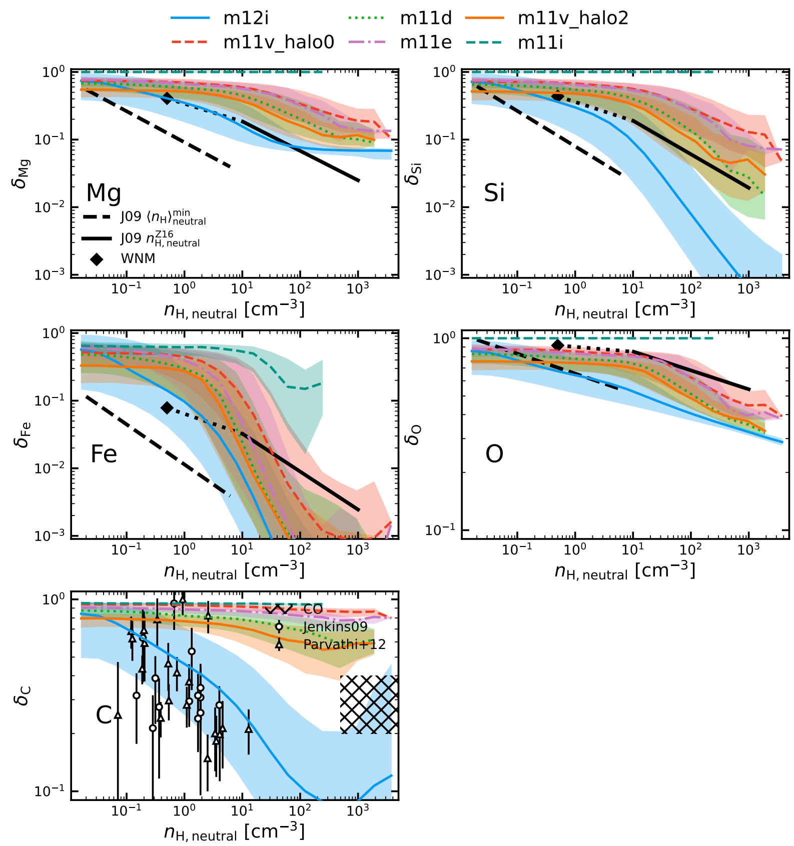

Figure 3.7. Resulting C, O, Mg, Si, and Fe depletion versus $n_{\mathrm{H,neutral}}$ for gas within the 10 kpc of each galaxy at z=0. The 16-/84-percentile ranges are represented for each by shaded regions. We compare with observed elemental depletions in the Milky Way from Jenkins (2009) assuming mean sight line density is the physical density (*black-dashed*), this can be treated as a lower limit, and using Zhukovska et al. (2016, 2018) mean sight line density to physical density fit (*black-solid*). For O, Mg, Si, and Fe we include estimates for the WNM depletions (*diamond*) along with an interpolation to the Jenkins' relation (*black-dotted*). For C we only include the individual sight line depletions from Jenkins (*triangles*) decreased by a factor of 2 based on observations from Sofia et al. (2011) and Parvathi et al. (2012). We also include 21 sight line observations from Parvathi et al. (2012) (*circles*) as another lower bound along with a range of expected minimum depletions in dense environments (*hatched*) based on observations of 20% to 40% of C in CO in the Milky Way. **m12i**, **m11v_halo2**, **m11d**, **m11e** and **m11v_halo0** show similar offset trends for Mg, Si, O, and Fe which transition from a shallow to steep slope for increasing $n_{\mathrm{H,neutral}}$. Mg and C depletions show an additional transition to a flat slope at the highest densities. For Mg, this is due to the saturation of silicate dust, which has run out of available Si to grow further. For C, this is due to the rapid formation of CO, which takes up any remaining gas-phase C. **m11i** only exhibits a slopped trend for Fe since only metallic iron grows efficiently.

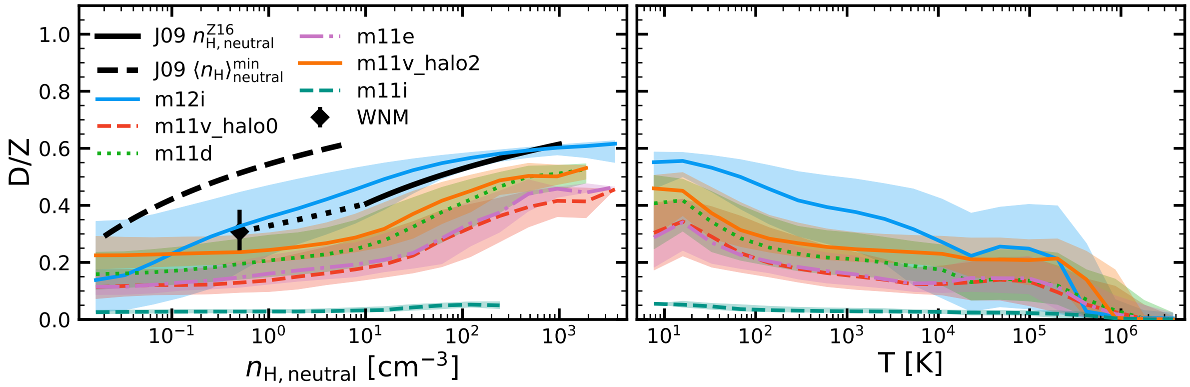

Figure 3.8. Resulting D/Z versus $n_{\mathrm{H,neutral}}$ (*left*) and temperature (*right*) for gas within 10 kpc for each galaxies at z=0. All galaxies with efficient dust growth via accretion produce a sloped relation which increases with increasing $n_{\mathrm{H,neutral}}$ and decreasing temperature. All galaxies with efficient silicate growth via accretion also have sizable D/Z even in low density, hot gas ($T>10^4$ K or $n_{\mathrm{H,neutral}}<1\,\mathrm{cm}^{-3}$), which is exposed to SNe shocks. For gas with $T>10^5$K, D/Z quickly drops due to the onset of efficient dust destruction via thermal sputtering.

3.4.3 Extragalactic Dust Emission

Direct measurement of element depletions in galaxies beyond the Milky Way and its satellites is currently not possible. An alternative method to probe galactic dust populations is through the combination of multi-wavelength estimates of dust mass, gas mass, and metallicity. This method infers a total dust mass by fitting dust emission models to observed dust emission spectra. The assumed dust model can vary in complexity from a simple modified black body to physical dust models with specific dust grain sizes and chemical compositions, affecting the total dust mass inferred (Chastenet et al., 2021). This method was first used in galaxy-integrated D/Z studies by Rémy-Ruyer et al. (2014) who studied 126 local galaxies, including dwarf, spiral, and irregular type galaxies, covering a large metallicity range ($12+\log_{10}(\mathrm{O/H})$=7.1−9.1; $Z\approx0.02-2.3\mathrm{Z}_\odot$). De Vis et al. (2019) further expanded upon this sample, adding ~500 local DustPedia galaxies, which cover a more limited metallicity range ($12+\log_{10}(\mathrm{O/H})$=7.9−8.7; $Z\approx0.15-0.9\mathrm{Z}_\odot$) and are mainly limited to spiral galaxies. Chiang (2021); Chiang et al. (2021, 2023) extended this method to ~2 kpc spatially-resolved studies of individual galaxies, compiling spatially resolved relations between D/Z and local environments for 46 nearby galaxies. Their sample is limited to primarily spiral galaxies with $M_{\rm star} > 10^9 \rm M_\odot$ and $12+\log_{10}(\rm O/H) \gtrsim 8.4$ ($Z \gtrsim 0.5 \rm Z_\odot$). Recently, (Clark et al., 2023) utilized this method with improved Herschel data to produce high resolution (14-144 pc) maps of dust-to-neutral-gas ($\rm D/H_{neutral}$) ratios for Local Group galaxies (LMC, SMC, M33, and M31).

Galaxy-Integrated D/Z

We first show the resulting evolution between galaxy-integrated D/Z and metallicity for each simulated galaxy in Fig. 3.9, plotting D/Z and $12+\log_{10}(\rm O/H)$ in 1 Gyr intervals from ~3 Gyr to present day. We compare against the galaxy-integrated observations from Rémy-Ruyer et al. (2014) and De Vis et al. (2019)[13] along with their fitted relations. We define the galaxy-integrated D/Z as the median D/Z for cool, neutral (T<1000 K) gas, following the assumption that galaxy-integrated dust emission studies primarily probe dense environments. In particular, Aniano et al. (2012, 2020) directly compared observations of spatially-resolved and galaxy-integrated dust emission SEDs for individual galaxies and found that a majority of galaxy-integrated dust emission is produced by dust in dense regions exposed to diffuse radiation fields. Chiang et al. (2021, 2023) also found that regions with good SNR (high dust emission) correlate with regions of CO detection (molecular gas), which further supports this assumption. We define the galaxy-integrated metallicity as the median $12+\log_{10}(\rm O/H)$ for gas with $7000<T<15000$ and $n_{\rm H}>0.5\rm cm^{-3}$ to match the properties of nebular regions typically probed by empirical strong emission line methods used in these studies (e.g. Pilyugin & Grebel, 2016). We also account for the depletion of O into dust by only considering gas-phase O instead of total (gas+dust) O abundance and include a -0.2 offset to correct for differences in reference O abundances assumed in our simulations (Anders & Grevesse, 1989) and observations (Asplund et al., 2009). We investigate other definitions of $12+\log_{10}(\rm O/H)$ in Appendix 3.B and find that accounting for only gas-phase O has the largest effect but only produces an offset of $\lesssim$0.2 primarily for high values of $12+\log_{10}(\rm O/H)$. However, this depends entirely on our model's

[13] De Vis et al. (2019) uniquely defines $\rm D/Z=\Sigma_{dust}/(\Sigma_{dust}+\Sigma_{metals})$ to account for possible depletion of metals into dust.

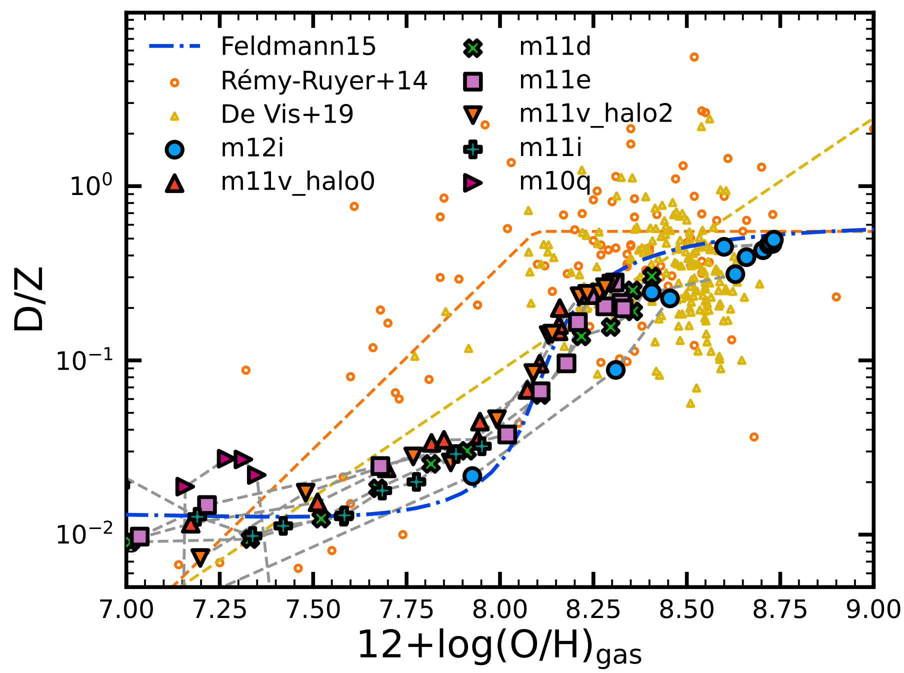

Figure 3.9. Resulting relation between galaxy integrated D/Z and metallicity for our galaxies over time. Each connected point is +1 Gyr apart in time, starting at ~3 Gyr up to present day. The galaxy-integrated D/Z is set as the median D/Z for cool, neutral ($T < 1000$ K) gas, similar to the type of environments probed by observations of dust SEDs. The metallicity is set as the median gas-phase oxygen abundance (only O not depleted into dust) for gas with $7000 < T < 15000$ and $n_{\rm H} > 0.5$ cm^{-3}, similar to regions probed by nebular emission lines used in galactic observations. $12 + \log_{10}({\rm O/H})$ is also offset by -0.2 to account for the differences in assumed oxygen abundances between Anders & Grevesse (1989) and Asplund et al. (2009). We compare with galaxy-integrated observations of local galaxies from Rémy-Ruyer et al. (2014) (*orange circles*) and De Vis et al. (2019) (*gold triangles*), along with the fits presented in both studies (*dashed lines*). We also include predictions from the equilibrium chemical and dust model from Feldmann (2015) (*blue dash-dotted*). All galaxies start with low D/Z and Z, being dominated by stardust production. For galaxies that surpass $12 + \log_{10}({\rm O/H}) {\sim} 8$, D/Z rises steeply due to the onset of efficient silicate, and later carbonaceous, dust growth via accretion. The differences in the steepness of this relation are due to the time it takes for the dust population to build up through successive cycling of gas into and out of cold, dense clouds. **m12i** also experiences a temporary decrease in the metallicity due to a minor merger which decreases the median metallicity of warm gas as seen in Fig. 3.4.

prescription for O depletion into dust. We also include the predicted relation between D/Z and metallicity from the equilibrium chemical and dust analytical model presented in Feldmann (2015), which tracks the evolution of a single, chemically-ambiguous dust species and accounts for stardust production, dust growth in the ISM, dust destruction by SNe shocks, and dust dilution by inflowing, pristine gas. We specifically plot the results from their model with slight adjustments to their fiducial parameters. We set the maximum depletion limit for all metals to $f^{\rm dep} = 0.6$ to match the maximum D/Z predicted by our model. We modify the dust injection via AGB stars and SNe II of a stellar population to $y_{\rm D} = 2\times10^{-3}$ to match our typical D/Z for stardust dominated galaxies. Finally, we set the ratio between the molecular gas depletion by star formation timescale and the dust growth via accretion timescale to $\gamma = 1.3\times10^{4}$ to match our model's predicted rapid increase in D/Z above a critical metallicity threshold.

At low metallicity, all of our galaxies exhibit similar D/Z relations. These galaxies are dominated by stardust production, which yields very low D/Z$\sim10^{-2}$ that is roughly constant with respect to metallicity. Metallic iron dust growth becomes efficient for galaxies above $12+\log_{10}({\rm O/H})\sim7.6$, increasing D/Z by roughly a factor of two. Above $12+\log_{10}({\rm O/H})>7.9$, the relations begin to diverge due to the onset of efficient silicate and later carbonaceous dust growth. Some galaxies (**m11v_halo2** and **m11v_halo0**) follow the predicted equilibrium relation from Feldmann (2015) to surprising accuracy. Others (**m12i**, **m11d**, and **m11e**) fall below this relation to varying degrees and at different metallicities, producing a maximum scatter in D/Z of ~0.5 dex at $12+\log_{10}({\rm O/H})\sim8.3$. These varying relations are caused by delays in the buildup of dust mass once gas-dust accretion becomes efficient, which we discuss in Sec. 3.5.2. At high metallicity, the relations begin to reconverge onto the equilibrium track where D/Z saturates at ~0.4. At these metallicities, dust growth is so strong that a majority of all refractory elements have been locked into dust. Another interesting feature is the apparent 'backslides' in metallicity shown by **m12i**. These correspond to flyby and merger events which cause the infall of low metallicity gas. This infalling gas decreases the metallicity of warm/hot gas, as can be seen in Fig. 3.4, including the nebular gas we use for our $12+\log_{10}({\rm O/H})$ definition. Even with our

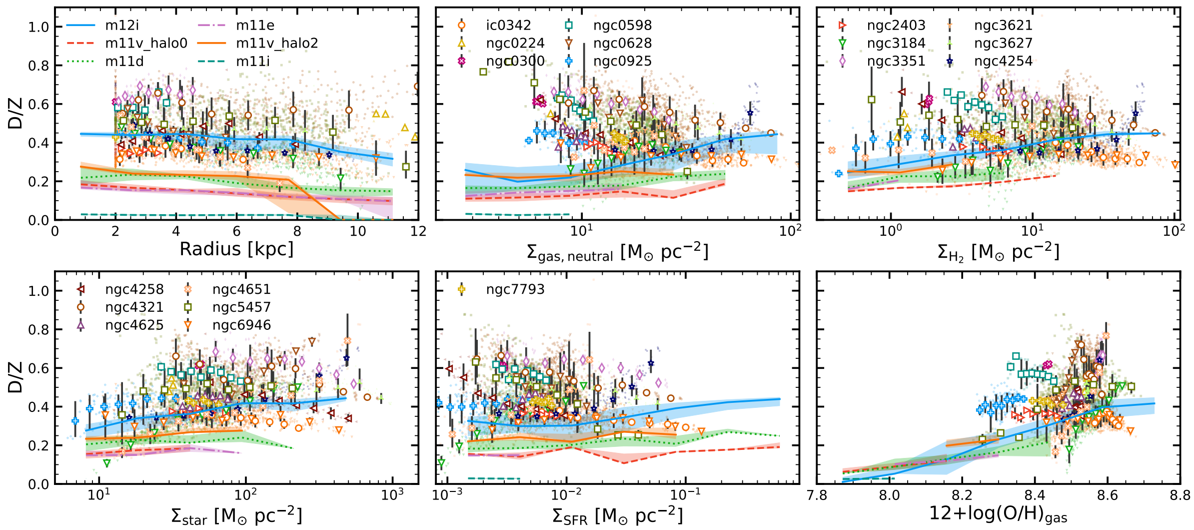

Figure 3.10. Relation between median D/Z ratio and galactocentric radius (*top left*), neutral gas surface density (*top middle*), molecular gas surface density (*top right*), stellar surface density (*bottom left*), star formation rate surface density (*bottom middle*), gas-phase oxygen abundance (*bottom right*) in 2 kpc bins for our galaxies at $z = 0$. We compare with dust emission-based observations of spatially-resolved D/Z of local galaxies from Chiang et al. (2023), which is an extension of the technique used in Chiang et al. (2021), with 2 kpc resolution and $\alpha_{\rm CO}^{\rm B13}$ conversion factor. All of our simulated galaxies produce a weakly slopped D/Z relation, which decreases with galactocentric radius and increases with density and metallicity. **m12i** falls near the middle of, and the dwarf galaxies fall at the bottom or below the observed range for all galactic properties, but this is not unexpected since the observed sample includes only one dwarf galaxy. Our results disagree with the observed relations for $\Sigma_{\rm gas,neutral}$ and $\Sigma_{\rm H_2}$, which suggest D/Z decreases in denser environments. However, these observations disagree with high-resolution observations (Clark et al., 2023), so this may be due to resolution effects.

small sample of galaxies, we are able to recreate a reasonable amount of the scatter in D/Z for certain metallicities, which could explain some of the observed scatter[14]. However, compared to the observed sample from Rémy-Ruyer et al. (2014), our relations appear to be shifted to higher metallicity, indicating our 'critical' metallicities may be too high.

Spatially-Resolved D/Z and D/H

We further compare our simulations at z=0 to the spatially resolved observations of Chiang et al. (2023) in Fig. 3.10, examining the relation between D/Z and galactocentric radius,

[14]This scatter is partly due to observational effects, such as how a single galactic metallicity is assigned for galaxies which have radial metallicity gradients, which can result in unphysical D/Z>1.

neutral gas surface density ($\Sigma_{\rm gas,neutral}$), molecular gas surface density ($\Sigma_{\rm H_2}$), stellar surface density ($\Sigma_{\rm star}$), star formation rate surface density ($\Sigma_{\rm SFR}$), and $12+\log_{10}(\rm O/H)_{gas}$[15]. We limit our comparison to the 17 galaxies in their 2 kpc resolution sample that have direct metallicity measurements and the derived D/Z values using the Bolatto et al. (2013) $\alpha_{\rm CO}$ prescription ($\alpha_{\rm CO}^{\rm B13}$), which Chiang et al. (2021) argued yields the most reasonable D/Z. To match the observational resolution, we bin each simulation in 2 kpc face-on square pixels and calculate $\rm D/Z = \Sigma_{dust}/\Sigma_{metals}$ for each pixel. We then bin these pixels across each property and calculate the median D/Z values and 16-/84 percentiles for each[16].

All galaxies produce a weakly slopped relation between D/Z and all galactic properties. Specifically, increasing D/Z with decreasing galactocentric radius and increasing density and metallicity. All relations are roughly offset downwards by each galaxy's relative metallicity, besides the relation between D/Z and $12+\log_{10}(\rm O/H)$, which suggest all galaxies follow the same trend across their respective metallicity ranges. Compared to observations, **m12i** falls near the middle of the observed range for all galactic properties. The dwarf galaxies fall either at the bottom or below the range of observations, but the observational sample includes only one dwarf galaxy (M33/NGC598), so this is not unexpected. What is unexpected is the observed trends of decreasing D/Z with increasing $\Sigma_{\rm gas,neutral}$ and $\Sigma_{\rm H_2}$ for many galaxies in the observational sample, which none of our simulations produce. However, these trends are in stark contrast to our current understanding that dust growth rates increase in denser environments. They also disagree with high-resolution dust emission observations from Clark et al. (2023), so this may be due to resolution effects.

We similarly compare our simulations to high-resolution observations of dust-to-neutral-gas mass ($\rm D/H_{neutral} = \Sigma_{dust}/\Sigma_{HI+H_2}$) for Local Group galaxies from Clark et al. (2023) in Fig. 3.11. We utilize the same face-on projection technique outlined above but with two different pixel sizes

[15]The spatially-resolved O abundances follow the same definition as defined for galaxy-integrated O abundances.

[16]While the observations from Chiang et al. (2023) primarily probe H_2-dominated regions (employ a minimum $I_{\rm CO}$ detection threshold), we do not include a molecular gas mass fraction ($f_{\rm H_2}$) cutoff for simulated pixels. We find that including such a cutoff has little effect on the resulting relations for **m12i**, primarily truncating the relations at lower surface densities and $12+\log_{10}(\rm O/H)$, but excludes the majority of pixels for our dwarf galaxies.

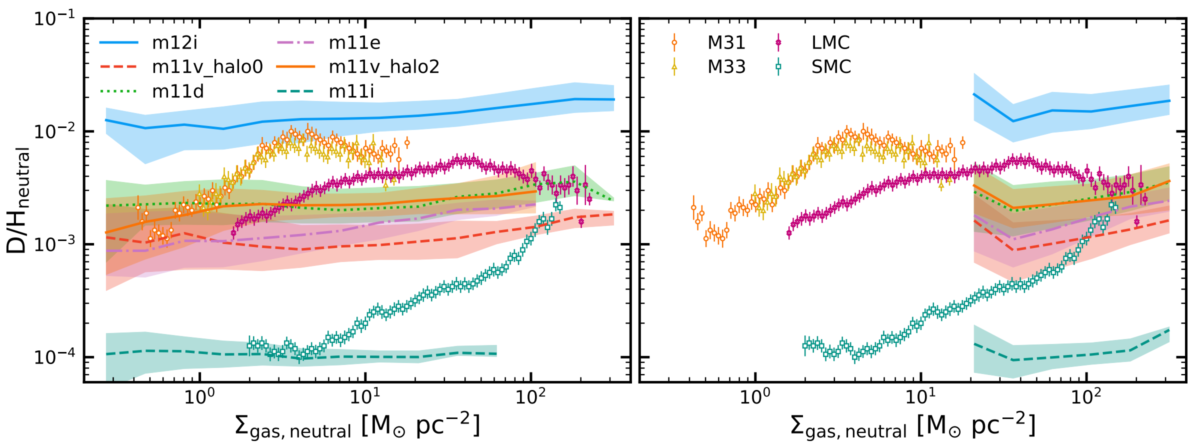

Figure 3.11. Resulting D/H$_{\text{neutral}}$ versus $\Sigma_{\text{gas,neutral}}$ with (*left*) 144 pc resolution pixels and (*right*) 14 pc resolution pixels from face-on projections of each galaxy at $z = 0$. Only pixels with > 50% of neutral gas mass are included since pixels dominated by ionized gas produce artificially high D/H$_{\text{neutral}}$ at low $\Sigma_{\text{gas,neutral}}$. We compare to deprojected 'face-on' observations of M33, M31, LMC, and SMC from Clark et al. (2023), which vary in resolution from 14-144 pc. Note the error bars presented for these observations are the uncertainty of the median and not the scatter. The average standard deviation for D/H$_{\text{neutral}}$ across all galaxies is 0.8 dex, but well-behaved and Gaussian. We also caution that these observations may underpredict D/H$_{\text{neutral}}$, when compared to element depletion observations. Overall, our simulations predict D/H$_{\text{neutral}}$ increases with surface density and match the typical values observed at high $\Sigma_{\text{gas,neutral}}$. However, they underpredict the steepness of this relation, suggesting our SNe dust destruction prescription may be too weak.

(14 and 140 pc) to match the range of observational resolutions. We also only consider pixels with a neutral gas mass fraction $f_{\rm neutral}$>0.5 to avoid HII-dominated regions that are invisible to this observational technique. Overall our simulations predict D/H$_{\rm neutral}$ increases with surface density for galaxies in which silicate and/or carbonaceous gas-dust accretion is efficient, and match the typical D/H$_{\rm neutral}$ observed at at high $\Sigma_{\rm gas,neutral}$ for all observed galaxies irrespective of resolution[17]. However, the steepness of this relation is under predicted, with D/H$_{\rm neutral}$ only increasing by a factor of $\lesssim$2 in our simulations compared to the >3 factor observed for all galaxies. This suggests that our model's SNe dust destruction prescription is too weak, leaving too much dust in diffuse gas. However, we cannot entirely rule out our model predictions since the observations have an average standard deviation of 0.8 dex across all galaxies. We also note that when compared to the expected D/H$_{\rm neutral}$ trends derived from element depletions (again using inferred C and O depletions), these observations underpredict D/H$_{\rm neutral}$ for the SMC but agree with the LMC. Our simulations also indicate that efficient silicate dust growth may have occurred relatively recently in the SMC, given its extremely steep relation that overlaps with both **m11v_halo0** and **m11i**.

We caution that our approximation of observables begins to break down at these high resolutions. Specifically, individual phases of the ISM are resolved, resulting in pixels that primarily probe diffuse, ionized gas. These pixels have misleadingly high D/H$_{\rm neutral}$ at low neutral surface densities since a majority of dust resides in ionized gas. This produces an upswing in D/H$_{\rm neutral}$ at the lower end of our predicted 14 pc resolution relations and is even more pronounced when we do not include the $f_{\rm neutral}$ > 0.5 cutoff. Whether observations would detect these pixels due to their possibly weak IR emissions is unknown and would require the creation of mock dust SEDs using radiative transfer codes. Due to this complexity, we save a more detailed comparison to spatially-resolved dust emission studies for future work.

[17]The apparent downturn in observed D/H$_{\rm neutral}$ at the highest surface densities for the LMC, M31, and M33 is most likely caused by observational biases and model assumptions, and not a physical decrease in dust in these environments. We point the reader to Appendix B in Clark et al. (2023) for a detailed breakdown of possible culprits.

3.5 Discussion

For all but the most metal-poor galaxies in our simulation suite, gas-dust accretion is the dominant producer of dust mass for a majority of each galaxy's life. Therefore, understanding when gas-dust accretion becomes efficient within a galaxy and when that galaxy's dust population transitions from a low to high D/Z ratio are critical for investigating galactic dust evolution. However, these two transitions have typically been lumped together under the moniker of 'critical' metallicity (e.g. Zhukovska, 2014; Feldmann, 2015). Below we break down these two transitions in our simulations, redefining the meaning of 'critical' metallicity, and investigate their implications for observations.

3.5.1 Efficient Gas-Dust Accretion

The transition to efficient gas-dust accretion for a dust species occurs when, on average, more dust mass is created by accretion in dense regions than is destroyed by destruction processes (SNe, thermal sputtering, astration) or removed from the galaxy by outflows. While this implies that numerous, interwoven processes on both a local and galactic scale determine this transition, in practice, the galaxy-averaged metallicity is found to be the primary determinator. In particular, a 'critical' metallicity threshold has been proposed above which the predicted galactic D/Z rapidly increases due to accretion (e.g. Zhukovska, 2014; Feldmann, 2015; Triani et al., 2020). For our purposes, we define the 'critical' metallicity as the point at which the species mass fraction of a given dust species begins to increase as seen in Fig. 3.4 & 3.5. Using this definition, all of our simulated galaxies show the same 'critical' metallicity threshold, above which the mass of a given dust species begins to increase. They all also indicate that each dust species has its own 'critical' metallicity, with $Z_{\rm crit}{\sim}0.05\mathrm{Z}_{\odot}$ for metallic iron, $Z_{\rm crit}{\sim}0.2\mathrm{Z}_{\odot}$ for silicates, and $Z_{\rm crit}{\sim}0.5\mathrm{Z}_{\odot}$ for carbonaceous dust. Three factors cause these differences in 'critical' metallicity:

(1) Key Elements: For a dust species with a set chemical composition, its accretion rate scales with the number abundance of that species' key element. For metallic iron this is Fe, for silicates this is Si[18], and for carbonaceous this is C. Assuming solar abundances (Anders & Grevesse 1989 or Asplund et al. 2009), C is 10 times more abundant than either Si or Fe. Atomic C is also lighter, so it will have thermal velocities 1.5 and 2.2 times greater than Si and Fe respectively. If we assume dust grows purely from hard-sphere type encounters, and all dust species are the same in all other respects, then carbonaceous dust should grow ~15 times faster than silicates and ~22 times faster than metallic iron dust, which is similar to the predictions of Granato et al. (2021).

(2) Physical Properties: Differences in physical properties between dust species (i.e. grain sizes, geometry, grain charging, sticking efficiency) can alter their effective accretion rates. In particular, our model assumes different average grain sizes ($\langle a \rangle_3$; see Eq. 3 in C22) for each dust species due to differences in grain size distributions and effects of Coulomb enhancement[19] in atomic and diffuse molecular gas. Overall this produces a relative difference in accretion timescales of 1:150:900 in atomic/diffuse molecular gas for metallic iron, silicates, and carbonaceous dust, respectively, and 1:10:10 in dense molecular environments.

(3) Life Cycles: Differences in dust life cycle processes (creation, growth, destruction) between species affect the net change in dust mass during one cycle of a gas parcel into and out of dense regions. For carbonaceous dust, our model accounts for the rapid formation of gas-phase CO in dense molecular environments, which halts dust growth. This decreases the amount of time carbonaceous dust has to grow compared to other dust species. For metallic iron, we assume a fraction of the dust population is locked inside silicate dust as inclusions ($f_{\rm incl} = 0.7$), protecting them from destruction by SNe and thermal sputtering and reducing the amount of dust grain surface area available for accretion.

We caution that the included physics in our dust evolution model are in no way complete and the predicted 'critical' metallicities could change with the incorporation of new physics.

[18]Depending on the relative abundances of Mg and Si, Mg can be the key element for silicates. For our simulations, we find Si is the key element for nearly the entire history of each galaxy.

[19]Coulomb enhancement arises from a grain size dependent electrostatic enhancement factor which accounts for the change in interaction cross section between ionized gas-phase metals and charged dust grains.

However, the predictions of varying critical metallicities between dust species have some support from observations. As shown in Fig. 3.6, the LMC and SMC show large depletions of Si, Mg, and Fe in dense environments, suggesting the efficient growth of silicate and a theoretical iron-bearing dust species which agree with our model. While C depletions are currently unobservable in these galaxies, dust extinction and emission observations show decreasing amounts of small carbonaceous grains and PAHs (Weingartner & Draine, 2001a; Chastenet et al., 2019), suggesting carbonaceous dust growth may not be efficient in such galaxies. A sizable carbonaceous dust population dominated by large grains could exist and be indiscernible by current observational techniques. However, this seems unlikely as it would require carbonaceous grains to be far less prone to shattering into smaller grains compared to other dust species.

3.5.2 Dust Buildup and Equilibrium

Once gas-dust accretion becomes efficient for a given dust species, the dust mass will build through successive cycles of gas into and out of dense environments until it reaches an equilibrium between dust growth and dust destruction via SNe. This can be seen in Fig. 3.3, 3.4, & 3.5 as sharp increases in total D/Z and species mass fraction that eventually plateau. We label the time between the onset of gas-dust accretion and the equilibrium plateau as the 'equilibrium' timescale ($\tau_{\rm equil}$) and find this timescale varies between dust species and between galaxies, with $\tau^{\rm iron}_{\rm equil}{\sim}0.75-4$ Gyr, $\tau^{\rm sil}_{\rm equil}{\sim}1.0-1.5$ Gyr, and $\tau^{\rm carb}_{\rm equil}{\gtrsim}3$ Gyr for metallic iron, silicates, and carbonaceous dust respectively. The variation in $\tau_{\rm equil}$ between dust species is due to the differences in dust life cycle processes outlined in Sec. 3.5.1, while the range in $\tau_{\rm equil}$ for a given dust species is due to differences in gas cycling and SNe destruction timescales between galaxies. We can confirm this with predictions of $\tau_{\rm equil}$ from analytical models (Eq. 20 and Eq. 21 in C22). In Fig. 3.12, we show the predicted evolution of the degree of condensation for Si bound in silicate dust ($f_{\rm Si}$) from this model. We assume an initial degree of condensation of $f_{\rm o,Si}$=0.01, cold cloud lifetime of $\tau_{\rm cloud}{\sim}10$ Myr estimated from Milky Way-mass galaxy simulations in Benincasa et al. (2020), and a constant accretion growth timescale of $\tau_{\rm grow}{\sim}40$ Myr which is the median value for gas in which accretion can occur in our model (T<300 K) for all galaxies in our sample at the onset of efficient silicate dust growth. We vary the SNe dust destruction timescale ($\tau_{\rm d}$; Eq. 18 in McKee 1989) and the fraction of the ISM with gas T<300 K ($X_{\rm cloud}$), which determines the average time it takes to cycle all ISM material from the cold cloud phase through the diffuse/warm ISM phases and back into cold clouds $\tau_{\rm cycle} = \tau_{\rm cloud}\frac{1-X_{\rm cloud}}{X_{\rm cloud}}$, to match typical values for dwarf, Milky Way, and massive galaxies. By varying these two parameters, we predict a spread in $\tau_{\rm equil}$ similar to those exhibited in our simulations. However, these predictions are an upper bound on $\tau_{\rm equil}$, especially for galaxies with high star formation rates, since $\tau_{\rm grow}$ inversely scales with metallicity and will thus decrease over time. We also note that our simulations' resulting equilibrium timescales depend on our model's prescriptions for accretion and SNe dust destruction. In particular, our accretion routine assumes a constant size distribution, which will underpredict accretion timescales, and the theoretical predictions for SNe dust destruction efficiency varying substantially (e.g. Hu et al., 2019; Kirchschlager et al., 2022).

The equilibrium timescale has important implications for the expected relation between galactic D/Z and metallicity when it is compared to the galactic metal enrichment timescale $\tau_{\rm metal}$, which we define as the time it takes for the galactic metallicity to double. For $\tau_{\rm equil} \lesssim \tau_{\rm metal}$, the dust population within a galaxy is able to reach a relative equilibrium D/Z for a given metallicity before it changes appreciably. This is similar to the model predictions presented in Feldmann (2015), which assumes equilibrium galactic metallicity and D/Z. When $\tau_{\rm equil} \gtrsim \tau_{\rm metal}$, the dust population is still in the process of building up its mass and will 'lag' behind the predicted equilibrium D/Z at a given metallicity. However, since $\tau_{\rm equil}$ inversely scales with metallicity, as the galactic metallicity increases, $\tau_{\rm equil}$ will eventually fall below $\tau_{\rm metal}$, causing these two trends to converge. This effect can be seen in the evolution between galactic D/Z and Z for each galaxy shown in Fig. 3.9, with the emergence of two evolutionary states we call 'equilibrium' and 'lagging'. The 'equilibrium' state is exhibited by galaxies that have long quiescent periods, evolving in isolation for the majority of their life and/or experiencing relatively constant and low star formation rates (i.e. **m11v_halo2**, **m11v_halo0**, and **m11i**) resulting in large $\tau_{\rm metal}$. These

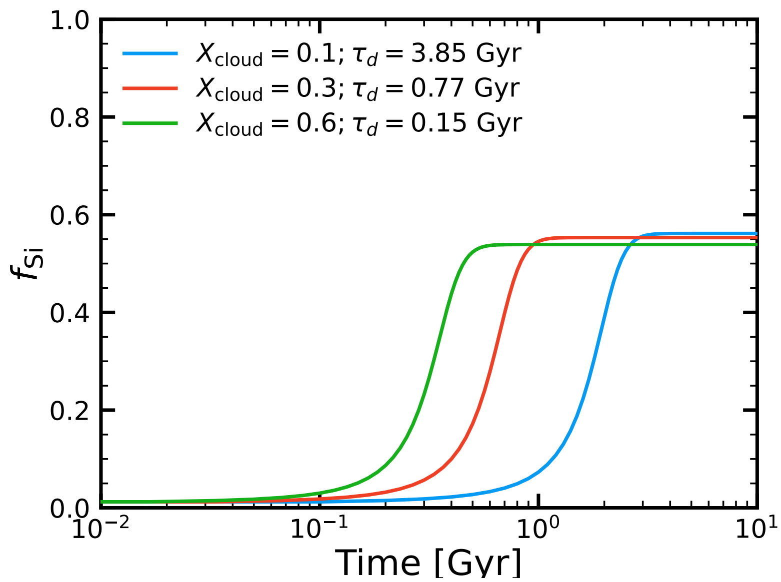

Figure 3.12. Predicted evolution of the degree of condensation for Si bound in silicate dust through successive cycles of gas into dense clouds, where the dust grows via accretion, and out into diffuse clouds, where it is destroyed by SNe, using Eq. 20 and Eq. 21 in C22. We assume an initial degree of condensation $f_{\rm Si}$=0.01, dust growth timescale $\tau_{\rm grow}$~40 Myr, and cold cloud lifetime $\tau_{\rm cloud}$~10 Myr. We vary the SNe dust destruction timescale ($\tau_{\rm d}$) and the fraction of the ISM in cold clouds ($X_{\rm cloud}$), selecting values typical for (*red*) a MW-mass galaxy, (*blue*) a dwarf-mass galaxy, and (*green*) a massive galaxy. While the resulting equilibrium fractions are similar, the time to equilibrium varies dramatically $\tau_{\rm equil}$~0.4−3 Gyr, matching the spread in $\tau_{\rm equil}$ seen in our simulations. However, these predictions are an upper bound on $\tau_{\rm equil}$ since $\tau_{\rm grow}$ will decrease over time as the metallicity of a galaxy increases.

galaxies all follow the same relation between D/Z and metallicity, similar to the equilibrium predictions from Feldmann (2015). The 'lagging' state is exhibited by galaxies that have chaotic episodes, experiencing major and/or multiple minor merger events and bursty star formation rates (i.e. **m12i**, **m11d**, and **m11e**) resulting in instances of small $\tau_{\rm metal}$. These galaxies exhibit relations between D/Z and metallicity that periodically fall below the 'equilibrium' trend, which roughly correspond with recent chaotic periods. These results suggest that recent galactic history plays a critical role in the expected galactic D/Z for galaxies in which gas-dust accretion is efficient and could explain a portion of the scatter in observed D/Z at a fixed metallicity. However, our sample of galaxies is small and only includes one Milky Way-mass galaxy, which exhibits the largest deviation from equilibrium predictions. More simulations are therefore needed to make a more statically robust conclusion.

3.6 Conclusions

In this work, we investigate the evolution of galactic dust populations, in both composition and amount, across cosmic time utilizing a suite of 7 cosmological zoom-in simulations run with the FIRE-2 model (Hopkins et al., 2018a) for stellar feedback and ISM physics and the "Species" dust evolution model (C22). This dust evolution model accounts for dust creation in stellar outflows, growth from gas-phase accretion, destruction from SNe shocks, thermal sputtering, and astration, and turbulent dust and metal diffusion in gas. It tracks the evolution of specific dust species (silicates, carbon, silicon carbide), treating each uniquely depending on their chemical composition, along with theoretical nano-particle metallic iron (Nano-iron) dust species and an oxygen-based (O-reservoir) dust species. It also incorporates a physically motivated dust growth routine which accounts for Coulomb enhancement and CO formation in dense molecular environments.

The 7 galaxies we selected cover a broad range of stellar ($10^6\,{\rm M}_\odot < M_* < 10^{11}\,{\rm M}_\odot$) and halo ($10^9\,{\rm M}_\odot < M_{\rm vir} < 10^{12}\,{\rm M}_\odot$) masses at present day and showcase a variety of growth histories.

We summarize our findings of dust population evolution below:

1. Despite the variety of galactic evolutionary histories probed in our sample, all galactic dust populations follow similar evolutionary trends. Initially, they are dominated by dust production from first SNe II and later (~2 Gyr) AGB stars. Above a critical metallicity threshold, gas-dust accretion becomes efficient and eventually increases the galactic D/Z>0.1 (Fig. 3.3, 3.4, & 3.5). This suggests that gas-dust accretion is the main producer of dust mass for all but the most metal-poor galaxies and, in the case of Milky Way-mass galaxies, for a majority of the galaxy's life.

2. Differences between key element abundances, physical properties, and life cycle processes between dust species result in varying critical metallicities of $Z_{\rm crit}$~$0.05Z_{\odot}$,$0.2Z_{\odot}$, and $0.5Z_{\odot}$ for metallic iron, silicates, and carbonaceous dust respectively. These differences reproduce observed depletions of Si, Mg, and Fe in the MW, LMC, and SMC (Fig. 3.6 & 3.7), and suggest that silicate and a theoretical iron-bearing dust species grow efficiently by accretion in the LMC and SMC. They also suggest that C depletion decreases rapidly with galactic metallicity, which could explain the reduced amount of small carbonaceous grains observed in the LMC and SMC.

3. After the onset of efficient gas-dust accretion, there is a characteristic equilibrium timescale over which dust mass builds up over time until an equilibrium between dust growth and SNe dust destruction is reached. This equilibrium timescale is $\gtrsim$1 Gyr in our sample and varies between galaxies. For galaxies with quiescent histories (long metal enrichment timescales), their dust populations are almost always in relative equilibrium and produce similar galaxy-integrated D/Z-Z trends. For galaxies with more chaotic histories (short metal enrichment timescales), their dust populations periodically 'lag' behind the expected equilibrium values, producing lower D/Z. These 'lagging' dust populations can explain part of the large scatter in the observed relation between galaxy-integrated D/Z and metallicity (Fig. 3.9).

4. Extragalactic observations of spatially-resolved D/Z in spiral galaxies are roughly consistent with our Milky Way-mass galaxy (Fig. 3.10). When compared to high-resolution observations of D/$H_{neutral}$ in Local Group galaxies, our model overpredicts the amount of dust in diffuse neutral gas (Fig. 3.11), but this may be due to our approximations of observables and a more direct comparison is needed.

Acknowledgements

CC and DK were supported by NSF grant AST-1715101 and the Cottrell Scholar Award from the Research Corporation for Science Advancement. We ran simulations using: the Extreme Science and Engineering Discovery Environment (XSEDE), supported by NSF grant ACI-1548562; Frontera allocations AST21010 and AST20016, supported by the NSF and TACC; Triton Shared Computing Cluster (TSCC) at the San Diego Supercomputer Center. The data used in this work were, in part, hosted on facilities supported by the Scientific Computing Core at the Flatiron Institute, a division of the Simons Foundation. This work also made use of MATPLOTLIB (Hunter, 2007), NUMPY (Harris et al., 2020), SCIPY (Virtanen et al., 2020), and NASA's Astrophysics Data System.

3.A Sight Line Methodology

To compare directly to observations of element depletions in the MW, we created a set of ~3000 sight lines within the galactic disk of **m12i**. Each sight line is determined as follows: **(1)** a point within an annulus ($r \sim 5-8$kpc) of the galactic disk is chosen at random (this choice of range is due to **m12i**'s less extended disk compared to the MW); this is the end of our sight line. **(2)** Up to 10 young star particles (t_{age} < 10 Myr) within $0.1-2$ kpc of the given point are chosen at random and will be the start of our sight lines. The specified stellar age and sight line distances are chosen to match the bias of observations to O & B type stars and the given sight line distances from Jenkins (2009). A gas density projection of **m12i** with a subsample of sight lines overlaid is shown in Fig. 3.13.

To compare directly to observations of element depletions in the LMC and SMC, we created a set of external sight lines for **m11v_halo0**, **m11d**, **m11e**,**m11v_halo2**, and **m11i**. Each sight line is determined as follows: **(1)** The location of all young ($t_{\rm age}$ < 10Myr) star particles within 10 kpc of the galactic center are determined. This is the start of our sight lines. For reference, there are ~1200, ~600, ~100, ~200, and ~30 young star particles within **m11v_halo0**, **m11d**, **m11e**, **m11v_halo2**, and **m11i** respectively. **(2)** Three endpoints are determined to create three sight lines for each star particle. These endpoints are situated ~50 kpc away (similar to the distance to the LMC and SMC) in three directions, one face-on with the average angular momentum vector of young stars in the galaxy, one orthogonal to the angular momentum vector, and one halfway between the two. A gas density projection of the dwarf galaxies with young stellar populations overlaid is shown in Fig. 3.14.

We then use the YTRay object in yt (Turk et al., 2011) to determine the gas cells intersected by a given sight line. This assumes spherical gas particles using the gas cell coordinates and smoothing kernel lengths from GIZMO. Given a sight line start and end point, the intersected particles and their intersection lengths are determined. We then calculate the sight line's $N_{\rm X}$ and $N_{\rm H,neutral}$ from the sum of individual particle column densities determined from their H and element X number densities, assuming they are uniform within each cell, and intersection length.

3.B Defining Oxygen Abundance and Metallicity

In this section, we investigate different definitions for galaxy-integrated oxygen abundance and discuss our choice of definition. These definitions are **(1)** the mass-weighted median O abundance in gas cells with 7000 < T < 15000 K and $n_{\rm H}$ > 0.5 cm^{-3}. This is motivated by galaxy-integrated observations which mainly probe auroral and nebular O emission lines in HII regions (i.e Pilyugin & Grebel, 2016). **(2)** The mass-weighted median O abundance for all gas. **(3)** & **(4)** The same as (1) and (2) but only gas-phase O abundance (accounting for O depleted

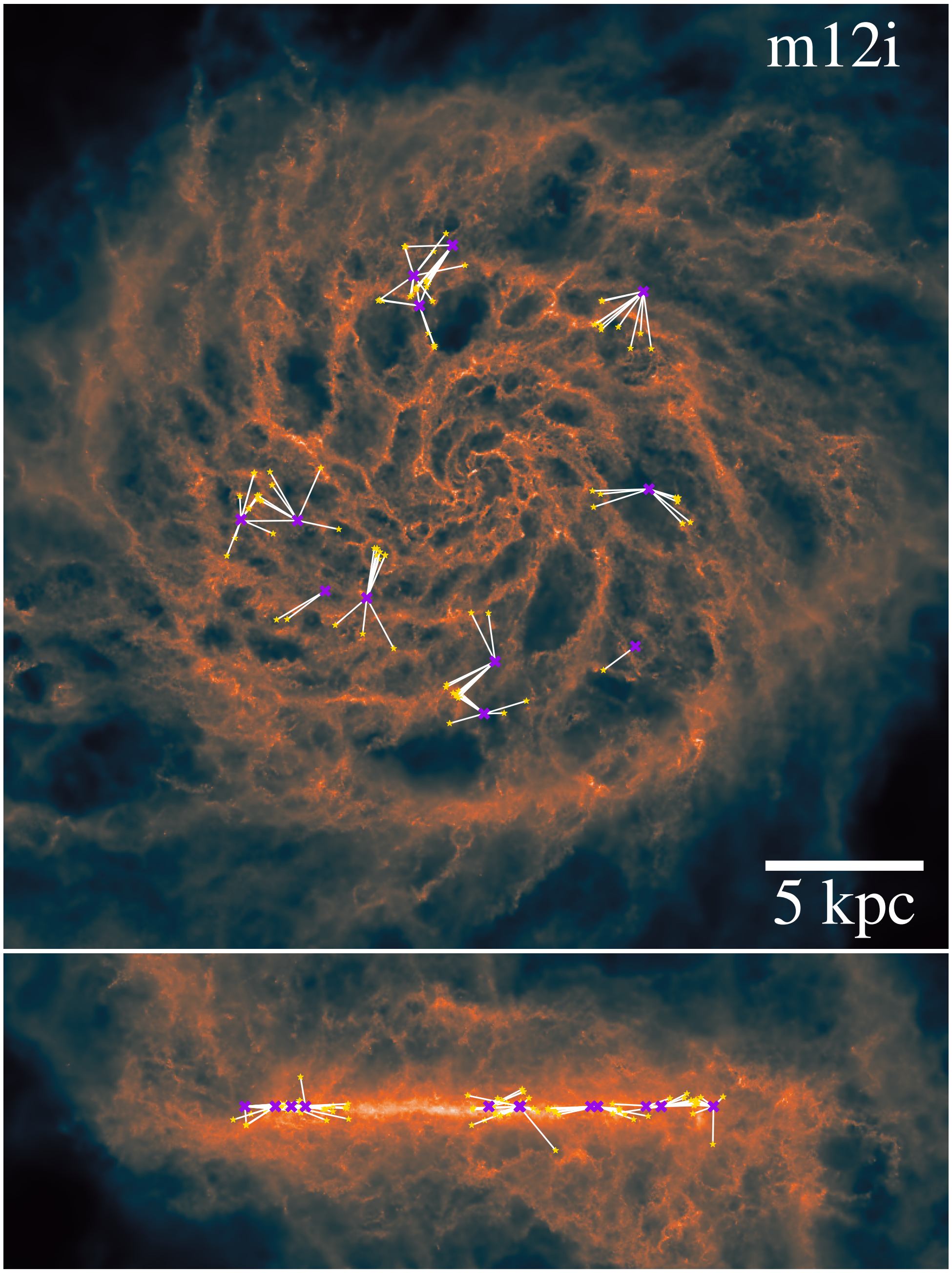

Figure 3.13. Face-on (*top*) and edge-on (*bottom*) gas density projection of **m12i** with a subset of our sight lines (*white lines*) to young stars overplotted. The end points (*purple crosses*) of the sight lines are randomly selected within the disk. The start of the sight lines (*gold stars*) are up to 10 young star particles within 0.1 – 2kpc of the endpoints. Our sight lines probe stars both within and above the disk plane, voids, and dense spiral arms.

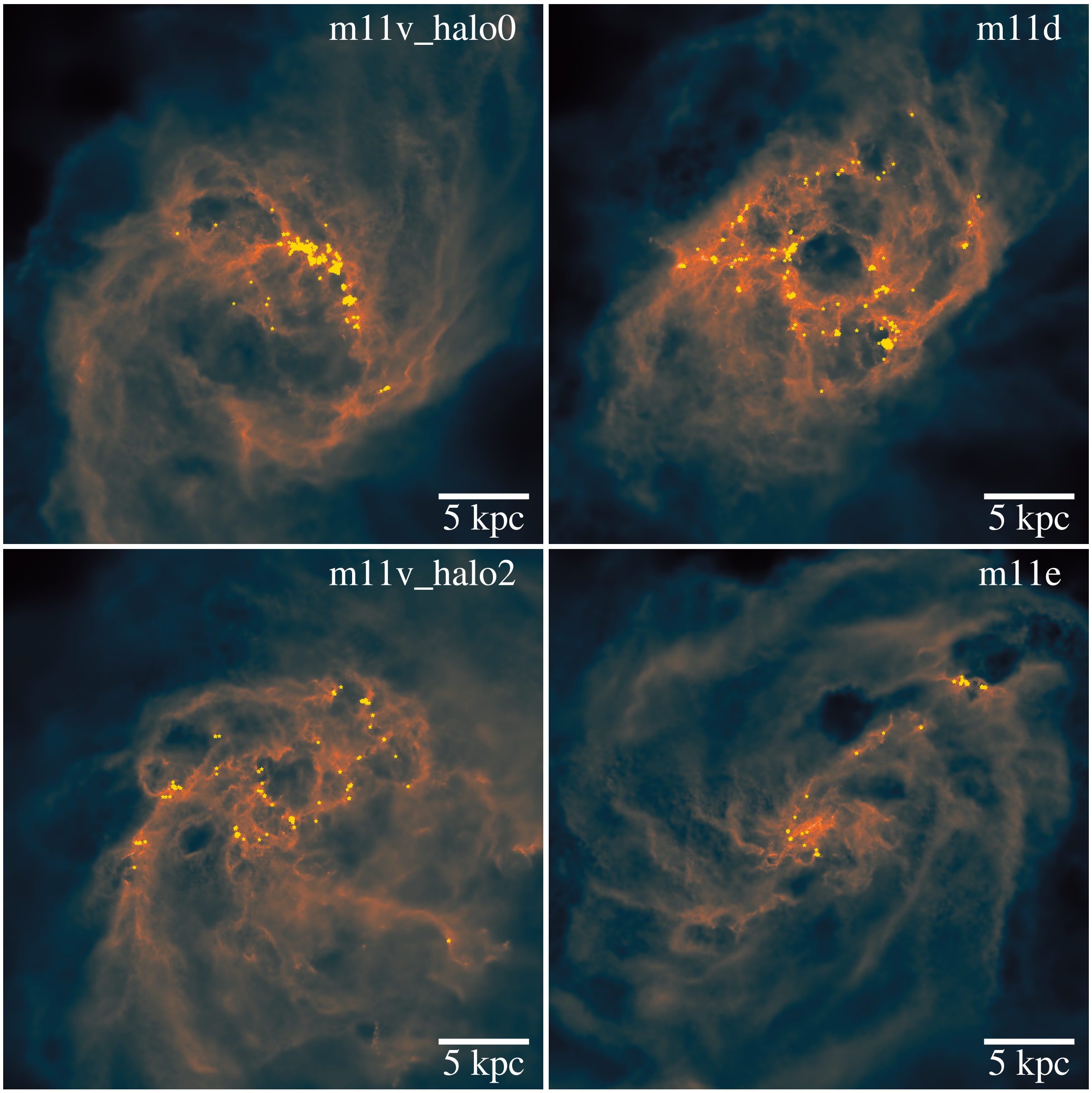

Figure 3.14. Face-on gas density projection of **m11v_halo0** (*top left*), **m11d** (*top right*), **m11e** (*bottom left*), and **m11v_halo2** (*bottom right*) with all young stars (*gold stars*) overplotted. Three sight lines are created for each young star particle to simulate the view of an outside observer at different orientations. One is face-on with the average angular momentum vector of young stars in the galaxy, one is orthogonal to the angular momentum vector, and one is halfway between the two. Note that the number of young stars varies by up to 1 dex between the different galaxies however, they all roughly trace the densest parts of each galaxy.

onto dust). Note only some observations even account for possible depletion of metals into dust (e.g De Vis et al., 2019). All of these definitions only consider gas within 0.1 $R_{\rm vir}$ of the galactic center. We show the differences between these definitions in Fig. 3.15 for our suite of galaxies. On average, definitions (1) and (2) are consistent and match previous work from Ma et al. (2016, Appendix A & B). However, accounting for O depletion into dust causes the relation to diverge for $12+\log_{10}(\mathrm{O/H}) > 8.3$ due to the onset of efficient dust growth. This difference decreases for ionized gas due to the tendency for this gas to have experienced a recent SNe event, which destroys dust and reduces O depletion.

Another caveat is the assumed metal abundances in our simulations. FIRE-2 adopts abundances from Anders & Grevesse (1989) ($12+\log_{10}(\mathrm{O/H})_{\odot} = 8.93$), but most observations use more recent Asplund et al. (2009) proto-solar abundances ($12+\log_{10}(\mathrm{O/H})_{\odot} = 8.73$). We show the resulting relation between definition (1) and Z for our simulations in Fig. 3.16. The median total O abundance closely follows the total metallicity of the galaxy and so including an overall offset of -0.2 dex in our definition of oxygen abundance will correct for this difference in adopted abundances.

For the reasons shown above, we define the galaxy-integrated $12+\log_{10}(\mathrm{O/H})$ as the weighted median gas phase O abundance (accounting for O locked in dust) in ionized regions, gas cells with $7000 < T < 15000$ K and $n_{\rm H} > 0.5$ cm^{-3}, with a -0.2 dex offset.

Chapter 3, in full, is currently being prepared for submission for publication of the material. Choban, Caleb R.; Kereš, Dušan. The dissertation author was the primary investigator and author of this material.

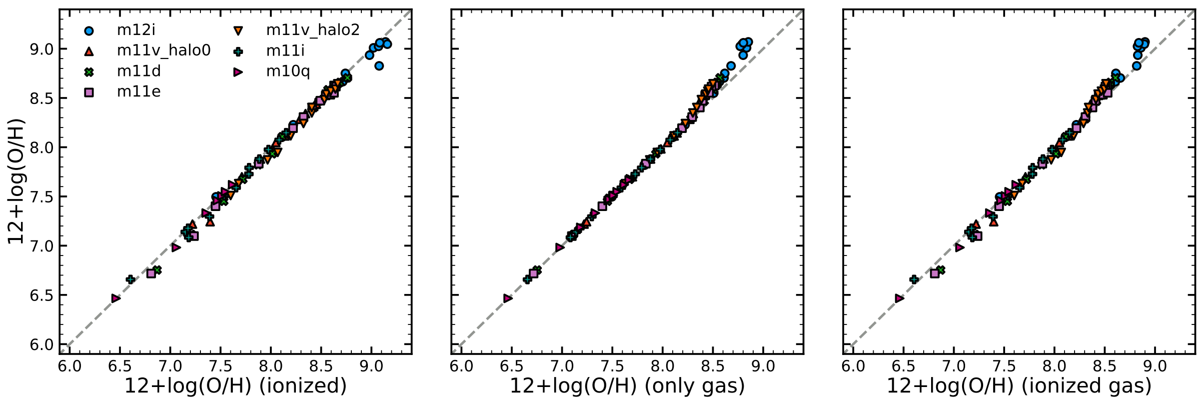

Figure 3.15. Resulting oxygen abundances from different definitions for our suite of simulations. (*left:*) Relation between oxygen abundances for definition (1), median O abundance for all gas within $0.1R_{\rm vir}$, and definition (2), median O abundance for all gas with $7000 < T < 15000$ K and $n_{\rm H} > 0.5$ cm^{-3}. (*middle:*) Relation between oxygen abundances for definition (1) and (3), median gas-phase O abundance (accounting for O depleted into dust) for all gas within $0.1R_{\rm vir}$. (*right:*) Relation between oxygen abundances for definition (1) and (4), median gas-phase O abundance (accounting for O depleted into dust) for all gas with $7000 < T < 15000$ K and $n_{\rm H} > 0.5$ cm^{-3}. The data points shown are the same as those in Fig. 3.9.

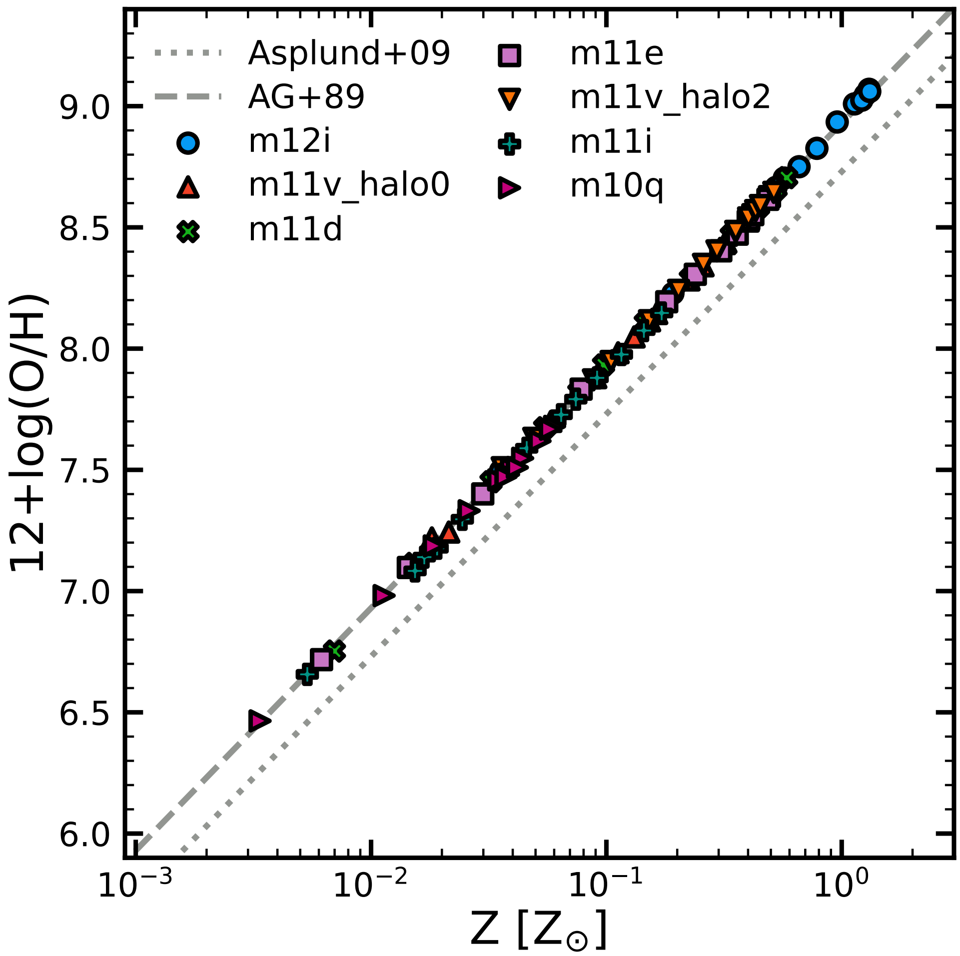

Figure 3.16. Resulting relation between median O abundance and median metallicity for all gas within $0.1R_{\rm vir}$ for our suite of simulations. The data points shown are the same as those in Fig. 3.9. Our simulations follow the O abundances expected from Anders & Grevesse (1989) which are offset by ~0.2 dex from Asplund et al. (2009) abundances usually assumed by observations.

Chapter 4

Conclusions and Future Endeavours

In Chapter 2, we have introduced two separate dust evolution models integrated into cosmological galaxy formation simulations, which showcase the advantages and shortcomings of differing prescriptions used for modeling the dust life cycle. We summarize the results and their implications here:

1. Both models reaffirm that the galaxy-integrated D/Z$\sim$0.4 within the Milky Way is produced by a balance between dust growth via gas-phase accretion and dust destruction by SNe, with little dependence on the efficiency of initial stellar dust production.

2. A dust evolution model that assumes a single, chemically ambiguous dust species and utilizes a 'tunable' gas-dust accretion routine is inherently unable to reproduce the variations in observed Milky Way element depletions. It also produces a relatively flat D/Z-$n_{\rm H,neutral}$ relation owing to unrestricted accretion.

3. A dust evolution model that tracks the evolution of specific dust species with set chemical compositions and incorporates a physically motivated dust growth routine can reproduce observed Mg, Si, and C depletions in the Milky Way.

4. We find the inclusion of additional theoretical metallic iron and an O-bearing dust species are needed in order to match observations of O and Fe depletions. The additional depletion of O is also critical for the matching expected D/Z in dense environments.

5. Accounting for the formation of CO in dense molecular gas is needed to match observed C depletions and ensures carbonaceous dust is not overproduced in dense environments.

In Chapter 3, we presented a suite of cosmological zoom-in simulations with our integrated dust evolution model. We investigate their predictions for the evolution of galactic dust populations for Milky Way to dwarf-halo mass galaxies and find that:

1. For all but the most metal-poor galaxies, gas-dust accretion is the dominant producer of dust mass, and, for Milky Way-mass galaxies in particular, dominants for a majority of the galaxy's life.

2. Each dust species has a unique critical metallicity, above which gas-dust accretion becomes efficient. These do not vary between galaxies but do vary between dust species with $Z_{\rm crit} \approx 0.05 - 0.5 Z_{\odot}$. This is caused by differences in key element abundances, physical properties, and life cycle processes between each dust species.

3. These differences in critical metallicity result in an evolving chemical composition, which could explain the differences in silicate and carbonaceous dust observed in the LMC and SMC compared to the Milky Way.

4. The time between the onset of gas-dust accretion and when the dust population reaches equilibrium is ~0.5−3 Gyr depending on the dust species and galaxy. This suggests gas-dust accretion can produce dusty galaxies at high redshift and could contribute to the scatter in observed galaxy-averaged D/Z at any given metallicity.

Despite the success of these models, they are in no way 'complete' or free of assumptions. However, they provide a solid foundation for future investigation into galactic dust evolution and are primed for the inclusion of more in-depth physics and implementation in other astrophysical environments. In future work, we will integrate these dust models with the physics already incorporated in galaxy formation simulations and investigate their effects on galaxy formation and evolution.

In addition, there are several prospective projects stemming from this work. The first involves expanding the dust evolution model presented to investigate the evolution of grain sizes which would require the development and integration of grain size evolution models (e.g. McKinnon et al., 2018; Aoyama et al., 2020). All processes involving dust depend strongly on the size distribution of dust grains, with small grains dominating the effective cross-section of a dust population and dictating interaction rates. Many processes in the dust life cycle grow, shrink, or destroy dust grains evolving the grain size distribution over time. With this improved model, the evolution of dust grain size distributions could be investigated along with what effects its inclusion has on the global evolution of dust populations compared to the static grain size assumption. The resulting grain size distributions from this model can also be convolved with assumed extinction efficiencies for each dust species to predict effective extinction curves within galaxies. The results of this model could also be directly compared to existing and future IR observations using radiative transfer codes (i.e. SKIRT; Camps & Baes 2015), which would utilize the tracked dust mass and dust grain size distributions within these simulations to create mock observations of the resulting galactic and spatially-resolved SEDs.

This improved model would also allow for the investigation of PAH formation and evolution. The exact origin and evolution of PAHs is currently unexplained, with a plethora of proposed formation mechanisms, including formation within AGB stellar winds (Galliano et al., 2008), photoprocessing of small, amorphous carbonaceous grains (Hirashita & Murga, 2020), and low-temperature chemical channels (Parker et al., 2012). As a first step, the evolution of extremely small carbonaceous grains in these simulations could serve as a proxy for PAHs. Simplified PAH formation prescriptions stemming from these proposed formation channels could be subsequently developed and integrated to investigate their implications for PAH evolution. This work would be especially timely given the numerous ongoing and future JWST observations of PAHs.

Another potential avenue of study is the simulation of dust grain evolution in giant molecular clouds (GMCs) to investigate its effects on individual star formation. On these scales, radiation pressure plays a significant role in regulating gas accretion onto newly formed stars and disrupting the collapse of GMCs, halting further star formation (Grudić et al., 2022). The effectiveness of radiation pressure to evacuate gas depends on primarily on the size of dust grains in the immediate region around the radiative source (star) and the coupling of dust and gas via dust-gas dynamics. However, small grains may be relatively rare in these environments (Ormel et al., 2011), and dust and gas can decouple. By integrating these dust evolution models into STARFORGE (Grudić et al., 2021), a state-of-the-art molecular cloud and star formation feedback model, and coupling them with the gas-dust dynamics model presented in Hopkins et al. (2022), it would be possible to investigate the effects dust evolution and dynamics have on the predicted final mass of stars and the overall efficiency of star formation.

Bibliography

Altobelli N., Postberg F., Fiege K., Trieloff M., Kimura H., Sterken V. J., Hsu H.-W., Hillier J., Khawaja N., Moragas-Klostermeyer G., Blum J., Burton M., Srama R., Kempf S., Gruen E., 2016, Science, 352, 312

Anders E., Grevesse N., 1989, Geochimica et Cosmochimica Acta, 53, 197

Anglés-Alcázar D., Faucher-Giguère C.-A., Kereš D., Hopkins P. F., Quataert E., Murray N., 2017, Monthly Notices of the Royal Astronomical Society, 470, 4698

Aniano G., Draine B. T., Calzetti D., Dale D. A., Engelbracht C. W., Gordon K. D., Hunt L. K., Kennicutt R. C., Krause O., Leroy A. K., Rix H. W., Roussel H., Sandstrom K., Sauvage M., Walter F., Armus L., Bolatto A. D., Crocker A., Donovan Meyer J., Galametz M., Helou G., Hinz J., Johnson B. D., Koda J., Montiel E., Murphy E. J., Skibba R., Smith J. D. T., Wolfire M. G., 2012, The Astrophysical Journal, 756, 138

Aniano G., Draine B. T., Hunt L. K., Sandstrom K., Calzetti D., Kennicutt R. C., Dale D. A., Galametz M., Gordon K. D., Leroy A. K., Smith J. D. T., Roussel H., Sauvage M., Walter F., Armus L., Bolatto A. D., Boquien M., Crocker A., De Looze I., Donovan Meyer J., Helou G., Hinz J., Johnson B. D., Koda J., Miller A., Montiel E., Murphy E. J., Relaño M., Rix H. W., Schinnerer E., Skibba R., Wolfire M. G., Engelbracht C. W., 2020, The Astrophysical Journal, 889, 150

Aoyama S., Hirashita H., Nagamine K., 2020, Monthly Notices of the Royal Astronomical Society, 491, 3844

Aoyama S., Hou K.-C., Shimizu I., Hirashita H., Todoroki K., Choi J.-H., Nagamine K., 2017, Monthly Notices of the Royal Astronomical Society, 466, 105

Asano R. S., Takeuchi T. T., Hirashita H., Inoue A. K., 2013, Earth, Planets, and Space, 65, 213

Asplund M., Grevesse N., Sauval A. J., Scott P., 2009, Annual Review of Astronomy and Astrophysics, 47, 481

Barnard E. E., 1907, The Astrophysical Journal, 25, 218

Barnard E. E., 1910, The Astrophysical Journal, 31, 8

Bekki K., 2013, Monthly Notices of the Royal Astronomical Society, 432, 2298

Bekki K., 2015a, The Astrophysical Journal, 799, 166

Bekki K., 2015b, Monthly Notices of the Royal Astronomical Society, 449, 1625

Benincasa S. M., Loebman S. R., Wetzel A., Hopkins P. F., Murray N., Bellardini M. A., Faucher-Giguère C.-A., Guszejnov D., Orr M., 2020, Monthly Notices of the Royal Astronomical Society, 497, 3993

Bianchi S., 2013, Astronomy and Astrophysics, 552, A89

Bolatto A. D., Wolfire M., Leroy A. K., 2013, Annual Review of Astronomy and Astrophysics, 51, 207

Boogert A. C. A., Gerakines P. A., Whittet D. C. B., 2015, Annual Review of Astronomy and Astrophysics, 53, 541

Burgh E. B., France K., Jenkins E. B., 2010, The Astrophysical Journal, 708, 334

Burke J. R., Hollenbach D. J., 1983, The Astrophysical Journal, 265, 223

Camps P., Baes M., 2015, Astronomy and Computing, 9, 20

Camps P., Trayford J. W., Baes M., Theuns T., Schaller M., Schaye J., 2016, Monthly Notices of the Royal Astronomical Society, 462, 1057

Chastenet J., Sandstrom K., Chiang I.-D., Leroy A. K., Utomo D., Bot C., Gordon K. D., Draine B. T., Fukui Y., Onishi T., Tsuge K., 2019, The Astrophysical Journal, 876, 1, 62

Chastenet J., Sandstrom K., Chiang I.-D., Hensley B. S., Draine B. T., Gordon K. D., Koch E. W., Leroy A. K., Utomo D., Williams T. G., 2021, The Astrophysical Journal, 912, 103

Chawner H., Marsh K., Matsuura M., Gomez H. L., Cigan P., De Looze I., Barlow M. J., Dunne L., Noriega-Crespo A., Rho J., 2019, Monthly Notices of the Royal Astronomical Society, 483, 70

Chiang I.-D., 2021, Observations of Spatially Resolved Dust Evolution in Nearby Galaxies, Ph.D. thesis, UC San Diego

Chiang I.-D., Hirashita H., Chastenet J., Koch E. W., Leroy A. K., Rosolowsky E., Sandstrom K. M., Sardone A., Sun J., Williams T. G., 2023, Monthly Notices of the Royal Astronomical

Society, 520, 5506

Chiang I.-D., Sandstrom K. M., Chastenet J., Herrera C. N., Koch E. W., Kreckel K., Leroy A. K., Pety J., Schruba A., Utomo D., Williams T., 2021, The Astrophysical Journal, 907, 29

Chiang I.-D., Sandstrom K. M., Chastenet J., Johnson L. C., Leroy A. K., Utomo D., 2018, The Astrophysical Journal, 865, 117

Choban C. R., Kereš D., Hopkins P. F., Sandstrom K. M., Hayward C. C., Faucher-Giguère C.-A., 2022, Monthly Notices of the Royal Astronomical Society, 514, 4506

Cioffi D. F., McKee C. F., Bertschinger E., 1988, The Astrophysical Journal, 334, 252

Clark C. J. R., Roman-Duval J. C., Gordon K. D., Bot C., Smith M. W. L., Hagen L. M. Z., 2023, The Astrophysical Journal, 946, 42

Costantini E., Pinto C., Kaastra J. S., in't Zand J. J. M., Freyberg M. J., Kuiper L., Méndez M., de Vries C. P., Waters L. B. F. M., 2012, Astronomy and Astrophysics, 539, A32

De Looze I., Barlow M. J., Bandiera R., Bevan A., Bietenholz M. F., Chawner H., Gomez H. L., Matsuura M., Priestley F., Wesson R., 2019, Monthly Notices of the Royal Astronomical Society, 488, 164

De Vis P., Jones A., Viaene S., Casasola V., Clark C. J. R., Baes M., Bianchi S., Cassara L. P., Davies J. I., De Looze I., Galametz M., Galliano F., Lianou S., Madden S., Manilla-Robles A., Mosenkov A. V., Nersesian A., Roychowdhury S., Xilouris E. M., Ysard N., 2019, Astronomy and Astrophysics, 623, A5

Draine B. T., 1990, in The Evolution of the Interstellar Medium, edited by L. Blitz, vol. 12 of Astronomical Society of the Pacific Conference Series, 193–205

Draine B. T., 2009, in Cosmic Dust - near and Far, edited by T. Henning, E. Grün, J. Steinacker, vol. 414 of Astronomical Society of the Pacific Conference Series, 453

Draine B. T., 2011, Physics of the Interstellar and Intergalactic Medium by Bruce T. Draine. Princeton University Press, 2011. ISBN: 978-0-691-12214-4

Draine B. T., Aniano G., Krause O., Groves B., Sandstrom K., Braun R., Leroy A., Klaas U., Linz H., Rix H.-W., Schinnerer E., Schmiedeke A., Walter F., 2014, The Astrophysical Journal, 780, 172

Draine B. T., Dale D. A., Bendo G., Gordon K. D., Smith J. D. T., Armus L., Engelbracht C. W., Helou G., Kennicutt Jr. R. C., Li A., Roussel H., Walter F., Calzetti D., Moustakas J., Murphy E. J., Rieke G. H., Bot C., Hollenbach D. J., Sheth K., Teplitz H. I., 2007, The Astrophysical

Journal, 663, 866

Draine B. T., Li A., 2007, The Astrophysical Journal, 657, 810

Draine B. T., Salpeter E. E., 1979, The Astrophysical Journal, 231, 77

Dwek E., 1987, The Astrophysical Journal, 322, 812

Dwek E., 1998, The Astrophysical Journal, 501, 643

Dwek E., 2005, in The Spectral Energy Distributions of Gas-Rich Galaxies: Confronting Models with Data, edited by C. C. Popescu, R. J. Tuffs, vol. 761 of American Institute of Physics Conference Series, 103–122

Dwek E., 2016, The Astrophysical Journal, 825, 136

Dwek E., Werner M. W., 1981, The Astrophysical Journal, 248, 138

El-Badry K., Quataert E., Wetzel A., Hopkins P. F., Weisz D. R., Chan T. K., Fitts A., Boylan-Kolchin M., Kereš D., Faucher-Giguère C.-A., Garrison-Kimmel S., 2018, Monthly Notices of the Royal Astronomical Society, 473, 1930

Escala I., Wetzel A., Kirby E. N., Hopkins P. F., Ma X., Wheeler C., Kereš D., Faucher-Giguère C.-A., Quataert E., 2018, Monthly Notices of the Royal Astronomical Society, 474, 2, 2194

Faucher-Giguère C.-A., Kereš D., 2011, Monthly Notices of the Royal Astronomical Society: Letters, 412, 1, L118

Faucher-Giguère C.-A., Lidz A., Zaldarriaga M., Hernquist L., 2009, The Astrophysical Journal, 703, 1416

Feldmann R., 2015, Monthly Notices of the Royal Astronomical Society, 449, 3, 3274

Ferrarotti A. S., Gail H.-P., 2006, Astronomy and Astrophysics, 447, 553

Galliano F., Dwek E., Chanial P., 2008, The Astrophysical Journal, 672, 214

Galliano F., Galametz M., Jones A. P., 2018, Annual Review of Astronomy and Astrophysics, 56, 673

Galliano F., Nersesian A., Bianchi S., De Looze I., Roychowdhury S., Baes M., Casasola V., Cassará L. P., Dobbels W., Fritz J., Galametz M., Jones A. P., Madden S. C., Mosenkov A., Xilouris E. M., Ysard N., 2021, Astronomy & Astrophysics, 649, A18

Gioannini L., Matteucci F., Vladilo G., Calura F., 2017, Monthly Notices of the Royal Astronomical Society, 464, 985

Gjergo E., Granato G. L., Murante G., Ragone-Figueroa C., Tornatore L., Borgani S., 2018, \mnras, 479, 2588

Goldsmith P. F., 2001, The Astrophysical Journal, 557, 736

Goldsmith P. F., Langer W. D., 1978, The Astrophysical Journal, 222, 881

Gomez H. L., Clark C. J. R., Nozawa T., Krause O., Gomez E. L., Matsuura M., Barlow M. J., Besel M.-A., Dunne L., Gear W. K., Hargrave P., Henning T., Ivison R. J., Sibthorpe B., Swinyard B. M., Wesson R., 2012, Monthly Notices of the Royal Astronomical Society, 420, 4, 3557

Gould R. J., Salpeter E. E., 1963, The Astrophysical Journal, 138, 393

Granato G. L., Lacey C. G., Silva L., Bressan A., Baugh C. M., Cole S., Frenk C. S., 2000, The Astrophysical Journal, 542, 710

Granato G. L., Ragone-Figueroa C., Taverna A., Silva L., Valentini M., Borgani S., Monaco P., Murante G., Tornatore L., 2021, Monthly Notices of the Royal Astronomical Society, 503, 511

Graziani L., Schneider R., Ginolfi M., Hunt L. K., Maio U., Glatzle M., Ciardi B., 2020, Monthly Notices of the Royal Astronomical Society, 494, 1071

Grudić M. Y., Guszejnov D., Hopkins P. F., Offner S. S. R., Faucher-Giguère C.-A., 2021, Monthly Notices of the Royal Astronomical Society, 506, 2199

Grudić M. Y., Guszejnov D., Offner S. S. R., Rosen A. L., Raju A. N., Faucher-Giguère C.-A., Hopkins P. F., 2022, Monthly Notices of the Royal Astronomical Society, 512, 216

Hafen Z., Faucher-Giguère C.-A., Anglés-Alcázar D., Stern J., Kereš D., Hummels C., Esmerian C., Garrison-Kimmel S., El-Badry K., Wetzel A., Chan T. K., Hopkins P. F., Murray N., 2019, Monthly Notices of the Royal Astronomical Society, 488, 1248

Harris C. R., Millman K. J., van der Walt S. J., Gommers R., Virtanen P., Cournapeau D., Wieser E., Taylor J., Berg S., Smith N. J., Kern R., Picus M., Hoyer S., van Kerkwijk M. H., Brett M., Haldane A., del Río J. F., Wiebe M., Peterson P., Gérard-Marchant P., Sheppard K., Reddy T., Weckesser W., Abbasi H., Gohlke C., Oliphant T. E., 2020, Nature, 585, 7825, 357

Hayward C. C., Kereš D., Jonsson P., Narayanan D., Cox T. J., Hernquist L., 2011, The Astrophysical Journal, 743, 159

Henning T., 2010, Annual Review of Astronomy and Astrophysics, 48, 21

Hensley B. S., Draine B. T., 2017, The Astrophysical Journal, 834, 134

Hernquist L., 1990, The Astrophysical Journal, 356, 359

Herschel W., 1785, Philosophical Transactions of the Royal Society of London, 75, 213

Hirashita H., 1999, Astronomy and Astrophysics, 344, L87

Hirashita H., 2000, Publications of the Astronomical Society of Japan, 52, 585

Hirashita H., 2015, Monthly Notices of the Royal Astronomical Society, 447, 2937

Hirashita H., Murga M. S., 2020, Monthly Notices of the Royal Astronomical Society, 492, 3779

Höfner S., Olofsson H., 2018, Astronomy and Astrophysics Review, 26, 1, 1

Hollenbach D., Salpeter E. E., 1971, The Astrophysical Journal, 163, 155

Hollenbach D. J., Takahashi T., Tielens A. G. G. M., 1991, The Astrophysical Journal, 377, 192

Hopkins P. F., 2015, Monthly Notices of the Royal Astronomical Society, 450, 53

Hopkins P. F., Kereš D., Oñorbe J., Faucher-Giguère C.-A., Quataert E., Murray N., Bullock J. S., 2014, Monthly Notices of the Royal Astronomical Society, 445, 1, 581

Hopkins P. F., Rosen A. L., Squire J., Panopoulou G. V., Soliman N. H., Seligman D., Steinwandel U. P., 2022, Monthly Notices of the Royal Astronomical Society

Hopkins P. F., Wetzel A., Kereš D., Faucher-Giguère C.-A., Quataert E., Boylan-Kolchin M., Murray N., Hayward C. C., Garrison-Kimmel S., Hummels C., Feldmann R., Torrey P., Ma X., Anglés-Alcázar D., Su K.-Y., Orr M., Schmitz D., Escala I., Sanderson R., Grudić M. Y., Hafen Z., Kim J.-H., Fitts A., Bullock J. S., Wheeler C., Chan T. K., Elbert O. D., Narayanan D., 2018a, Monthly Notices of the Royal Astronomical Society, 480, 800

Hopkins P. F., Wetzel A., Kereš D., Faucher-Giguère C.-A., Quataert E., Boylan-Kolchin M., Murray N., Hayward C. C., El-Badry K., 2018b, Monthly Notices of the Royal Astronomical Society, 477, 1578

Hopkins P. F., Wetzel A., Wheeler C., Sanderson R., Grudić M. Y., Sameie O., Boylan-Kolchin M., Orr M., Ma X., Faucher-Giguère C.-A., Kereš D., Quataert E., Su K.-Y., Moreno J., Feldmann R., Bullock J. S., Loebman S. R., Anglés-Alcázar D., Stern J., Necib L., Choban C. R., Hayward C. C., 2023, Monthly Notices of the Royal Astronomical Society, 519, 3154

Hou K.-C., Aoyama S., Hirashita H., Nagamine K., Shimizu I., 2019, arXiv:1901.02886 [astro-ph]

Hu C.-Y., Zhukovska S., Somerville R. S., Naab T., 2019, Monthly Notices of the Royal Astronomical Society, 487, 3252

Hunter J. D., 2007, Computing in Science Engineering, 9, 3, 90

Inoue A. K., 2011, Earth, Planets and Space, 63, 1027

Irvine W. M., Goldsmith P. F., Hjalmarson Å., 1987, in Interstellar Processes, edited by D. J. Hollenbach, H. A. Thronson, vol. 134 of Astrophysics and Space Science Library, 560–609, Springer Netherlands, Dordrecht

Iwamoto K., Brachwitz F., Nomoto K., Kishimoto N., Umeda H., Hix W. R., Thielemann F.-K., 1999, The Astrophysical Journal Supplement Series, 125, 2, 439

Izzard R. G., Tout C. A., Karakas A. I., Pols O. R., 2004, Monthly Notices of the Royal Astronomical Society, 350, 2, 407

Jansky K. G., 1933, Popular Astronomy, 41, 548

Jenkins E. B., 2009, The Astrophysical Journal, 700, 1299

Jenkins E. B., Tripp T. M., 2011, The Astrophysical Journal, 734, 65

Jenkins E. B., Wallerstein G., 2017, The Astrophysical Journal, 838, 85

Jones A. P., Fanciullo L., Köhler M., Verstraete L., Guillet V., Bocchio M., Ysard N., 2013, Astronomy and Astrophysics, 558, A62

Jones A. P., Tielens A. G. G. M., Hollenbach D. J., 1996, The Astrophysical Journal, 469, 740

Jones A. P., Ysard N., 2019, Astronomy and Astrophysics, 627, A38

Katz N., Weinberg D. H., Hernquist L., 1996, The Astrophysical Journal Supplement Series, 105, 19

Kereš D., Katz N., Weinberg D. H., Davé R., 2005, Monthly Notices of the Royal Astronomical Society, 363, 2

Kirchschlager F., Schmidt F. D., Barlow M. J., De Looze I., Sartorio N. S., 2022, Dust Survival Rates in Clumps Passing through the Cas~A Reverse Shock – II. The Impact of Magnetic Fields

Kriek M., Labbé I., Conroy C., Whitaker K. E., van Dokkum P. G., Brammer G. B., Franx M., Illingworth G. D., Marchesini D., Muzzin A., Quadri R. F., Rudnick G., 2010, The Astrophysical Journal, 722, L64

Kroupa P., 2001, Monthly Notices of the Royal Astronomical Society, 322, 231

Kroupa P., 2002, Science, 295, 5552, 82

Krumholz M. R., Gnedin N. Y., 2011, The Astrophysical Journal, 729, 36

Lacy J. H., Knacke R., Geballe T. R., Tokunaga A. T., 1994, The Astrophysical Journal Letters, 428, L69

Lau R. M., Herter T. L., Morris M. R., Li Z., Adams J. D., 2015, Science, 348, 413

Leitherer C., Schaerer D., Goldader J. D., Delgado R. M. G., Robert C., Kune D. F., de Mello D. F., Devost D., Heckman T. M., 1999, The Astrophysical Journal Supplement Series, 123, 3

Li A., 2020, Nature Astronomy, 4, 339

Li A., Draine B. T., 2001, The Astrophysical Journal, 554, 778

Li Q., Narayanan D., Davé R., 2019, Monthly Notices of the Royal Astronomical Society, 490, 1425

Li Q., Narayanan D., Torrey P., Davé R., Vogelsberger M., 2021, Monthly Notices of the Royal Astronomical Society, 507, 548

Liang L., Feldmann R., Faucher-Giguère C.-A., Kereš D., Hopkins P. F., Hayward C. C., Quataert E., Scoville N. Z., 2018, Monthly Notices of the Royal Astronomical Society, 478, L83

Liang L., Feldmann R., Hayward C. C., Narayanan D., Çatmabacak O., Kereš D., Faucher-Giguère C.-A., Hopkins P. F., 2021, Monthly Notices of the Royal Astronomical Society, 502, 3210

Liang L., Feldmann R., Kereš D., Scoville N. Z., Hayward C. C., Faucher-Giguère C.-A., Schreiber C., Ma X., Hopkins P. F., Quataert E., 2019, Monthly Notices of the Royal Astronomical Society, 489, 1397

Limongi M., Chieffi A., 2018, The Astrophysical Journal Supplement Series, 237, 13

Liszt H. S., 2007, Astronomy and Astrophysics, 476, 291

Lodders K., 2003, The Astrophysical Journal, 591, 1220

Ma X., Hayward C. C., Casey C. M., Hopkins P. F., Quataert E., Liang L., Faucher-Giguère C.-A., Feldmann R., Kereš D., 2019, Monthly Notices of the Royal Astronomical Society, 487, 1844

Ma X., Hopkins P. F., Faucher-Giguère C.-A., Zolman N., Muratov A. L., Kereš D., Quataert E., 2016, Monthly Notices of the Royal Astronomical Society, 456, 2140

Madau P., Dickinson M., 2014, Annual Review of Astronomy and Astrophysics, 52, 415

Mannucci F., Della Valle M., Panagia N., 2006, Monthly Notices of the Royal Astronomical Society, 370, 2, 773

Mathis J. S., Rumpl W., Nordsieck K. H., 1977, The Astrophysical Journal, 217, 425

Matsuura M., Dwek E., Barlow M. J., Babler B., Baes M., Meixner M., Cernicharo J., Clayton G. C., Dunne L., Fransson C., Fritz J., Gear W., Gomez H. L., Groenewegen M. A. T., Indebetouw R., Ivison R. J., Jerkstrand A., Lebouteiller V., Lim T. L., Lundqvist P., Pearson C. P., Roman-Duval J., Royer P., Staveley-Smith L., Swinyard B. M., van Hoof P. A. M., van Loon J. Th., Verstappen J., Wesson R., Zanardo G., Blommaert J. A. D. L., Decin L., Reach W. T., Sonneborn G., Van de Steene G. C., Yates J. A., 2015, The Astrophysical Journal, 800, 50

Matsuura M., Dwek E., Meixner M., Otsuka M., Babler B., Barlow M. J., Roman-Duval J., Engelbracht C., Sandstrom K., Lakićević M., van Loon J. Th., Sonneborn G., Clayton G. C., Long K. S., Lundqvist P., Nozawa T., Gordon K. D., Hony S., Panuzzo P., Okumura K., Misselt K. A., Montiel E., Sauvage M., 2011, Science, 333, 1258

Mattsson L., Andersen A. C., 2012, Monthly Notices of the Royal Astronomical Society, 423, 38

McKee C., 1989, in Interstellar Dust, edited by L. J. Allamandola, A. G. G. M. Tielens, vol. 135 of IAU Symposium, 431

McKinnon R., Torrey P., Vogelsberger M., 2016, Monthly Notices of the Royal Astronomical Society, 457, 3775

McKinnon R., Torrey P., Vogelsberger M., Hayward C. C., Marinacci F., 2017, Monthly Notices of the Royal Astronomical Society, 468, 1505

McKinnon R., Vogelsberger M., Torrey P., Marinacci F., Kannan R., 2018, Monthly Notices of the Royal Astronomical Society, 478, 2851

Melbourne J., Williams B. F., Dalcanton J. J., Rosenfield P., Girardi L., Marigo P., Weisz D., Dolphin A., Boyer M. L., Olsen K., Skillman E., Seth A. C., 2012, The Astrophysical Journal, 748, 47

Min M., Waters L. B. F. M., de Koter A., Hovenier J. W., Keller L. P., Markwick-Kemper F., 2007, Astronomy and Astrophysics, 462, 667

Muratov A. L., Kereš D., Faucher-Giguère C.-A., Hopkins P. F., Ma X., Anglés-Alcázar D., Chan T. K., Torrey P., Hafen Z. H., Quataert E., Murray N., 2017, Monthly Notices of the Royal Astronomical Society, 468, 4170

Muratov A. L., Kereš D., Faucher-Giguère C.-A., Hopkins P. F., Quataert E., Murray N., 2015, Monthly Notices of the Royal Astronomical Society, 454, 2691

Murray N., Quataert E., Thompson T. A., 2005, The Astrophysical Journal, 618, 569

Murray N., Quataert E., Thompson T. A., 2010, The Astrophysical Journal, 709, 191

Narayanan D., Conroy C., Davé R., Johnson B. D., Popping G., 2018, The Astrophysical Journal, 869, 70

Narayanan D., Smith J. D., Hensley B., Li Q., Hu C.-Y., Sandstrom K., Torrey P., Vogelsberger M., Marinacci F., Sales L., 2023, A Framework for Modeling Polycyclic Aromatic Hydrocarbon Emission in Galaxy Evolution Simulations

Narayanan D., Turk M., Feldmann R., Robitaille T., Hopkins P., Thompson R., Hayward C., Ball D., Faucher-Giguère C.-A., Kereš D., 2015, Nature, 525, 496

Navarro J. F., Frenk C. S., White S. D. M., 1996, The Astrophysical Journal, 462, 563

Nomoto K., Kobayashi C., Tominaga N., 2013, Annual Review of Astronomy and Astrophysics, 51, 457

Nomoto K., Tominaga N., Umeda H., Kobayashi C., Maeda K., 2006, Nuclear Physics A, 777, 424

Nozawa T., Maeda K., Kozasa T., Tanaka M., Nomoto K., Umeda H., 2011, The Astrophysical Journal, 736, 1, 45

Oort J. H., Rougoor G. W., 1960, Monthly Notices of the Royal Astronomical Society, 121, 171

Ormel C. W., Min M., Tielens A. G. G. M., Dominik C., Paszun D., 2011, Astronomy & Astrophysics, Volume 532, id.A43, <NUMPAGES>10</NUMPAGES> pp., 532, A43

Orr M. E., Hayward C. C., Hopkins P. F., Chan T. K., Faucher-Giguère C.-A., Feldmann R., Kereš D., Murray N., Quataert E., 2018, Monthly Notices of the Royal Astronomical Society, 478, 3653

Pandya V., Fielding D. B., Anglés-Alcázar D., Somerville R. S., Bryan G. L., Hayward C. C., Stern J., Kim C.-G., Quataert E., Forbes J. C., Faucher-Giguère C.-A., Feldmann R., Hafen Z., Hopkins P. F., Kereš D., Murray N., Wetzel A., 2021, Monthly Notices of the Royal Astronomical Society, 508, 2979

Panuzzo P., Granato G. L., Buat V., Inoue A. K., Silva L., Iglesias-Páramo J., Bressan A., 2007, Monthly Notices of the Royal Astronomical Society, 375, 640

Parente M., Ragone-Figueroa C., Granato G. L., Borgani S., Murante G., Valentini M., Bressan A., Lapi A., 2022, Monthly Notices of the Royal Astronomical Society, 515, 2053

Parker D. S. N., Zhang F., Kim Y. S., Kaiser R. I., Landera A., Kislov V. V., Mebel A. M., Tielens A. G. G. M., 2012, Proceedings of the National Academy of Sciences, 109, 1, 53

Parvathi V. S., Sofia U. J., Murthy J., Babu B. R. S., 2012, The Astrophysical Journal, 760, 36

Pei Y. C., 1992, The Astrophysical Journal, 395, 130

Péroux C., Howk J. C., 2020, Annual Review of Astronomy and Astrophysics, 58, 363

Pignatari M., Herwig F., Hirschi R., Bennett M., Rockefeller G., Fryer C., Timmes F. X., Ritter C., Heger A., Jones S., Battino U., Dotter A., Trappitsch R., Diehl S., Frischknecht U., Hungerford A., Magkotsios G., Travaglio C., Young P., 2016, The Astrophysical Journal Supplement Series, 225, 24

Pilyugin L. S., Grebel E. K., 2016, Monthly Notices of the Royal Astronomical Society, 457, 3678

Popping G., Péroux C., 2022, arXiv:2203.03686 [astro-ph]

Popping G., Somerville R. S., Galametz M., 2017, Monthly Notices of the Royal Astronomical Society, 471, 3152

Poteet C. A., Whittet D. C. B., Draine B. T., 2015, The Astrophysical Journal, 801, 110

Prantzos N., Abia C., Limongi M., Chieffi A., Cristallo S., 2018, Monthly Notices of the Royal Astronomical Society, 476, 3432

Priestley F. D., De Looze I., Barlow M. J., 2022, Monthly Notices of the Royal Astronomical Society, 509, L6

Prochaska J. X., Wolfe A. M., 1997, The Astrophysical Journal, 487, 1, 73

Rau S.-J., Hirashita H., Murga M., 2019, Monthly Notices of the Royal Astronomical Society, 489, 5218

Rémy-Ruyer A., Madden S. C., Galliano F., Galametz M., Takeuchi T. T., Asano R. S., Zhukovska S., Lebouteiller V., Cormier D., Jones A., Bocchio M., Baes M., Bendo G. J., Boquien M., Boselli A., DeLooze I., Doublier-Pritchard V., Hughes T., Karczewski O. Ł., Spinoglio L., 2014, Astronomy and Astrophysics, 563, A31

Rémy-Ruyer A., Madden S. C., Galliano F., Lebouteiller V., Baes M., Bendo G. J., Boselli A., Ciesla L., Cormier D., Cooray A., Cortese L., De Looze I., Doublier-Pritchard V., Galametz M., Jones A. P., Karczewski O. Ł., Lu N., Spinoglio L., 2015, Astronomy and Astrophysics, 582, A121

Rho J., Kozasa T., Reach W. T., Smith J. D., Rudnick L., DeLaney T., Ennis J. A., Gomez H., Tappe A., 2008, The Astrophysical Journal, 673, 1, 271

Rhodin N. H. P., Agertz O., Christensen L., Renaud F., Fynbo J. P. U., 2019, Monthly Notices of the Royal Astronomical Society, 488, 3, 3634

Rogantini D., Costantini E., Zeegers S. T., de Vries C. P., Bras W., de Groot F., Mutschke H., Waters L. B. F. M., 2018, Astronomy and Astrophysics, 609, A22

Rogantini D., Costantini E., Zeegers S. T., Mehdipour M., Psaradaki I., Raassen A. J. J., de Vries C. P., Waters L. B. F. M., 2020, Astronomy and Astrophysics, 641, A149

Roman-Duval J., Aloisi A., Gordon K., Hagen L., Henry A., James B., Jenkins E. B., Lebouteiller V., Rafelski M., Tchernyshyov K., Welty D., 2019a, Bulletin of the American Astronomical Society, 51, 458

Roman-Duval J., Bot C., Chastenet J., Gordon K., 2017, The Astrophysical Journal, 841, 72

Roman-Duval J., Gordon K. D., Meixner M., Bot C., Bolatto A., Hughes A., Wong T., Babler B., Bernard J.-P., Clayton G. C., Fukui Y., Galametz M., Galliano F., Glover S., Hony S., Israel F., Jameson K., Lebouteiller V., Lee M.-Y., Li A., Madden S., Misselt K., Montiel E., Okumura K., Onishi T., Panuzzo P., Reach W., Remy-Ruyer A., Robitaille T., Rubio M., Sauvage M., Seale J., Sewilo M., Staveley-Smith L., Zhukovska S., 2014, The Astrophysical Journal, 797, 86

Roman-Duval J., Jenkins E. B., Tchernyshyov K., Williams B., Clark C. J. R., Gordon K. D., Meixner M., Hagen L., Peek J., Sandstrom K., Werk J., Yanchulova Merica-Jones P., 2021, The Astrophysical Journal, 910, 95

Roman-Duval J., Jenkins E. B., Tchernyshyov K., Clark C. J. R., De Cia A., Gordon K. D., Hamanowicz A., Lebouteiller V., Rafelski M., Sandstrom K., Werk J., Merica-Jones P. Y., 2022a, The Astrophysical Journal, 928, 90

Roman-Duval J., Jenkins E. B., Tchernyshyov K., Clark C. J. R., Cia A. D., Gordon K. D., Hamanowicz A., Lebouteiller V., Rafelski M., Sandstrom K., Werk J., Merica-Jones P. Y., 2022b, The Astrophysical Journal, 935, 105

Roman-Duval J., Jenkins E. B., Williams B., Tchernyshyov K., Gordon K., Meixner M., Hagen L., Peek J., Sandstrom K., Werk J., Yanchulova Merica-Jones P., 2019b, The Astrophysical Journal, 871, 151

Salim S., Narayanan D., 2020, Annual Review of Astronomy and Astrophysics, 58, 529

Savage B. D., Sembach K. R., 1996, Annual Review of Astronomy and Astrophysics, 34, 279

Schneider R., Valiante R., Ventura P., dell'Agli F., Di Criscienzo M., Hirashita H., Kemper F., 2014, Monthly Notices of the Royal Astronomical Society, 442, 1440

Seon K.-I., Draine B. T., 2016, The Astrophysical Journal, 833, 201

Shapley H., 1918, Publications of the Astronomical Society of the Pacific, 30, 42

Sheffer Y., Rogers M., Federman S. R., Abel N. P., Gredel R., Lambert D. L., Shaw G., 2008, The Astrophysical Journal, 687, 1075

Shivaei I., Boogaard L., Díaz-Santos T., Battisti A., da Cunha E., Brinchmann J., Maseda M., Matthee J., Monreal-Ibero A., Nanayakkara T., Popping G., Vidal-García A., Weilbacher P. M., 2022, Monthly Notices of the Royal Astronomical Society, 514, 1886

Smith N., 2014, Annual Review of Astronomy and Astrophysics, 52, 1, 487

Snow T. P., McCall B. J., 2006, Annual Review of Astronomy and Astrophysics, 44, 367

Sofia U. J., Parvathi V. S., Babu B. R. S., Murthy J., 2011, The Astronomical Journal, 141, 22

Stecher T. P., Donn B., 1965, The Astrophysical Journal, 142, 1681

Strandet M. L., Weiss A., De Breuck C., Marrone D. P., Vieira J. D., Aravena M., Ashby M. L. N., Béthermin M., Bothwell M. S., Bradford C. M., Carlstrom J. E., Chapman S. C., Cunningham D. J. M., Chen C.-C., Fassnacht C. D., Gonzalez A. H., Greve T. R., Gullberg B., Hayward C. C., Hezaveh Y., Litke K., Ma J., Malkan M., Menten K. M., Miller T., Murphy E. J., Narayanan D., Phadke K. A., Rotermund K. M., Spilker J. S., Sreevani J., 2017, The Astrophysical Journal, 842, L15

Su K.-Y., Hopkins P. F., Hayward C. C., Faucher-Giguère C.-A., Kereš D., Ma X., Robles V. H., 2017, Monthly Notices of the Royal Astronomical Society, 471, 1, 144

Sugerman B. E. K., Ercolano B., Barlow M. J., Tielens A. G. G. M., Clayton G. C., Zijlstra A. A., Meixner M., Speck A., Gledhill T. M., Panagia N., Cohen M., Gordon K. D., Meyer M., Fabbri J., Bowey J. E., Welch D. L., Regan M. W., Kennicutt R. C., 2006, Science, 313, 5784, 196

Sukhbold T., Ertl T., Woosley S. E., Brown J. M., Janka H. T., 2016, The Astrophysical Journal, 821, 38

Thompson T. A., Fabian A. C., Quataert E., Murray N., 2015, Monthly Notices of the Royal Astronomical Society, 449, 147

Thompson T. A., Quataert E., Murray N., 2005, The Astrophysical Journal, 630, 167

Tielens A. G. G. M., Hollenbach D., 1985, The Astrophysical Journal, 291, 722

Todini P., Ferrara A., 2001, Monthly Notices of the Royal Astronomical Society, 325, 2, 726

Trayford J. W., Camps P., Theuns T., Baes M., Bower R. G., Crain R. A., Gunawardhana M. L. P., Schaller M., Schaye J., Frenk C. S., 2017, Monthly Notices of the Royal Astronomical Society, 470, 771

Trayford J. W., Lagos C. d. P., Robotham A. S. G., Obreschkow D., 2020, Monthly Notices of the Royal Astronomical Society, 491, 3937

Triani D. P., Sinha M., Croton D. J., Pacifici C., Dwek E., 2020, Monthly Notices of the Royal Astronomical Society, 493, 2490

Trumpler R. J., 1930, Publications of the Astronomical Society of the Pacific, 42, 214

Tsai J. C., Mathews W. G., 1995, The Astrophysical Journal, 448, 84

Turk M. J., Smith B. D., Oishi J. S., Skory S., Skillman S. W., Abel T., Norman M. L., 2011, The Astrophysical Journal Supplement Series, 192, 9

van Dishoeck E. F., Blake G. A., 1998, Annual Review of Astronomy and Astrophysics, 36, 317

van Dishoeck E. F., Blake G. A., Draine B. T., Lunine J. I., 1993, in Protostars and Planets III, 163, University of Arizona Press, Arizona

Vílchez J. M., Relaño M., Kennicutt R., De Looze I., Mollá M., Galametz M., 2019, Monthly Notices of the Royal Astronomical Society, 483, 4968

Virtanen P., Gommers R., Oliphant T. E., Haberland M., Reddy T., Cournapeau D., Burovski E., Peterson P., Weckesser W., Bright J., van der Walt S. J., Brett M., Wilson J., Millman K. J., Mayorov N., Nelson A. R. J., Jones E., Kern R., Larson E., Carey C. J., Polat İ., Feng Y., Moore E. W., VanderPlas J., Laxalde D., Perktold J., Cimrman R., Henriksen I., Quintero E. A., Harris C. R., Archibald A. M., Ribeiro A. H., Pedregosa F., van Mulbregt P., SciPy 1.0 Contributors, 2020, Nature Methods, 17, 261

Wang S., Li A., Jiang B. W., 2015, Monthly Notices of the Royal Astronomical Society, 454, 569

Weingartner J. C., Draine B. T., 1999, The Astrophysical Journal, 517, 292

Weingartner J. C., Draine B. T., 2001a, The Astrophysical Journal, 548, 296

Weingartner J. C., Draine B. T., 2001b, The Astrophysical Journal Supplement Series, 134, 263

Westphal A. J., Stroud R. M., Bechtel H. A., Brenker F. E., Butterworth A. L., Flynn G. J., Frank D. R., Gainsforth Z., Hillier J. K., Postberg F., Simionovici A. S., Sterken V. J., Nittler L. R., Allen C., Anderson D., Ansari A., Bajt S., Bastien R. K., Bassim N., Bridges J., Brownlee D. E., Burchell M., Burghammer M., Changela H., Cloetens P., Davis A. M., Doll R., Floss C., Grün E., Heck P. R., Hoppe P., Hudson B., Huth J., Kearsley A., King A. J., Lai B., Leitner J., Lemelle L., Leonard A., Leroux H., Lettieri R., Marchant W., Ogliore R., Ong W. J., Price M. C., Sandford S. A., Tresseras J.-A. S., Schmitz S., Schoonjans T., Schreiber K., Silversmit G., Solé V. A., Srama R., Stadermann F., Stephan T., Stodolna J., Sutton S., Trieloff M., Tsou P., Tyliszczak T., Vekemans B., Vincze L., Von Korff J., Wordsworth N., Zevin D., Zolensky M. E., aff14, 2014, Science, 345, 786

Wheeler C., Hopkins P. F., Pace A. B., Garrison-Kimmel S., Boylan-Kolchin M., Wetzel A., Bullock J. S., Kereš D., Faucher-Giguère C.-A., Quataert E., 2019, Monthly Notices of the Royal Astronomical Society, 490, 4447

Whittet D. C. B., 2003, Dust in the Galactic Environment, Institute of Physics Publishing, Bristol, 2nd edn.

Whittet D. C. B., 2010, The Astrophysical Journal, 710, 1009

Wolfe A. M., Gawiser E., Prochaska J. X., 2005, Annual Review of Astronomy & Astrophysics, vol. 43, Issue 1, pp.861-918, 43, 1, 861

Zeegers S. T., Costantini E., Rogantini D., de Vries C. P., Mutschke H., Mohr P., de Groot F., Tielens A. G. G. M., 2019, Astronomy and Astrophysics, 627, A16

Zhukovska S., 2014, Astronomy and Astrophysics, 562, A76

Zhukovska S., Dobbs C., Jenkins E. B., Klessen R. S., 2016, The Astrophysical Journal, 831, 147

Zhukovska S., Gail H.-P., Trieloff M., 2008, Astronomy and Astrophysics, 479, 453

Zhukovska S., Henning T., 2013, Astronomy and Astrophysics, 555, A99

Zhukovska S., Henning T., Dobbs C., 2018, The Astrophysical Journal, 857, 94

Zibetti S., Gallazzi A., Charlot S., Pierini D., Pasquali A., 2013, Monthly Notices of the Royal Astronomical Society, 428, 1479